Forcing Stem Cells to Behave: Dissecting the Mechanobiology of Human Pluripotent Stem Cells Using Microengineering Approaches

by

Yubing Sun

A dissertation submitted in partial fulfillment
of the requirements for the degree of
Doctor of Philosophy
(Mechanical Engineering)
in the University of Michigan
2015

Doctoral Committee:

Associate Professor Jianping Fu, Chair
Professor Paul Krebsbach
Assistant Professor Allen Liu
Professor Sue O'Shea
Associate Professor Andrew Putnam

2015

To my family,

Acknowledgement

This thesis can never be done without the help from many others. First, I feel very lucky to have a great Ph.D. advisor, Dr. Jianping Fu, who is always positive and supportive, who is always patient when I faced challenges, who spent numerous time helping me establish my own academic career. It is a privilege to be one of the first few students of Dr. Fu, because I had the freedom to explore an exciting new field and establish a new research program from scratch. As the lab become matured, I become matured as well. At the end of the day, the Ph.D. training is not just about knowledge, papers, or skills, but more importantly, about the way you look at things. From this perspective, every single day I spent in G.G Brown building is well worth it.

Of course, I owe special thanks to all the other members in my thesis committee. Dr. Paul Krebsbach and Dr. Sue O'Shea help me jump start my human pluripotent stem cell research by providing many resources and advices. I also learned a lot from Dr. Luis Villa-Diaz and Dr. Jin Koo Kim from Krebsbach Lab. They are all wonderful collaborators that every researcher wouldn't dream of. I would like to thank Dr. Andy Putnam and his student, Dr. Yen Kong, for always providing instructive suggestions to my research and working together on very exciting projects. I would like to thank Dr. Allen Liu for always making effort to share his broad knowledge and experience with me and sharing his expensive equipment unreservedly.

There are many others I wish to express my thanks to, including my wonderful collaborators: Drs. Cheri Deng, Di Chen, Zhenzhen Fan, Raymond Lam, Devin Rosenthal and Steve Allen; my fellow Fu lab members; talented undergrads I have worked with: Renee Philson, Heng Yang, Chunan Huang, *etc*.; and last but not least, my wife Yuan Zhou and my daughter Amber, for their endless love and support.

A Ph.D. degree is not the end but a new start. "Two roads diverged in a wood, and I--, I took the one less traveled by. And that has made all the difference."

Table of Contents

List of Figures

List of Appendices

Abstract

Stem cells, especially human pluripotent stem cells (hPSCs), hold significant promise for modeling developmental and disease processes, drug and toxicology screening, and cell-based regenerative medicine. Most hPSC studies have so far focused on identifying extrinsic soluble factors, intracellular signaling pathways, and transcriptional regulatory networks involved in regulating hPSC behaviors. This thesis focuses on the development and application of some novel synthetic micromechanical systems to understand the mechano-sensitive and -responsive properties of hPSCs and their functional regulation of self-renewal, directed differentiation, and survival of hPSCs. First, we have demonstrated that rigid PDMS micropost arrays (PMAs, Young's modulus $E_{eff=}$ 1MPa) support the maintenance of pluripotency of hPSCs. Blocking cytoskeleton contractility by blebbistatin and inhibiting E-cadherin functions by DECMA-1 antibody both impair mechanoresponsive self-renewal of hPSCs on rigid substrates. We have further achieved efficient neuroepithelial induction, caudalization, and motor neuron differentiation from hPSCs combing soft PMAs ($E_{eff<}$ 5kPa) with dual Smad inhibition. The purity and yield of functional motor neurons derived from hPSCs within 23 days of culture using soft PMAs were improved four- and twelve-fold, respectively, compared to coverslips or rigid PMAs. Our mechanistic work has helped reveal for the first time that biomechanical cues, including intracellular contractile forces and cell shape, converge and reinforce signal integration of TGF-β, Wnt, Hippo/YAP, Rho GTPase, and the actomyosin cytoskeleton to regulate the neural plate specification. The last part of this thesis focuses on a novel acoustic tweezing cytometry (ATC) utilizing ultrasound pulses to actuate functionalized lipid-encapsulated

microbubbles (MBs) targeted to cell surface integrin receptors to exert subcellular mechanical forces in the pN - nN range. ATC can robustly induce cell traction force changes through acoustic radiation forces and bubble cavitation induced shear stresses. Importantly, ATC stimulations increased the survival rate and cloning efficiency of hESCs by 3-fold, suggesting its potential application in large-scale expansion of hPSCs that is critical for future hPSC-based regenerative therapies and disease modeling.

Chapter 1

Introduction

The major content of this chapter is reproduced from our previously published papers: "Forcing stem cells to behave: a biophysical perspective of the cellular microenvironment" in *Annual Review of Biophysics*, 2012 [1] and "Mechanobiology: a new frontier for human pluripotent stem cells" in *Integrative Biology*, 2013 [2].

1.1. Background and motivation of research

Stem cells are critical players during development, tissue regeneration, and healthy homeostatic cell turnover, and they are an important driving force for the developing fields of functional tissue engineering and regenerative medicine owing to their self-renewal capacity and pluripotency [1, 3]. Due to their ability to generate tissue *de novo* following disease or injury, there is a widespread hope of developing stem cell--based therapies for various degenerative diseases [4, 5]. A key aspect in the enabling of these stem cell-based therapies will be the ability to manipulate stem cell interactions between stem cells and their local microenvironment (a setting *in vivo* known as the stem cell niche) in order to regulate and direct stem cell fate [6, 7]. How the *in vivo* stem cell niche, which filters and presents a wide range of molecular and cellular scale physical and biological signals, acts to regulate tissue regeneration based on physiological

demand and pathological state remains incompletely understood [8-12]. *In vivo*, stem cell niches create specialized microenvironments, consisting of soluble and surface-bound signaling factors, cell-cell contacts, stem cell niche support cells, extracellular matrix (ECM), and local mechanical microenvironment. Although stem cell biologists have long appreciated the regulatory roles for soluble stem -cell niche signals (e.g., growth factors and cytokines) in regulating stem cell fate, recent evidence demonstrates that regulation of stem cell fate by these soluble factors is strongly influenced by the coexisting insoluble adhesive, mechanical, and topological cues inherently contained and dynamically regulated in the stem cell niche [13-17]. These insoluble biophysical cues can be sensed and transduced into intracellular biochemical and functional responses by stem cells, a process known as mechanotransduction [18-24].

Recent evidence has demonstrated that biophysical signals in the cellular microenvironment of stem cells can have extensive potential to regulate and synergize with classical signal transduction pathways induced by soluble factors to control stem cell fate (Figure 1-1). Such advances are enabled by emerging bioengineering strategies for controllable synthetic cellular microenvironment developed through the interactions of stem cell biology, tissue engineering, and microtechnology/nanotechnology at multiple length scales. This dissertation will discuss some exciting, interdisciplinary research integrating microengineering, cell and molecular biology, and biomaterials for elucidating the regulatory roles of mechanical cues in stem cells, in particular, human pluripotent stem cells (hPSCs) (Figure 1-2). This dissertation will first discuss the roles of substrate rigidity, a critical mechanical cue in stem cell microenvironment, in determining the pluripotency (chapter 2) and neuronal differentiation (chapter 3) of hPSCs. This dissertation will further explore the pivotal roles of traction forces and cell shape in neural plate development using a novel *in vitro* neural plate model generated by

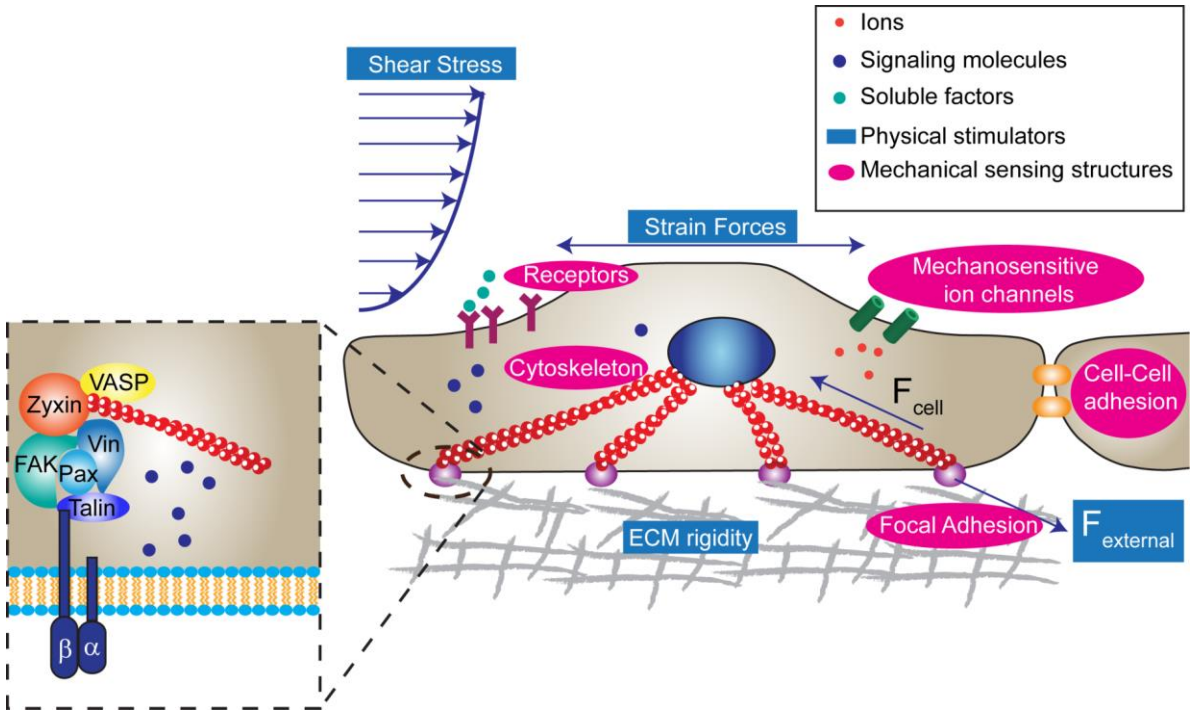

Figure 1-1 Schematic showing biophysical signals in the stem cell niche and the intricate reciprocal molecular interactions between stem cells and their microenvironment to regulate stem cell fate. The extracellular microenvironment of stem cells is a hydrated protein- and proteoglycan-based gel network comprising soluble and physically bound signals as well as signals arising from cell-cell interactions. Biophysical signals in the stem cell niche include matrix rigidity and topography, flow shear stress, strain forces, and other mechanical forces exerted by adjacent support cells. Stem cells can sense these biophysical stimuli through mechanosensitive ion channels, focal adhesions, cell surface receptors, actin cytoskeleton, and cell-cell adhesions. A magnified view of the focal adhesion structure is also shown, which includes transmembrane heterodimeric integrin, paxillin (Pax), talin, focal adhesion kinase (FAK), vinculin (Vin), Zyxin, and vasodilator-stimulated phosphoprotein (VASP).

micropatterning (chapter 4). Moreover, this dissertation will describe acoustic tweezing cytometry (ATC), a novel tool to apply subcellular mechanical forces to cells, and its important applications in rescuing the apoptosis of single disassociated hPSCs (chapter 5). Together, leveraging a range of microengineered tools, my thesis research lays the foundation of the mechanobiology of hPSCs and greatly contributes to the stem cell-based regenerative medicine.

1.2. Research Topics and Dissertation Outline

1.2.1. Substrate mechanics regulate the self-renewal of hPSCs

Human pluripotent stem cells (hPSCs) including human embryonic stem cells (hESCs) and human induced pluripotent stem cells (hiPSCs) hold significant promise for modeling developmental and disease processes, drug and toxicity screening, and cell-based regenerative medicine. Most studies of hPSCs have so far focused on illustrating different biochemical factors, signaling pathways, and transcriptional networks that are involved in regulating hPSC self-

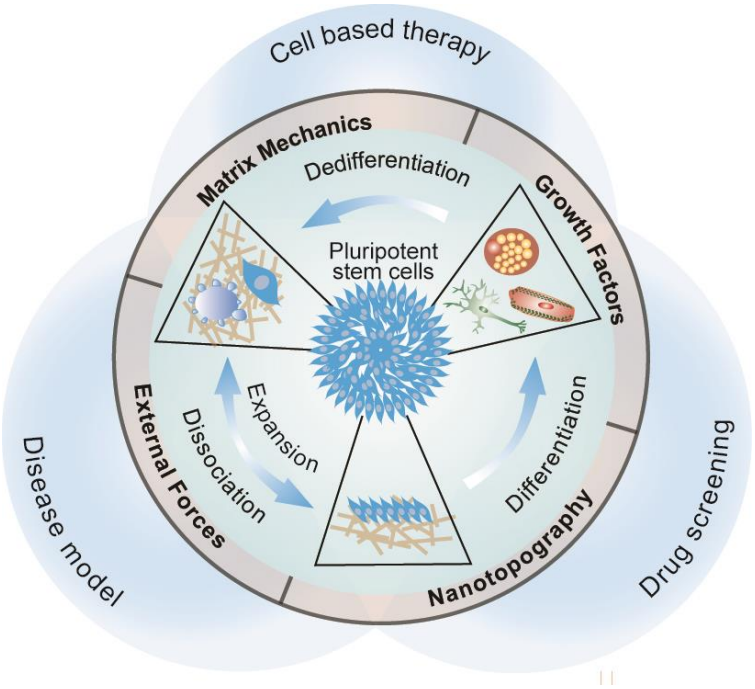

Figure 1-2 High-throughput micromechanical tools for precise control and measurements of mechanical stimuli and response to improve hPSC culture.

renewal and differentiation, revealing that, for example, soluble growth factors, such as those in the TGF-β superfamily and FGF, Wnt, and Hedgehog families, are important in regulating self-renewal and differentiation of hPSCs in cell culture through their effects on a core network of transcription factors including OCT3/4, NANOG, and SOX2, which function in concert to regulate target genes necessary for pluripotency maintenance and lineage specification of hPSCs [25-28]. Currently, large-scale preclinical and clinical applications of hPSCs remain challenging owing to the lack of understanding of hPSCs microenvironments [29]. Indeed,

mechanoresponsive behaviors of human adult stem cells including hematopoietic, mesenchymal, neural and skeletal muscle stem cells have been well documented recently [30-34]. Collectively, there is still limited knowledge of how mechanical signals in the local cellular microenvironment regulate fate decisions of hESCs, and advancing in such knowledge will be critical for both fundamental understanding and clinical applications of hESCs.

Therefore, in chapter 2, I will investigate explicitly the mechanosensitive properties of hESCs [2, 35, 36]. Here, I applied a unique synthetic microengineered substrate system, the poly(dimethylsiloxane) micropost array (PMA), and demonstrated that hESCs are mechanosensitive, and they could increase their cytoskeleton contractility with matrix rigidity. Furthermore, rigid substrates supported maintenance of pluripotency of hESCs. Matrix mechanics-mediated cytoskeleton contractility might be functionally correlated with E-cadherin expressions in cell-cell contacts and thus involved in fate decisions of hESCs. My results highlighted the important functional link between matrix rigidity, cellular mechanics, and pluripotency of hESCs and provided a novel approach to characterize and understand mechanotransduction and its involvement in hESC function.

1.2.2. Hippo/YAP-mediated rigidity-dependent motor neuron differentiation of hPSCs

The effects of the physical microenvironment on the differentiation of hPSCs are not completely established. Poorly defined culture conditions and inefficient protocols for derivation of MNs from hPSCs have hindered their use in regenerating neural tissues.

In chapter 3, I applied PMA systems with varying mechanical rigidities to accelerate neural induction and caudalization of hPSCs [37, 38]. The purity and yield of functional motor neurons (MNs) derived from hPSCs within 23 days of culture using soft PMAs were improved

four- and twelve-fold, respectively, compared to coverslips or rigid PMAs. Mechanistic studies revealed a multi-targeted mechanotransductive process involving Smad phosphorylation and nucleocytoplasmic shuttling, regulated by rigidity-dependent Hippo-YAP activities and actomyosin cytoskeleton integrity and contractility. These data suggest that substrate rigidity is an important biophysical cue influencing neural induction and subtype specification. Synthetic, microengineered substrates therefore can serve as an innovative platform for future large-scale culture of hPSCs.

1.2.3. Modeling neural plate development *in vitro*

Embryo development coincides with drastic changes of cell morphology and tissue organization, which suggest the important involvement of mechanical forces. However, the detailed role and mechanism of forces during development is largely unknown due to the lack of proper tools. As important models for studying human embryo development, hESCs provide tremendous opportunities for the investigation of biomechanics during development.

In chapter 4, I combined microengineering tools (micropatterning, PMAs, microfluidic chambers, etc) and hESCs to study whether mechanical forces and cell shape can regulate the fate decision and regionalization of neural border cells. I discovered that micropatterning can facilitate the spontaneous formation of neural plate-like structures, with Pax6+ neuroepithelial cells located in the center of the patterns and Pax3+ neural crest cells located in the periphery of the patterns. Using this model, I found that both contractility and cell shape are important for the formation of such structure. Further gene expression analysis revealed that cell shape can regulate BMP activities, which are critical for the neural crest specification. These results quantitatively reveal that how mechanical forces and corresponding cell shape changes, synergizing with biochemical cues, determine the lineage bifurcation in neural plate.

1.2.4. Acoustic tweezing cytometry for stem cell applications

Mechanical forces are critical to modulate cell spreading, contractility, gene expression, and even stem cell differentiation. Yet, existing tools that can apply controllable subcellular forces to a large number of single cells simultaneously are still limited. In chapter 5, I will discuss a novel ultrasound tweezing cytometry utilizing ultrasound pulses to actuate functionalized lipid microbubbles covalently attached to single live cells to exert mechanical forces in the pN - nN range [39-41]. Ultrasonic excitation of microbubbles could elicit a rapid and sustained reactive intracellular cytoskeleton contractile force increase in different adherent mechanosensitive cells. Further, ultrasound-mediated intracellular cytoskeleton contractility enhancement was dose-dependent and required an intact actin cytoskeleton as well as RhoA/ROCK signaling. My results demonstrated the great potential of ultrasound tweezing cytometry technique using functionalized microbubbles as an actuatable, biocompatible, and multifunctional agent for biomechanical stimulations of cells.

Dissociation-induced apoptosis of human embryonic stem cells (hESCs) hampers their large-scale culture. Herein we leveraged the mechanosensitivity of hESCs and used a novel technique, ATC, for subcellular mechanical stimulation of disassociated single hESCs to improve their survival. By acoustically actuating integrin-bound microbubbles to live cells, ATC increased the survival rate and cloning efficiency of hESCs by 3-fold. A positive correlation was observed between increased hESC survival rate and total accumulative displacement of integrin-anchored MBs during ATC stimulation. Our study suggests ATC as a promising biocompatible tool to improve hESC culture.

Chapter 2

Substrate mechanics regulates the self-renewal of hESCs

The major content of this chapter is reproduced from our previously published paper: "Mechanics regulates fate decisions of human embryonic stem cells" in *PLoS ONE*, 2012[36].

2.1. Introduction

Experimental evidence established in recent years has shown that mechanical signals experienced by ESCs through their biophysical interactions with the extracellular matrix (ECM) can play critical roles in regulating survival, proliferation and differentiation. For example, Saha *et al.* reported that cyclic mechanical stretches inhibit differentiation of human ESCs (hESCs) through the TGF-β/Activin/Nodal signaling pathway [42, 43]. Chowdhury *et al.* recently demonstrated that a local cyclic stress applied through focal adhesions (FAs) to mouse ESCs (mESCs) induce their spreading and differentiation [44]. In addition to external mechanical forces, matrix mechanics has also been shown to regulate lineage commitments of human mesenchymal stem cells [31, 45]. More recently, two independent studies have indicated that mESCs can sense and respond to subtle changes in matrix mechanics. First, Evans *et al.* [46] demonstrated that mESCs showed increased spreading, proliferation and osteogenic differentiation when plated on rigid poly-dimethylsiloxane (PDMS) substrates as compared to

the cells plated on soft ones. The second study by Chowdhury *et al.* demonstrated that mESCs could maintain their pluripotency for a long term on soft polyacrylamide gels even without leukemia inhibitory factor (LIF), which is essential for maintaining pluripotency of mESCs [47]. hESCs are intrinsically different from mESCs, in regard to the required growth factors and dominant signal pathways that regulate their pluripotency [26].

The mechano-sensitive and -responsive properties of hPSCs have not been examined explicitly until recently. Different groups including our own have lately started to investigate whether the survival, self-renewal and differentiation of hESCs can be regulated by substrate rigidity at the single-cell level [48-50]. Unlike mouse ESCs (mESCs), single hPSCs tend to differentiate spontaneously in the cell culture. Further, the survival rate and cloning efficiency of single hPSCs is extremely low as they tend to undergo apoptosis upon complete dissociation into single cells. hPSCs are intrinsically different from mESCs, in regard to the required growth factors and dominant signal pathways that regulate their pluripotency. Thus, there is still a critical knowledge gap in understanding the mechano-sensitive and -responsive properties of hPSCs.

Keung *et al*. have recently studied responses of small clusters of hESCs and hiPSCs to bulk rigidity changes in Matrigel coated polyacrylamide (PA) gels [49]. Their results have shown that substrate rigidity does not affect proliferation or expression of pluripotent markers including NANOG, OCT4 and SSEA-4 for hPSCs after culturing the cell clusters for 3 days under a self-renewal medium condition. A more recent study by Musah *et al.* have refined the PA gel system by functionalizing the hydrogel with an adhesive peptide (GKKQRFRHRNRKG) derived from vitronectin [49], which has been shown in their previous work to bind to cell surface GAGs and support the long-term self-renewal of hESCs [51]. Interestingly, Musah *et al*. have found that

only rigid PA gels functionalized with the adhesive peptide can maintain hESC proliferation and pluripotency, consistent with our finding that rigid micropost arrays coated with vitronectin support maintenance of pluripotency of hESCs [50]. Altogether, our work and the studies by Keung *et al*. and Musah *et al*. all point to the conclusion that unlike mESCs [47], soft microenvironment does not promote the survival and self-renewal of hPSCs. The differences between the observations by our group and Musah *et al*. and the results reported by Keung *et al*. suggest the possibility that rigidity sensing of hPSCs may critically depend on the specific cell adhesion molecules employed by hPSCs to bind to the surrounding ECM. The differences between these studies also underscore the importance in recognizing the differences in molecular-scale material properties (such as porosity, surface chemistry, molecular backbone flexibility and binding properties of immobilized adhesive ligands) when comparing different hydrogel systems. Recent studies using synthetic hydrogels for hPSCs and human adult stem cells have strongly indicated that these molecular-scale changes in material properties can have profound effects on stem cell function [52, 53] .

2.2. Materials and Methods

2.2.1. Fabrication and surface functionalization of the PDMS micropost array

The PDMS micropost arrays were fabricated using the protocol described previously [54]. Briefly, silicon micropost array masters were fabricated by standard photolithography and deep reactive ion etching (DRIE). The height of the silicon micropost was modulated by controlling the DRIE etch time. The silicon masters were silanized with (tridecafluoro-1,1,2,2,-tetrahydrooctyl)-1-trichlorosilane (United Chemical Technologies, Bristol, PA) for 4 hr under vacuum. Then, 1:10 (w/w, curing agent:base monomer) ratio PDMS prepolymer (Sylgard 184, Dow-Corning, Midland, MI) was poured over the silicon micropost master and cured at 110°C

for 20 min. The negative PDMS mold was then generated by peeling off from the silicon master, oxidized with the oxygen plasma for 1 min (200 mTorr; Plasma Prep II, West Chester, PA), and silanization with (tridecafluoro-1,1,2,2,-tetrahydrooctyl)-1-trichlorosilane for 24 hrs to obtain the PDMS negative mold. To generate the final PDMS micropost array, 1:10 ratio PDMS prepolymer was poured over the negative PDMS mold and degassed under vacuum for 10 min. Then a clean 25 cm × 25 cm cover glass was placed on top of the negative mold and the whole assembly was cured at 110°C for 40 hrs. The negative mold was then peeled off to release the final PDMS micropost array. The collapsed PDMS microposts during peeling off was rescued by sonication in 100% ethanol for 30 sec followed by dry-release with liquid CO_2 using a critical point dryer (Samdri®-PVT-3D, Tousimis, Rockville, MD).

The top surface of the PDMS micropost array was functionalized with human recombinant vitronectin (R&D system, Minneapolis, MN) to promote adhesion of hESCs. Briefly, a flat 1:30 PDMS stamp was soaked with vitronectin at a concentration of 20 $\mu g\ mL^{-1}$ in distilled water for 1 hr at room temperature. The PDMS stamp was then thoroughly rinsed with distilled water and blown dry with a stream of nitrogen. In parallel, the PDMS micropost array was treated with ozone generated by a UV-ozone cleaner (Jelight, Irvine, CA) for 7 min to activate the surface of the PDMS micropost array, so that the hydroxyl group generated during this process on the PDMS surface could covalently bond to vitronectin. The PDMS stamp was then placed in conformal contact with the PDMS micropost array for about 10 sec. To prevent non-specific protein absorption to the non-functionalized surface of the PDMS micropost array, the PDMS micropost array was soaked in pluronics F127 NF dissolved in PBS (0.2%, w/v; BASF, Ludwigshafen, Germany) for 30 min. For the PDMS micropost array used for traction force measurement, an additional labeling step was performed by soaking the PDMS micropost

array with 1,1'-dioctadecyl-3,3,3',3'-tetramethylindodicarbocyanine perchlorate ('DiD' oil; Invitrogen, Carlsbad, CA) before the treatment with the pluronics F 127 NF.

2.2.2. Cell culture and seeding cells on the PDMS micropost array

hESCs (H9 and H1, obtained from WiCell, Madison, WI) were cultured on a feeder-free synthetic polymer coating (PMEDSAH) [55, 56] with the Human-Cell-Conditioned Medium (GlobalStem, Rockville, MD) supplemented with 8 ng/mL of human recombinant basic fibroblast growth factor (bFGF; Globalstem). Before plating cells, differentiated cells were removed manually by a modified pasteur pipette under a stereomicroscope (Leica MZ9.5, Leica Microsystems Inc., Buffalo Grove, IL). Then, undifferentiated colonies were collected as small cell aggregates using the STEMPRO EZPassage Disposable Stem Cell Passaging Tool (Invitrogen) in a 1.5 mL centrifuge tube. After centrifugation and a brief washing with PBS, the cell aggregates were treated with 0.5 mL 0.25% Trypsin-EDTA for 1 min. 1 mL 10% fetal bovine serum (FBS, Invitrogen) was used to stop trypsinization and was followed by an immediate centrifugation. The cell pellet was then dispersed in the StemPro serum free medium (Invitrogen) supplied with 8 ng/mL bFGF and Y27632 (a ROCK inhibitor) at 10 μM and passed through a cell strainer with the 40 μm nylon mesh (BD Biosciences, Bedford, MA) to remove large cell aggregates. The obtained single hESCs were counted and then seeded on the PDMS micropost array at a desired density.

The H1 hESC line (H1, obtained from WiCell) was also tested in this work. These hESCs were cultured on mitotically inactive mouse embryonic fibroblasts (MEFs, obtained from GlobalStem, Rockville, MD) with the standard hESC culture medium containing the knock-out serum replacement (Invitrogen), non-essential amino acid (Invitrogen), and bFGF (Invitrogen).

Before plating the cells, differentiated cells were removed manually by a modified pasteur pipette under a stereomicroscope (Leica), and undifferentiated colonies were collected as small cell aggregates using the STEMPRO EZPassage Disposable Stem Cell Passaging Tool (Invitrogen). The collected cells were briefly rinsed with PBS and treated with TrypLE Select (Invitrogen) for 3 min to release the MEFs. The cells were again rinsed with PBS and then all the cells including hESCs and remaining MEFs were scraped using a cell scraper (BD Biosciences). To further remove the remaining MEFs, the solution containing the cells was transferred into a 35 mm culture dish (BD Biosciences) coated with gelatin and incubated for 45 min. Most MEFs would attach to the dish while hESCs were still in the supernatant. The supernatant was collected and centrifuged and the cell pellet was treated with 0.25% Trypsin-EDTA for 1 min. After this, the same procedure used for H9 cells was followed to obtain and seed single hESCs on the PDMS micropost array.

2.2.3. Quantification of traction forces using the PDMS micropost array

For traction force measurements, the cover glass holding the PDMS micropost array was attached to a 35 mm dish with a 20 mm hole at the center (Glass-bottom-dishes, MatTek, Ashland, MA). Live-cell images were obtained using a 40× objective (1.3 NA, oil immersion; EC Plan NEOFLUAR; Carl Zeiss MicroImaging, Thornwood, NY) on a Zeiss Observer.Z1 microscope equipped with a thermoelectrically-cooled monochrome CCD camera (AxioCam HRM, Carl Zeiss MicroImaging). The microscope was further equipped with an environmental chamber to maintain the experimental environment at 37°C. A microscope stage incubator (Carl Zeiss MicroImaging) was also used to maintain 5% CO_2. The positions of single hESCs were recorded by the AxioVision software (Carl Zeiss MicroImaging). A custom-developed

MATLAB program (details of the program was described in Ref. [54]; The MathWorks, Natick, MA) was used to calculate deflection of the PDMS micropost centroid from its unbent, unloaded position, which was then converted to the horizontal traction force by multiplying with the nominal spring constant *K* of the PDMS micropost.

2.2.4. Immunofluorescence staining

Cells were fixed with 4% paraformaldehyde (Electron Microscopy Sciences, Hatfield, PA) for 20 min at room temperature, and then permeabilized with 0.1% Triton X-100 (Roche Applied Science, Indianapolis, IN) for 20 min. To assay Oct4 expression, Oct4 rabbit polyclonal IgG (Santa Cruz Biotechnology, Santa Cruz, CA) primary antibody, which did not cross-react with Oct4 isoform B, was used and detected by the goat-anti-rabbit Alexa-546 secondary antibody (Invitrogen). To examine the expression of E-cadherin, mouse anti-E-Cadherin primary antibody (Invitrogen) was used and detected by the goat-anti-mouse Alexa-647 secondary antibody (Invitrogen). To examine the effect of myosin inhibition, mouse anti-nonmuscle myosin IIA primary antibody (Abcam, Cambridge, MA) was used and detected by the goat-anti-mouse Alexa-488 secondary antibody (Invitrogen). For vinculin staining, cells were incubated in an ice-cold cytoskeleton buffer (50 mM NaCl, 150 mM sucrose, 3 mM $MgCl_2$, 1 μg/mL aprotinin, 1 μg/mL leupeptin, 1 μg/mL pepstatin, and 2 mM PMSF) for 1 min, followed by 1 min in the cytoskeleton buffer supplemented with 0.5% Triton X-100. After that, the mouse anti-vinculin primary antibody (Sigma-Aldrich, St. Louis, MO) was used and detected by the goat-anti mouse Alexa-488 secondary antibody.

2.2.5. Inhibition experiments

Rat monoclonal antibody against E-cadherin (DECMA-1) (Abcam, Cambridge, MA) was added to media at 12 µg/mL. Blebbistatin (Sigma) was added to media at 10 µM. Media containing DECMA-1 or blebbistatin was refreshed every day.

2.3. Results and Discussion

Before plating hESCs on the PDMS micropost array, we first used microcontact printing to coat the tops of the PDMS microposts with vitronectin, which has been proved supportive for self-renewal of hESCs [57]. hESCs were further cultured in a chemically defined serum-free medium to establish a fully defined culture system [55, 58]. For all experiments two hESC lines,

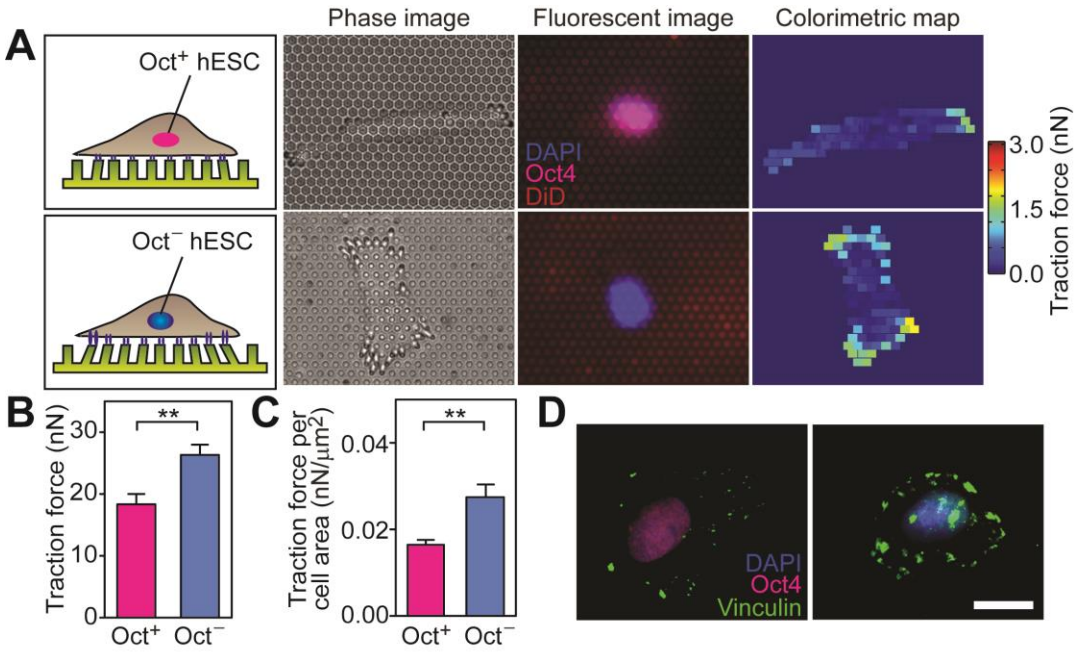

Figure 2-1 Differential cytoskeleton contractility and FA distribution for single Oct+ and Oct- hESCs. (A) Quantification of subcellular traction forces for single Oct+ (top row) and Oct- (bottom row) hESCs using the PDMS micropost array. (B&C) Bar plots of total traction forces per cell (B) and traction force per cell area (C) for both single Oct+ and Oct- hESCs. Data represents the means ± s.e.m from 3 independent experiments. **, $p < 0.01$. (D) Immunofluorescence images showing FA distributions in single hESCs (left: Oct+; right: Oct-), as indicated by vinculin staining. Scale bar, 20 µm.

H1 and H9, were used with similar results.

Since mechanosensing of matrix rigidity involves cytoskeleton contractility in mESCs and other multipotent adult stem cells, we decided to investigate whether there would be a correlation between stemness of single hESCs and their cytoskeleton contractility, by examining simultaneously expressions of Oct4 (a nuclear transcription factor and hallmark of stemness) in hESCs and their traction forces (Figure 2-1). Undifferentiated hESCs, confirmed using flow

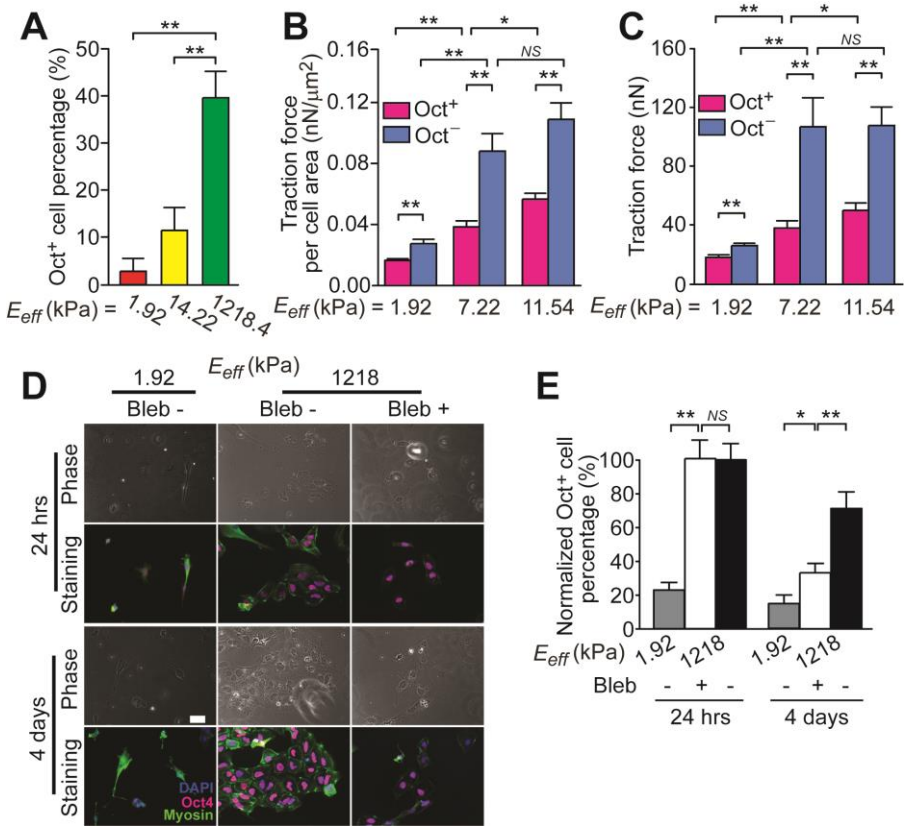

Figure 2-2 Matrix mechanic-mediated behaviors of single hESCs on PDMS micropost arrays with different rigidities. (*A*) Bar plot of percentage of Oct^+ cells for single hESCs plated on the PDMS micropost arrays with different rigidities. (*B&C*) Traction force per cell area (*B*) and total traction forces per cell (*C*) for both Oct^+ and Oct^- cells as a function of the PDMS micropost array rigidity. (*D*) Phase contrast and immunofluorescence images of hESCs treated with or without blebbistatin on both soft (E_{eff} = 1.92 kPa) and rigid (E_{eff} = 1,218.4 kPa) PDMS micropost arrays. Scale bar, 50 μm. (*E*) Bar plot of percentage of Oct^+ cells for blebbistatin treated hESCs and untreated controls as a function of the PDMS micropost array rigidity. Data in *E* was normalized to the value for untreated hESCs plated on the rigid micropost array under the 24-hr treatment condition. Data in *A-C* and *E* represents the means ± s.e.m from 3 independent experiments. *: $p < 0.05$; **: $p < 0.01$; *NS*: $p > 0.05$.

cytometry analysis of SSEA-3 positive cells with a purity of 95.90%, were seeded as single cells in the complete culture medium containing basic fibroblast growth factor (bFGF) on the PDMS micropost array with the post diameter D of 1.83 μm, the height L of 12.9 μm, and the effective modulus E_{eff} of 1.92 kPa. Live-cell traction forces as well as the percentage of Oct4 positive (Oct^+) cells, defined as the ratio of Oct^+ cells to the total cell number, were quantified 24 hrs after plating (Figure 2-1 and Figure 2-2A). It was noticeable that within 24 hrs on the PDMS micropost array, 25.6% ± 3.8% of single hESCs lost expression of Oct4, suggesting spontaneous differentiation. A similar level of spontaneous differentiation (16.1% ± 2.0%) was also observed for single hESCs plated on control vitronectin-coated tissue culture plates (with the *Young*'s modulus E of 10^6 kPa). Quantification of live-cell traction forces of hESCs on the PDMS microposts showed strong positive correlations between total traction force per cell and cell spread area for both undifferentiated (Oct^+) and differentiated (Oct^-) hESCs (Figure 2-3), similar to our previous observations with adult stem cells [31]. This observation suggested that total traction force per cell normalized by cell spread area could be used as a suitable indicator to gauge the mechanical state of single hESCs. The evaluation of cytoskeleton contractility indicated a significant difference between Oct^+ and Oct^- cells, as Oct^+ hESCs showed significantly less total traction force per cell (Figure 2-1*B*) and total traction force per cell area (Figure 2-1*C*) as compared to Oct^- cells. Vinculin, a FA protein, was used to examine the functional role of FAs in regulating the mechanosensitivity of hESCs (Figure 2-1*D*). Vinculin-expressing FAs appeared to be concentrated on the cell periphery of Oct^+ hESCs, while for Oct^- cells FAs were randomly distributed across the cell spreading area. Taken together, our results in Figure 2-1 suggested that cytoskeleton contractility and FA formation might be intrinsic mechanical properties of hESCs correlating closely with their pluripotent state.

Next we investigated whether single hESCs could sense and respond to changes in matrix mechanics using PDMS micropost arrays with different rigidities, and whether matrix rigidity could influence pluripotency of hESCs. Here we used a modified culture condition to challenge the self-renewal of hESCs by removing bFGF from the complete culture medium. Undifferentiated hESCs were first seeded in complete medium onto three different PDMS micropost arrays with the same post diameter *D* of 1.83 μm but different post heights, whose effective modulus E_{eff} were 1.92 kPa (soft), 14.22 kPa (medium rigid) and 1,218.4 kPa (rigid), respectively. Twenty-four hours after seeding the complete culture medium was replaced with

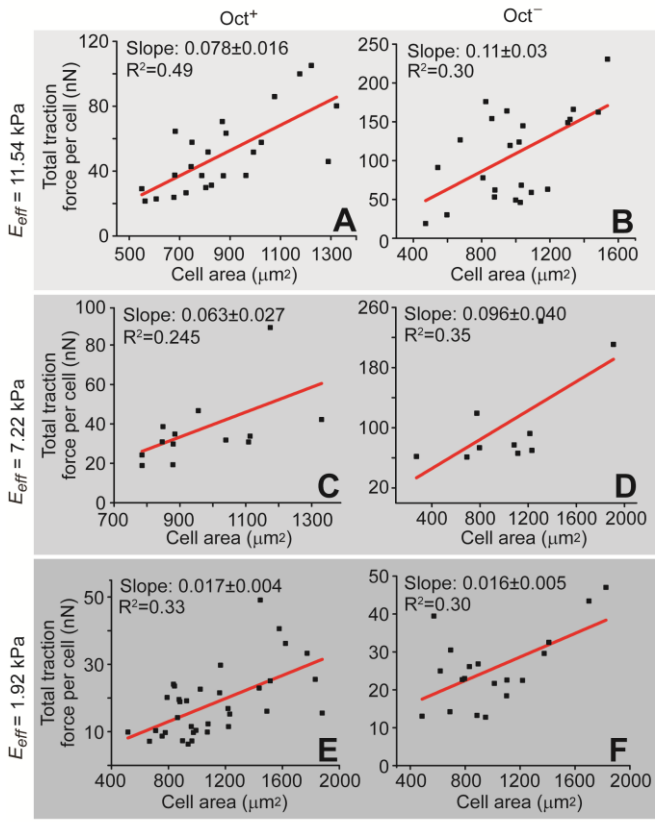

Figure 2-3 Correlative analysis of cell morphology and traction force for single Oct^+ (left) and Oct^- (right) hESCs during rigidity-sensing. Total traction force per single hESCs was plotted against hESC spread area. Each data point represents an individual cell. Data were collected from three different PDMS micropost arrays (Top row, *A&B*: E_{eff} = 11.54 kPa; Middle row, *C&D*: E_{eff} = 7.22 kPa; Bottom row, *E&F*: E_{eff} = 1.92 kPa). Data trends were compared with the linear least square fitting (red lines, with the slope and R^2 values indicated).

the bFGF-free medium, and hESCs were cultured for another 24 hrs before analyzing their Oct4 expressions. Under the bFGF-free condition, we observed a significant decrease of the percentage of Oct^+ cells as compared to the full medium condition. However, matrix rigidity appeared to play a significant role in regulating pluripotency of hESCs, as 39.5% ± 5.5% of single hESCs on the rigid PDMS micropost array remained as undifferentiated Oct^+ cells, while on the medium rigid and soft PDMS micropost arrays, only 11.6% ± 4.8% and 2.8% ± 2.6% of hESCs were Oct^+, respectively (Figure 2-2*A*). To investigate whether matrix mechanics-mediated Oct4 expression in single hESCs was correlated with endogenous cytoskeleton contractility, cellular traction forces of both Oct^+ and Oct^- cells were measured using PDMS micropost arrays with an E_{eff} ranging from 1.92 to 11.54 kPa. As shown in Figure 2-2*B*&*C*, Oct^- cells consistently showed greater cytoskeleton contractility than Oct^+ cells, regardless the micropost rigidity E_{eff}. Furthermore, both Oct^+ and Oct^- cells increased their cytoskeleton contractility with E_{eff}. Together, our results in Figure 2-2 suggested that hESCs are mechanosensitive and rigid substrates are supportive for pluripotency maintenance of single hESCs. Our data also showed that increasing matrix rigidity might lead to stronger cytoskeleton contractility in hESCs as reflected by their greater traction forces measured by the PDMS micropost arrays [59].

Recent studies have indicated a functional role of nonmuscle myosin II activity in regulating the fate decision of hESCs [60, 61]. Mechanosensing of matrix rigidity by adherent mammalian cells also involves actomyosin-mediated cytoskeleton contractility [34, 45]. Thus, we decided to examine the functional role of nonmuscle myosin II activity on rigidity-dependent self-renewal of hESCs. hESCs were seeded as single cells on the PDMS micropost arrays of different rigidities at 3,000 cells/cm^2 in the complete cell medium. Twenty four hours after cell

seeding, the complete culture medium was replaced with the bFGF-free medium supplemented with 10 μM blebbistatin, a small molecule that inhibits specifically nonmuscle myosin II activity. Blebbistatin treatment for 24 hrs had no significant effect on pluripotency maintenance of hESCs on the rigid PDMS micropost array (Figure 2-2 *D*&*E*). However, a prolonged 4-day treatment of hESCs with blebbistatin resulted in loosely connected single hESCs and a significant decrease in cell density and the percentage of Oct^+ cells (Figure 2-2 *D*&*E*). No compact and sharp edged colonies could be observed for blebbistatin-treated cells, in distinct contrast to compact colonies formed by untreated controls. Our observations in Figure 2-2 *D*&*E* were consistent with recent studies reporting that the effect of blebbistatin treatment on hESC self-renewal might be time-dependent, and long-term exposure to blebbistatin could inhibit cell division and thus negatively impact hESC self-renewal [60, 61].

Blebbistatin-treated single hESCs on the rigid PDMS micropost array appeared to behave differently from untreated cells on the soft micropost array, under both 24-hr and 4-day treatment conditions with blebbistatin (Figure 2-2*E*). This observation suggested that although it is known that actomyosin activity can be down-regulated for mechanosensitive adherent cells plated on soft substrates, other molecular mechanisms might also exist and work in parallel to transduce the rigidity signal to regulate stem cell fate, such as integrin-mediated adhesion signaling [34, 62].

We further investigated mechanosensitivity of small aggregates of hESCs (containing n = 2-5 cells). hESCs were seeded at a high density (8,000 cells/cm^2) on different PDMS micropost arrays with E_{eff} ranging from 1.92-1,218.4 kPa in the complete culture medium. Live-cell traction force measurements were performed 24 hrs after cell seeding (Figure 2-4), and percentages of Oct^+ cells were quantified on different PDMS micropost arrays. Under this

condition, single cells and doublets did not show significant differences on different PDMS micropost arrays with regard to their Oct4 expressions. However, it appeared that larger aggregates of hESCs (n > 2 cells) had a greater tendency to differentiate on softer micropost arrays while maintaining their Oct4 expressions on more rigid ones (Figure 2-5*A*). Our live-cell traction force results in Figure 2-5*B* also showed that the average total traction force per cell for hESCs plated on the same PDMS micropost array (with E_{eff} = 1.92 kPa) was not significantly different among single cells, doublets or triplets, for both Oct^+ and Oct^- cells, suggesting that cell-cell contact might play an important role in regulating matrix mechanics-mediated

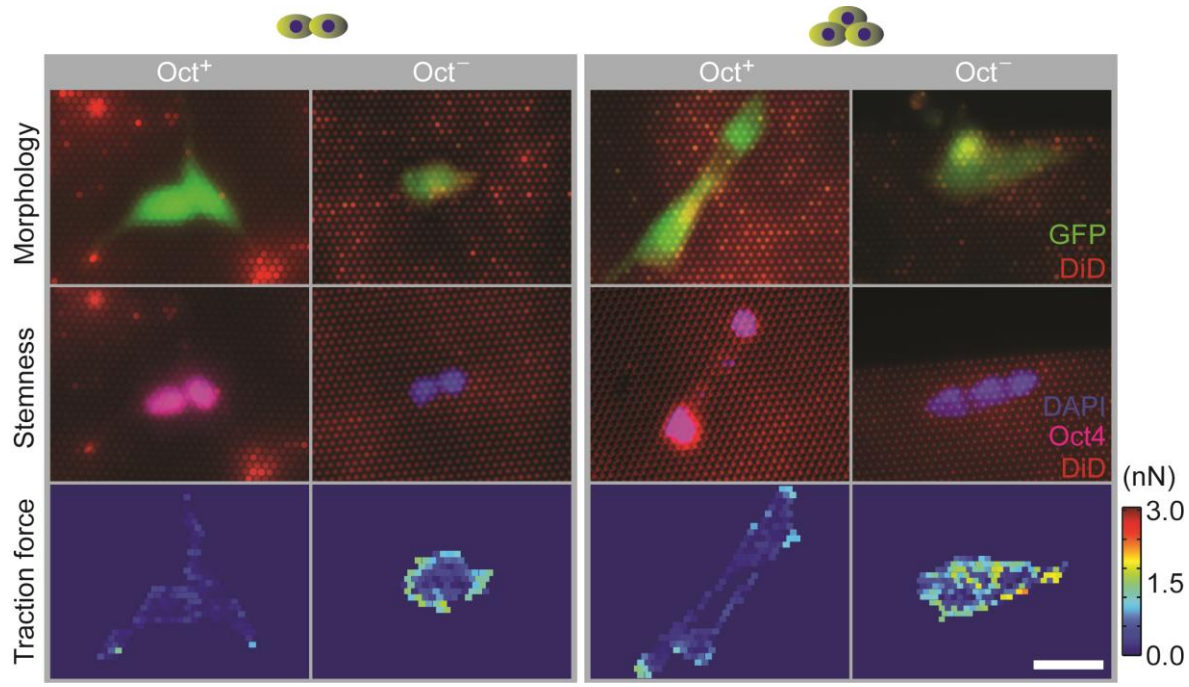

Figure 2-4 Representative fluorescence images showing measurements of traction forces for small aggregates of Oct+ and Oct- hESCs plated on the PDMS micropost array.

pluripotency maintenance of hESCs. To examine the FA distribution in small aggregates of hESCs, immunostaining of vinculin was performed (Figure 2-5*C*). Our staining images showed that similar to results for single hESCs in Figure 2-5*D*, vinculin-expressing FAs were

concentrated on the cell periphery of clustered Oct$^+$ hESCs, while for clustered Oct$^-$ cells, FAs were randomly distributed across the cell spreading area.

It was interesting to observe that there was a lack of response of single hESCs to rigidity changes in Figure 2-5*A*, which might be due to the fact that bFGF in the complete culture medium might have activated mechanotransductive signaling cascades downstream of rigidity

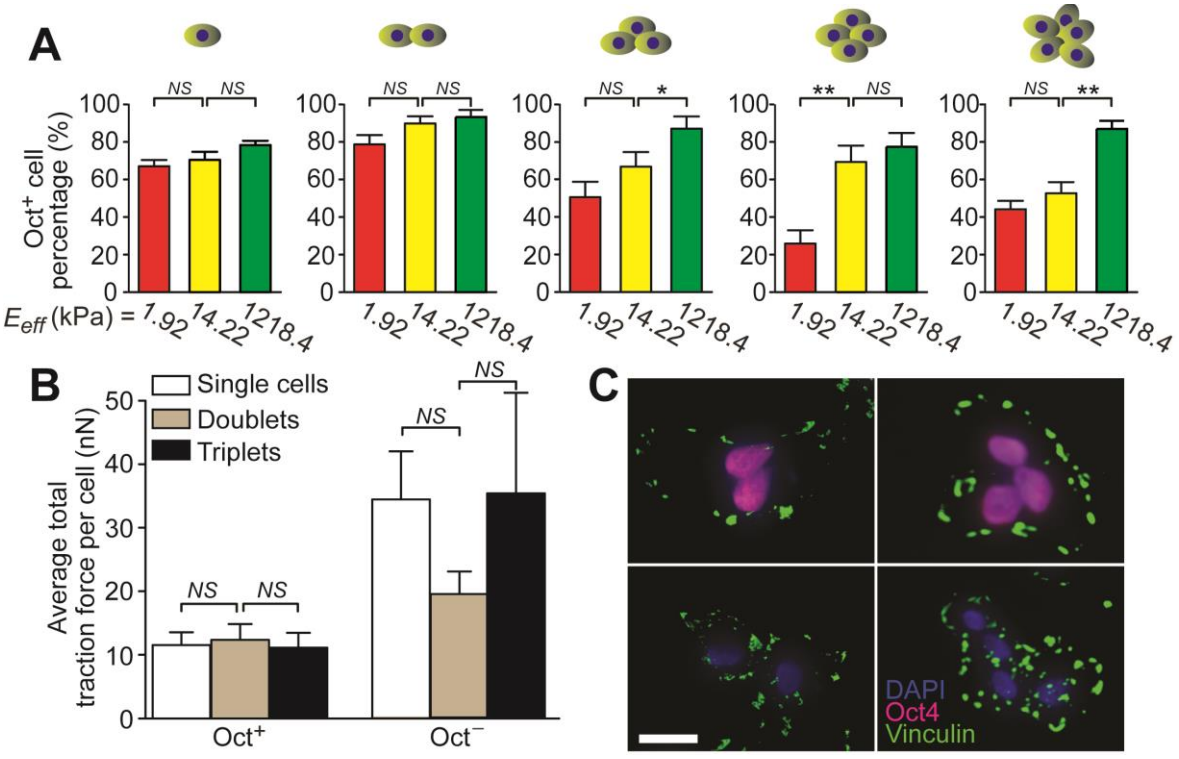

Figure 2-5 Matrix mechanics-mediated cellular functions of small aggregates of hESCs on PDMS micropost arrays with different rigidities. (*A*) Bar plots of percentage of Oct$^+$ cells for clustered hESCs of different sizes as a function of the PDMS micropost rigidity. (*B*) Plot of average total traction force per cell for both Oct$^+$ and Oct$^-$ cells contained in different sized hESC aggregates. Data in *A* & *B* represents the means ± s.e.m from 3 independent experiments. *: $p < 0.05$; **: $p < 0.01$; *NS*: $p > 0.05$. (*C*) Immunofluorescence images showing FA distributions in Oct$^+$ (top) and Oct$^-$ (bottom) hESC aggregates, as indicated by vinculin staining. Scale bar, 25 μm.

sensing of single hESCs. Future studies might be necessary to elucidate the convergence and cross-talk of different well-conserved soluble factor-mediated signal transduction pathways and the cellular mechanosensing and mechanotransduction processes to activate the elaborate intracellular signaling network in an integrated and interacting manner to regulate hESC fate.

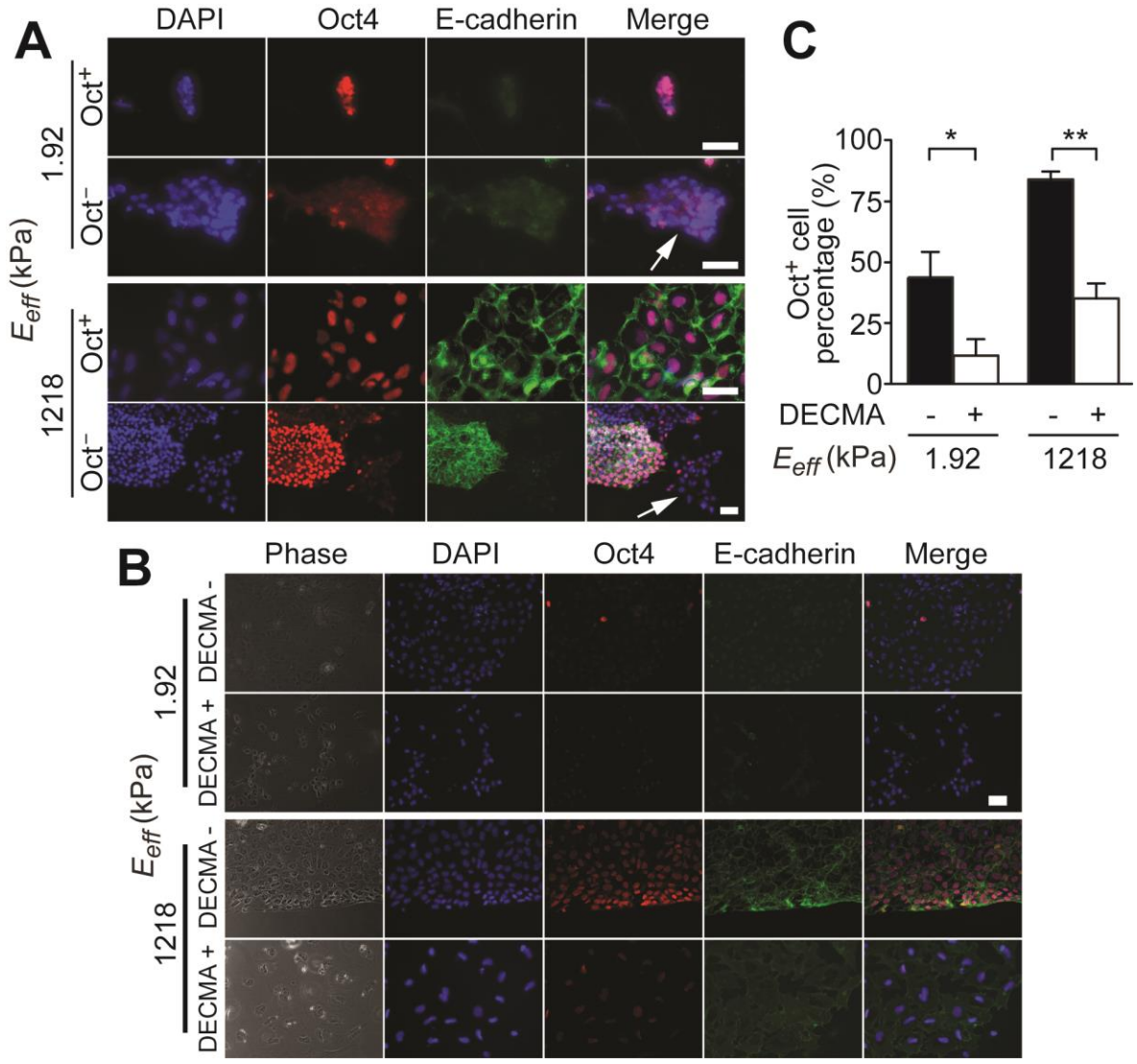

Figure 2-6 E-cadherin expression of hESCs modulated by substrate rigidity. (*A*) Immunofluorescence images taken for undifferentiated (Oct^+) and differentiated (Oct^-) hESC colonies on soft (E_{eff} = 1.92 kPa) and rigid (E_{eff} = 1,218.4 kPa) PDMS micropost arrays, as indicated. Differentiated hESC colonies were marked with an arrow. Scale bars, 50 µm. (*B*) Phase contrast and immunofluorescence images of hESCs treated with or without DECMA-1 on both soft (E_{eff} = 1.92 kPa) and rigid (E_{eff} = 1,218.4 kPa) PDMS micropost arrays. Scale bar, 50 µm. (*C*) Bar plot of percentage of Oct^+ cells for DECMA-1 treated hESCs and untreated controls as a function of the PDMS micropost rigidity. Data represents the means ± s.e.m from 3 independent experiments. *: $p < 0.05$; **: $p < 0.01$.

Recent studies have shown that actomyosin-mediated cytoskeleton contractility and E-cadherin expression form a positive feedback loop to promote maintenance of pluripotency of hESCs [61]. Thus, in hESC aggregates with cell-cell contacts, E-cadherin expression might be correlated with CSK contractility, expression of Oct4 and pluripotency of hESCs. To examine

this possibility, single hESCs were plated at 8,000 cells/cm^2 in the complete medium on the soft (E_{eff} = 1.92 kPa) and rigid (E_{eff} = 1,218.4 kPa) PDMS micropost arrays. Twenty-four hours after seeding, cells were co-stained for E-cadherin and Oct4. Co-expressions of Oct4 and E-cadherin were detected in Oct$^+$ hESCs on the rigid micropost array, while E-cadherin was not detectable in Oct$^-$ cells on the rigid micropost array (Figure 2-6*A*). In comparison, hESCs plated on the soft micropost array expressed very low levels of E-cadherin, regardless of their Oct4 expressions (Figure 2-6*A*).

To examine the functional role of E-cadherin in mediating rigidity-dependent self-renewal of hESCs, we performed E-cadherin inhibition assays for hESCs cultured on both the soft (E_{eff} = 1.92 kPa) and rigid (E_{eff} = 1,218.4 kPa) PDMS micropost arrays. hESCs were treated with or without DECMA-1, an antibody that blocks E-cadherin activity [61], for 5 days before cells were fixed and stained for E-cadherin and Oct4. Blocking E-cadherin activity in hESCs on both the rigid and soft micropost arrays by DECMA-1 resulted in loosely connected single cells as compared to compact and sharp edged colonies for untreated controls (Figure 2-6*B*). Percentages of Oct$^+$ cells also decreased significantly for DECMA-1 treated hESCs as compared to untreated controls, regardless the micropost rigidity E_{eff} (Figure 2-6*C*). Together, our findings in Figure 2-6 supported a possible involvement of E-cadherin in rigidity-dependent self-renewal of hESCs. Our results, combined with the evidence that inhibition of E-cadherin leads to loss of hESC pluripotency[61, 63] and over-expression of E-cadherin promotes hESC self-renewal[64], strongly suggest that for hESC colonies where E-cadherin-mediated cell-cell contacts have been established, matrix mechanics-mediated cytoskeleton tension may help stabilize the OCT4-SOX2-NANOG circuitry, possibly by regulating the E-cadherin-mediated intercellular adhesion.

In this work, our results demonstrated that cytoskeleton contractility, focal adhesion formation, and E-cadherin expression were all critically involved in mechanoresponsive differentiation of hESCs. Specifically, hESCs were mechanosensitive and increased their cytoskeleton contractility with matrix rigidity, and rigid substrates were supportive for maintenance of pluripotency of hESCs. Matrix mechanics-mediated cytoskeleton contractility might be functionally correlated to E-cadherin expressions in cell-cell contacts and involved in fate decisions of hESCs. Our results highlighted the important functional link between matrix rigidity, cellular mechanics, and pluripotency of hESCs. In addition, our micropost array system provided a novel approach to characterize and understand mechanotransduction and its involvement in hESC function. Advancing understanding of mechanoresponsive behaviors of hESCs will help in the design of biologically inspired *in vitro* cellular microenvironments to guide growth, differentiation, and functional assembly of hESCs.

Chapter 3

Hippo/YAP-mediated rigidity-dependent motor neuron differentiation of human pluripotent stem cells

The major content of this chapter is reproduced from our previously published papers: "Hippo/YAP-mediated rigidity-dependent motor neuron differentiation of human pluripotent stem cells" in *Nature Materials*, 2014 [37] and "Harnessing mechanobiology of human pluripotent stem cells for regenerative medicine" in *ACS Chemical Neuroscience*, 2015 [38].

3.1. Introduction

Mechanics and forces are known to play important roles in embryogenesis [65]. Given that hPSC differentiation follows developmental principles, it is not at all surprising that mechanical cues can regulate lineage commitment and differentiation of hPSCs. Zoldan *et al.* have cultured embryonic bodies (EBs) in three dimensional scaffolds with their bulk rigidity engineered to model that found in specific germlayers *in vivo*. Differentiation of hESCs in the EBs to endoderm, mesoderm, and ectoderm germlayers was shown to be promoted by a different rigidity threshold of the scaffold [66]. Specifically, their results have demonstrated that high, intermediate, and low elastic moduli of the scaffolds promote mesodermal, endodermal and ectodermal differentiation, respectively, as evidenced by upregulated expressions of genes representative of the three germ layers. A more definitive study on the mechanoresponsive hPSC differentiation has been demonstrated recently by Keung *et al.*, where the authors have

investigated the effect of substrate mechanics on neural induction of hESCs and hiPSCs. Matrigel coated PA gels with the bulk rigidity in the range of 100 Pa - 700 Pa were shown to promote neural induction under a culture condition for dual inhibitions of TGF-β and BMP4 signalling, a well-established neural induction culture for the monolayer culture system [67]. Specifically, soft PA gels were shown to upregulate expressions of multiple neuroepithelial markers such as Pax6, Sox1 and even some markers of the later stage neurogenic differentiation such as Tuj-1 in hPSCs after culturing the cells for 9 days on the PA gels. Interestingly, Keung *et al.* have further shown that a short 5-day soft stiffness "pulse" treatment for hPSCs before neural patterning can promote their neural induction to the same extend as a 9-day "pulse". Keung *et al.* have also studied whether soft PA gels promote the maturation of dopaminergic neurons. They passaged the neural progenitor cells induced after 9 days of culture on PA gels of different rigidities to glass chamber wells for additional 10 days to allow for neuronal maturation. They observed that while a greater number of dopaminergic neurons were obtained from neural progenitor cells on soft PA gels, the ratio between the dopaminergic neurons and Tuj-1-positive neural cells remained about the same. The results reported by Keung *et al.* suggest that mechanosensitivity of hPSCs in the initial neural induction phase may not be preserved in the later neuronal differentiation and maturation. We have also recently shown that hESCs cultured on soft micropost arrays are more sensitive to caudalization signals induced by retinoic acid with increased expressions of Sox1 and Islet1/2 (a transcription factor found in motor neurons) in hESCs as compared to the cells cultured on rigid micropost arrays and tissue culture plates [35]. All together, these results strongly support that matrix rigidity can influence neural differentiation of hPSCs in multiple stages, from initial neural induction to primitive neural progenitor cells to the later stage specification and maturation.

Progressive degeneration and death of spinal cord motor neurons (MNs) are associated with fatal neurological diseases such as spinal muscular atrophy (SMA) and amyotrophic lateral sclerosis (ALS). Our limited understanding of the complicated and diverse neuropathologies of these debilitating diseases has significantly hindered developments of effective strategies for clinical intervention and treatments. While mutation in survival of motor neuron-1 (SMN1) gene has been identified responsible for the majority of patients afflicted with SMA, about 80% of ALS cases do not have a genetic origin. Several genes including SOD1, TDP43, and FIG4 are found to be associated with the remainder 20% familial ALS cases, although a detailed mechanism of these mutations leading to ALS is still unclear [68]. Moreover, the available animal models for studying ALS do not completely recreate the human disease. Consequently, none of the drugs tested effective in animal models has been proven effective for treating ALS patients.

Recent advances in human pluripotent stem cells (hPSCs) including human embryonic stem cells (hESCs) and human induced pluripotent stem cells (hiPSCs) have opened exciting new doors for treating MN-associated neurodegenerative diseases. hPSCs have unlimited self-renewal capability *in vitro*, critical for generating enough cells for large-scale cell-based applications. Furthermore, hPSCs have the important potential to differentiate into various stages of progenitors with distinct epigenetic and transcriptional statuses, allowing selection of optimal cell types for stem cell-based transplantation therapies. Current stem cell-based clinical trials for treating MN-associated neurodegenerative diseases mainly use human adult stem cells including human spinal stem cells and human mesenchymal stem cells [69]. Although adult stem cells can provide a supportive environment to remaining neurons in the diseased host, in many cases they fail to generate new functional neurons that can rescue neuronal circuit or form

neuromuscular junctions. Moreover, hPSCs, especially patient-derived hiPSCs, may drastically change the way of drug discovery efforts by eliminating the genetic and anatomical differences between human and animals while offering exciting promise for personalized medicine and understanding patient-specific basis of disease.

All potential applications of hPSCs for treating MN-associated neurodegenerative diseases require large-scale manufacturing of clinical-grade neural stem cells and MNs. However, current approaches for deriving MNs are inefficient and time consuming, presenting a significant technical hurdle for cell-based drug screening and transplantation applications. Most current approaches for *in vitro* derivation of MNs in some way mimic the process of neurogenesis during development, requiring inhibition of BMP signaling for neuroepithelial fate induction before activation of caudalization and ventralization signals using morphogens such as fibroblast growth factors (FGFs), retinoic acid (RA), and sonic hedgehog (SHH). To recapitulate neuronal development, either recombinant proteins (such as noggin) or BMP receptor inhibitors (such as LDN193189) has been applied in hPSC culture to inhibit BMP signaling. Similarly, RA, SHH, and purmorphamine (Pur) have been employed for anterior-posterior and dorsal-ventral patterning of neural progenitor cells. However, BMP inhibitors are dispensable if embryonic bodies are used for neural differentiation of hPSCs, and RA-independent MN specification has also been reported recently [70, 71]. Therefore, our understanding of the regulatory network controlling MN differentiation remains incomplete.

Over the last few years, there is a significant surge of interest in investigating the effect of the physical aspect of cell microenvironment on controlling stem cell fate [1, 15]. Indeed, mechanoresponsive behaviors of human adult stem cells including hematopoietic, mesenchymal, neural, and skeletal muscle stem cells have been well documented recently [30, 32, 33, 45, 72].

Furthermore, evidence gathered from studies with mouse ESCs (mESCs) has supported the notion that like many adult stem cells, ESCs may also be intrinsically mechanosensitive. For example, soft hydrogels are found to be conductive for stemness maintenance of mESCs, and on rigid substrates osteogenic differentiation of mESCs is promoted [46, 47]. Furthermore, applying local cyclic stress using magnetic beads to mESCs *via* integrin-mediated focal adhesions can result in loss of pluripotent markers [44]. These important findings have shed light on the importance of biophysical cues in the local cell microenvironment (*i.e.*, rigidity and mechanical force) during embryonic development and for improving *in vitro* culture of ESCs.

3.2. Materials and Methods

3.2.1. Fabrication and surface functionalization of PDMS micropost arrays (PMAs)

The PDMS micropost arrays (PMAs) were batch fabricated using microfabrication techniques including photolithography, deep reactive ion etching (DRIE), and replica molding, as described previously [54]. The design of the Si micropost array master reported previously was ideal for single-cell assays such as traction force measurements [54]. To facilitate large-scale hPSC culture as well as standard biological assays, in this work the design of the Si master was modified, so that the total surface area of supporting structures (circular pillars, with a diameter of 30 μm) surrounding 1 mm × 1 mm square-shaped micropost arrays occupied < 1% of the total surface area of microposts. In most experiments, the PMAs were fabricated onto 18-mm round coverslips before transferred to standard 12-well tissue culture plates. To promote cell attachment, the top surface of the PMA was functionalized with vitronectin (Trevigen) using

microcontact printing as described previously [54]. It has been reported that vitronectin can support self-renewal of hESCs [57].

To facilitate adoption of PMAs by other researchers, we will provide a resource to distribute PMAs to any interested scientist for their research.

3.2.2. Culture medium conditions

Growth media contained DMEM/F12 (GIBCO), 20% KnockOut serum replacement (GIBCO), 0.1 mM β-mercaptoethanol (GIBCO), 2 mM glutamax (GIBCO), 1% non-essential amino acids (GIBCO), and 4 ng mL^{-1} human recombinant basic fibroblast growth factor (bFGF; GlobalStem).

Neural induction media: Growth media were used as neural induction media from day 1 to day 3. N2 media containing DMEM/F12, 1% N2 supplement (GIBCO), 2 mM glutamax, and 1% non-essential amino acid were used to gradually replace growth media from day 4 as following: 25% N2 media and 75% growth media at day 4, 50% N2 media and 50% growth media at day 5 and 6, 75% N2 media and 25% growth media at day 7, 100% N2 media at day 8. To promote neural induction, TGF-β inhibitor SB 431542 (10 μM; Cayman Chemical) and BMP4 inhibitor LDN 193189 (0.1 μM, unless stated otherwise; Selleckchem) were added into neural induction media from day 1.

Motor neuron (MN) differentiation media contained N2 media supplemented with 1 μM retinoic acid (RA; Cayman Chemical), 1 μM purmorphamine (Pur; Cayman Chemical), and 20 ng mL^{-1} bFGF.

Motor neuron (MN) maturation media contained basal media that was a 1:1 mixture of N2 and B-27 media. B-27 media contained neurobasal media (GIBCO), 2% B-27 supplement

(GIBCO), and 2 mM Glutamax. The following chemicals were added to basal media freshly before each medium change: 10 ng mL^{-1} brain-derived neurotrophic factor (BDNF; R&D systems), 10 ng mL^{-1} insulin-like growth factor 1 (IGF-1; Peprotech), 1 μM cyclic adenosine monophosphate (cAMP; Sigma), 0.2 μg mL^{-1} ascorbic acid (Sigma), 0.1 μM RA, and 1 μM Pur.

All the media were pre-equilibrated at 37°C in 5% CO_2 before use.

3.2.3. Cell culture

hESC line H1 (WiCell) was cultured on mitotically inactive mouse embryonic fibroblasts (MEFs; GlobalStem) in growth media with daily medium change. Cells were passaged every 5 d using the STEMPRO EZPassage Disposable Stem Cell Passaging Tool (Invitrogen). Before passaging, differentiated cells were removed manually using a modified pasteur pipette under a stereomicroscope (Olympus). Cells were rinsed briefly with PBS and treated with TrypLE Select (Invitrogen) for 2 min to release MEFs. Cells were rinsed briefly again with PBS before all cells, including hESCs and remaining MEFs, were collected using a cell scraper (BD Biosciences). To remove contaminant MEFs, all cells were transferred onto a 60-mm tissue culture dish (BD Biosciences) coated with gelatin (Sigma) and incubated for 45 min. MEFs would attach to the dish while hESCs were still in the supernatant. hESCs in the supernatant were collected and centrifuged with the cell pellet re-dispersed in growth media containing Y27632 (10 μM; Enzo Life Sciences).

Both hESC line CHB-10 (Children's Hospital Corp., Boston, MA) and hiPSC line were cultured on poly[2-(methacryloyloxy)ethyl dimethyl-(3-sulfopropyl)ammonium hydroxide] (PMEDSAH) in human cell conditioned media (GlobalStem) as described previously[55], before seeded onto the PMA by digesting in TrypLE Select. The hiPSC line was derived from human

foreskin fibroblasts by over-expression of *Oct4*, *Sox2*, *Klf4*, and *c-Myc* using the Sendai virus constructs (Invitrogen).

When cell passaging was needed for neuroepithelial cells (NEs), cells were first cut into small cell aggregates using the STEMPRO EZPassage Disposable Stem Cell Passaging Tool or dispase (STEMCELL Technologies) before transferred onto new substrates *en bloc*.

3.2.4. Immunocytochemistry

Cells were fixed with 4% paraformaldehyde (Electron Microscopy Sciences) for 15 min and then permeabilized with 0.1% Triton X-100 (Roche Applied Science) for 20 min at room temperature. Primary antibodies were used and detected by goat-anti mouse Alexa Fluor 488 and/or goat-anti rabbit Alexa Fluor 546 secondary antibodies, except for ChAT staining, which was detected using FITC conjugated bovine-anti goat secondary antibody (Santa-Cruz Biotechnology). Alexa Fluor 555 conjugated phalloidin (Invitrogen) was used for visualization of actin microfilaments. Percentage of marker-positive cells was quantified with a custom-developed MATLAB program (MathWorks) based on a watershed segregation algorithm.

3.2.5. RNA isolation and quantitative real-time PCR (qRT-PCR) analysis

Total RNA was isolated from cells using TRIzol (Invitrogen) or RNeasy kit (Qiagen). Real-time PCR (RT-PCR) was performed and monitored using an ABI 7300 system (Applied Biosystems). Quantitative real-time PCR (qRT-PCR) was also performed with either Taqman-probes (for gene expression analysis) or SYBR Green PCR mastermix (for siRNA knockdown). Human GAPDH or 18S primers were used as an endogenous control for relative quantifications. Samples in which no expression was detected were given an arbitrary Ct value of 40. All

analyses were performed with three replicates. Relative expression levels were determined by calculating $2^{-\Delta\Delta Ct}$ with the corresponding s.e.m.

3.2.6. Western blotting

Whole cell lysates were prepared from cells, separated on SDS-polyacrylamide gel, and transferred to PVDF membranes. NE-PER nuclear and cytoplasmic extraction kit (Thermo Scientific) was used to obtain cytoplasmic and nuclear protein fractions. PVDF membranes were incubated with blocking buffer (Li-Cor) for 1 hr and then incubated with primary antibodies overnight at 4^{o}C. Blots were then incubated with IRDye secondary antibodies (Li-Cor) for 1 hr before protein expression was detected with a Li-Cor Odyssey Sa Infrared Imaging System (Li-Cor).

3.2.7. siRNA knockdown

hESCs cultured on vitronectin coated 6-well plates were transfected using DharmaFECT 1 (Thermo Scientific). Briefly, cells were plated at 80% confluence and subjected to transfection the next day (or day 0) using 25 nM final concentration of siRNA. After 24 hrs, transfected cells were passaged onto the PMA for downstream assays. Two additional siRNA treatments were performed at day 2 and 4. siRNA including Lats1 and scramble control (SMARTpool) was purchased from Dharmacon.

3.2.8. Scanning electron microscopy (SEM)

Samples for scanning electron microscopy were washed 3 times with 50 mM Na-cacodylate buffer (pH 7.3; Sigma-Aldrich), fixed for 1 hr with 2% glutaraldehyde (Electron

Microscopy Science) in 50 mM Na-cacodylate buffer, and dehydrated in a graded series of ethanol concentrations through 100% over a period of 1.5 hr. Dehydration in 100% ethanol was performed 3 times. After washing with 100% ethanol, dehydrated samples were dried with liquid CO_2 using a super critical point dryer (Samdri-PVT-3D; Tousimis). Samples were then mounted on stubs, sputtered with gold palladium, observed, and photographed under a Hitachi SU8000 ultra-high resolution SEM machine (Hitachi High Technologies America).

3.2.9. Whole-cell patch clamp recording

Whole-cell current clamp was performed for functional MNs derived from hESCs using pipette electrodes (resistance 3 - 5 MΩ) filled with the following: 140 mM K-gluconate, 4 mM NaCl, 1 mM EGTA, 2 mM $MgCl_2$, 0.39 mM $CaCl_2$, 2 mM ATP, 0.3 mM GTP and 20 mM Hepes (pH 7.2; free $[Ca^{2+}]_i \sim 100$ nM). The standard extracellular (bath) solution (modified Tyrode's solution) contained: 153 mM NaCl, 5 mM KCl, 2 mM $CaCl_2$, 1 mM $MgCl_2$, 20 mM Hepes, and 10 mM glucose (pH 7.4). Signals were amplified using an Axopatch 2A patch clamp amplifier, digitized with Digidata 1440 at 10 kHz, filtered at 2 kHz, and recorded with Clampex 10.3 acquisition system (Axon instruments). All experiments were conducted at room temperature, and all recordings were analyzed with pClamp 10.3 and Origin 8.0 (OriginLab). As described previously[73], only cells with stable resting membrane potentials < -50 mV were considered to be healthy and used for further recording. Spontaneous action potentials (APs) were recorded without current stimulus. Amplitude of APs was determined by averaging at least 20 APs. The instantaneous frequency change or spike frequency adaptation (SFA) and post-inhibitory rebound (PIR) AP were examined by injecting a depolarizing or hyperpolarizing current pulse, respectively.

3.3. Results and Discussion

The influence of substrate rigidity on neural induction of hPSCs was assessed using vitronectin-coated coverslips (with bulk modulus $E = 10^4$ kPa) and PMAs with a broad range of rigidities (E = 1.0 - 1,200 kPa). hESCs were seeded at 20,000 cells cm^{-2} on coverslips and PMAs in growth media (Figure 3-1). After 24 hr, hESCs were switched to neural induction media containing the dual Smad inhibitors, SB 431542 (SB, TGF-β inhibitor) and LDN 193189 (LDN, BMP4 inhibitor), to promote neural induction (Figure 3-2a) [74]. No significant difference in cell attachment was observed between coverslips and PMAs of different rigidities (not shown). On coverslips and PMAs with E = 1,200 kPa (rigid PMAs), hESCs spread to form monolayers, whereas on PMAs with $E \leq 5.0$ kPa (soft PMAs), hESCs spontaneously migrated toward each other to form compact clusters. Cell spreading and nucleus size of hESCs were significantly reduced on soft PMAs relative to on coverslips or rigid PMAs (referred to henceforth as controls; Figure 3-3a-c). Notably, within 24 hr, 22.3% ± 6.2% of hESCs on soft PMAs had differentiated, indicated by loss of Oct4 (pluripotency-associated transcription factor) expression, whereas only 4.9% ± 1.0% (coverslip) and 3.9% ± 0.4% (rigid PMA) of hESCs on controls started differentiating (Figure 3-3d).

Expression of the early neuroectodermal differentiation marker, Pax6, was used to monitor neural induction[75]. On soft PMAs, $Pax6^+$ neuroepithelial cells (NEs) appeared as early as day 4, and reached 95.1% ± 2.1% by day 8. In contrast, on controls, $Pax6^+$ NEs appeared at day 6 and constituted only 28.2% ± 10.8% (coverslip) and 33.4% ± 7.2% (rigid PMA) of total cells at day 8, respectively (Figure 3-3b,c) [76]. Immunoblots revealed higher Pax6 and Sox1 (neuroectodermal transcription factor) protein expression by hESCs on soft PMAs relative to controls (Figure 3-3d). Paralleling definitive neural stem cells in mouse embryos [77], $Pax6^+$

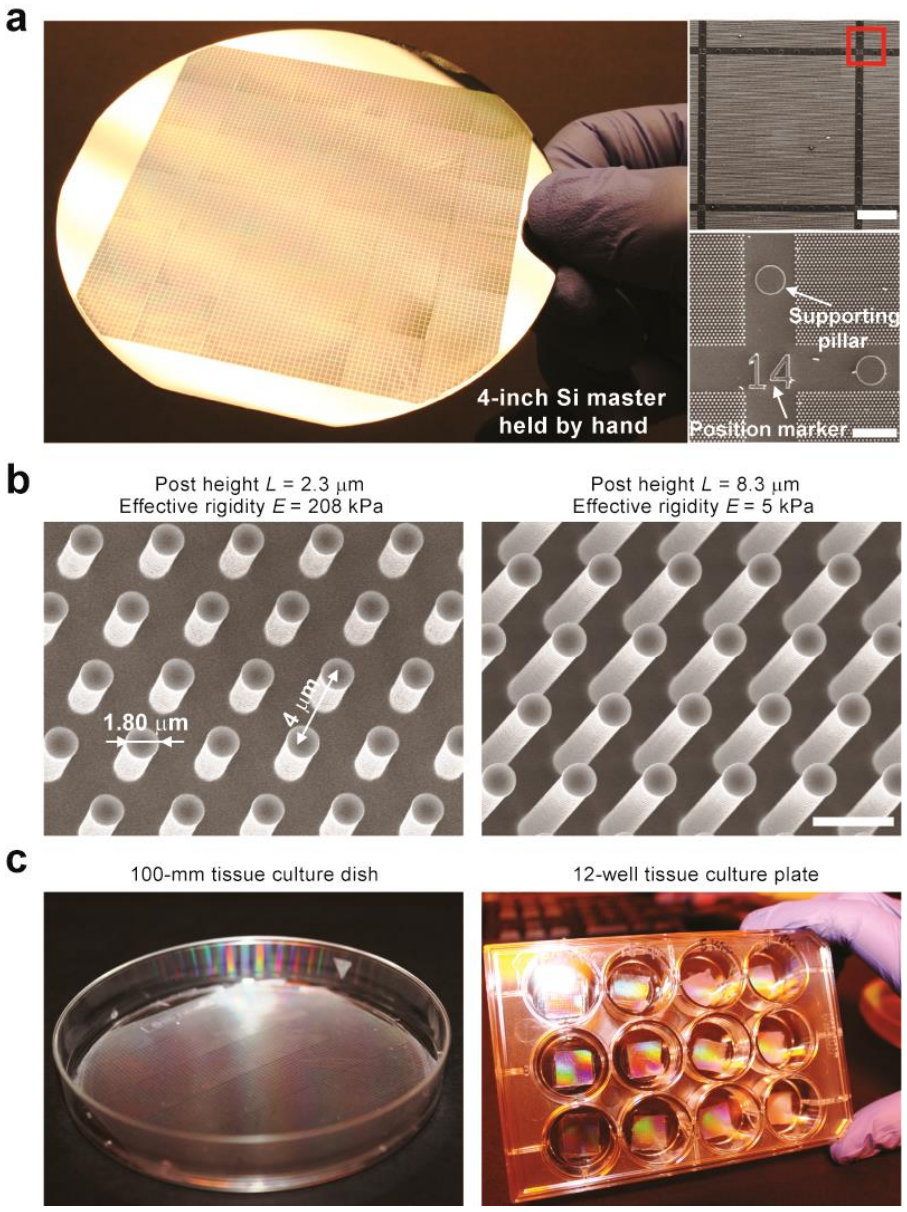

Figure 3-1 Batch microfabricated PDMS micropost arrays (PMAs) of large surface areas for hPSC culture. (**a**) Photograph (*left*) showing micropost array structures fabricated on a 4-inch Si wafer and SEM images (*right*) showing the layout of the micropost array surrounded by supporting pillars and position markers. The red rectangle in the top SEM image highlights the area in which the bottom SEM image was taken The total surface area of supporting pillars occupied < 1% of the total surface area of microposts. (**b**) High magnification SEM images showing arrays of hexagonally arranged circular Si microposts with different post heights. To modulate the effective rigidity E of the micropost array, the micropost height L was varied between < 1 μm to about 15 μm. PMAs generated in this work spanned a more than 1,000-fold range of rigidity from about 1.0 kPa to 1,200 kPa. (**c**) PMAs fabricated using replica molding from the Si micropost master could fit into different sized tissue culture dishes (with a diameter up to 100 mm; *left*) and 6- and 12-well tissue culture plates (*right*).

NEs derived from soft PMAs were responsive to bFGF and readily formed polarized neural tube-like rosettes, while the controls did not (Figure 3-4). Our screening assay revealed a threshold for neural induction of PMA rigidity E between 5 - 14 kPa: $E \leq 5$ kPa had a potent effect, whereas $E \geq 14$ kPa did not (Figure 3-5). Two sets of PMAs with different post geometries were compared, with results indicating that neural induction by soft PMAs was not sensitive to micropost geometries (Figure 3-6). By modulating PDMS curing agent to base

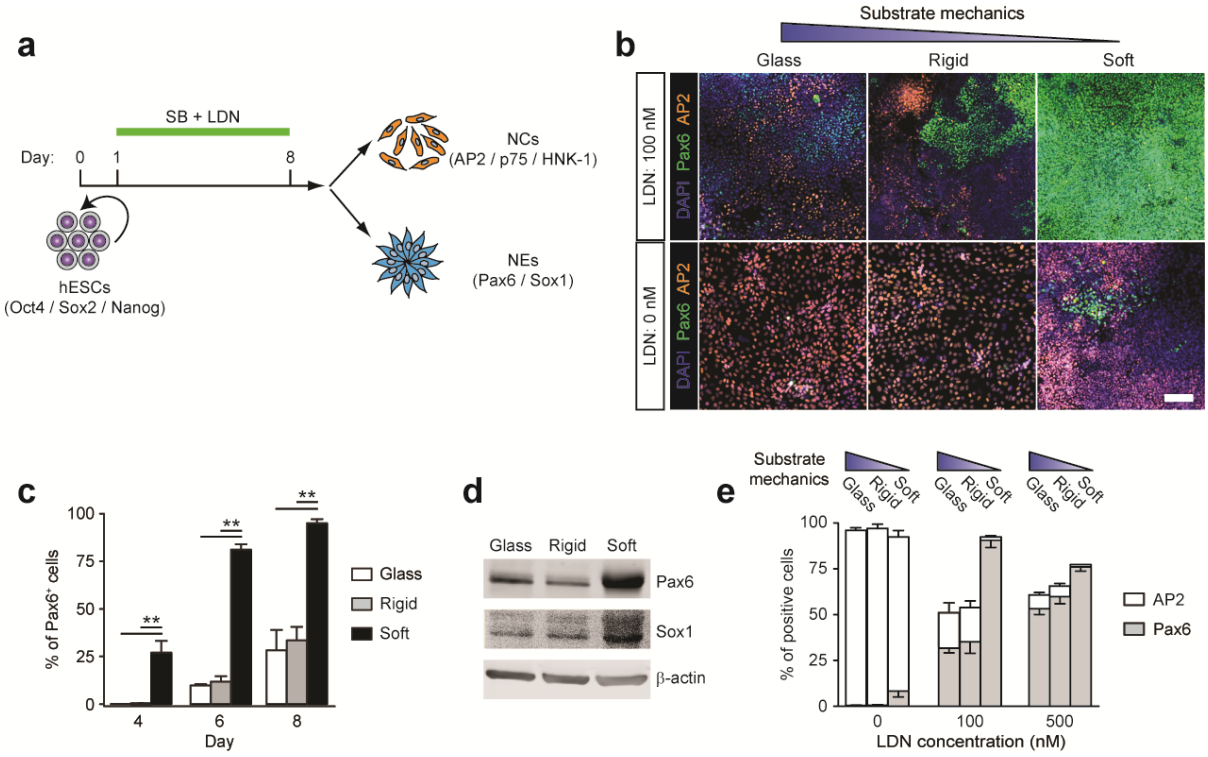

Figure 3-2 Soft substrates promote neuroepithelial conversion while inhibiting neural crest differentiation of hESCs in a BMP4-dependent manner. (**a**) Schematic diagram showing experimental design of hESC neural induction. hESCs were cultured for 8 d in neural induction media containing the dual Smad inhibitors, SB 431542 (SB, 10 µM) and LDN 193189 (LDN, 100 nM). (**b**) Representative immunofluorescence images showing $Pax6^+$ NEs and $AP2^+$ NCs derived from hESCs after 8 d of culture with (*top*; 100 nM) or without (*bottom*) LDN on vitronectin-coated coverslips and rigid (E = 1,200 kPa) and soft (E = 5 kPa) PMAs. Scale bar, 100 µm. (**c**) Bar graph showing percentage of $Pax6^+$ NEs on coverslips and rigid and soft PMAs at day 4, 6, and 8. (**d**) Western blotting showing Pax6 and Sox1 expression levels in hESCs cultured for 8 d on coverslips and rigid and soft PMAs. (**e**) Bar plot showing percentages of $Pax6^+$ NEs and $AP2^+$ NCs at day 8 as a function of substrate rigidity and LDN concentration. Data represents the mean ± s.e.m with n = 3. P-values were calculated using one-way *ANOVA*, followed by Tukey post hoc analysis. *, $P < 0.05$; **, $P < 0.01$.

monomer ratio, flat featureless PDMS surfaces with different bulk modulus *E* were generated and assayed for neural induction. Soft flat PDMS surfaces ($E \leq 5$ kPa) could significantly promote neural induction, compared to rigid flat PDMS surfaces ($E = 2.5$ MPa) or coverslips (Figure 3-7). Noticeably, neural induction by soft flat PDMS surfaces was not as drastic as soft PMAs, likely owing to their viscoelastic nature, different from the elastic PMAs. Temporal mRNA expression of pluripotency markers (*NANOG* and *SOX2*) and neuroectodermal markers (*PAX6*, *SOX1*, and *TUJ-1*) was quantified using qRT-PCR. Soft PMAs accelerated disruption of the transcriptional circuitry maintaining pluripotency, while promoting neuroectodermal gene expression (Figure 3-8). Experiments with another hESC line (CHB-10) and a hiPSC line derived from human foreskin fibroblasts showed that at day 6, $Pax6^+$ NEs constituted 60.8% ± 1.1% (CHB-10) and 78.8% ± 5.8% (hiPSCs) of cells on soft PMAs, respectively, in contrast to 23.2% ± 3.0% (CHB-10) and 24.5% ± 1.8% (hiPSCs) on rigid PMAs (Figure 3-9).

Treatment of hESCs with both Smad inhibitors led to $Pax6^+$ NEs, as well as $Pax6^-$ cells co-expressing neural crest (NC) markers AP2, p75, and HNK-1 (Figure 3-10)[74]. At day 8, 18.7% ± 5.3% and 18.1% ± 3.6% of cells were $AP2^+$ on coverslips and rigid PMAs, respectively. Strikingly, only 1.1% ± 0.5% of cells were $AP2^+$ on soft PMAs. Similar reductions in $p75^+$ and $HNK\text{-}1^+$ NCs were observed on soft PMAs. Paralleling the effects of substrate rigidity, manipulation of the concentration of the BMP4 inhibitor, LDN, altered the ratio of $Pax6^+$ NEs to $Pax6^-$ / $AP2^+$ NCs. Increasing LDN levels promoted differentiation toward $Pax6^+$ NEs, whereas LDN's absence favored NC differentiation.

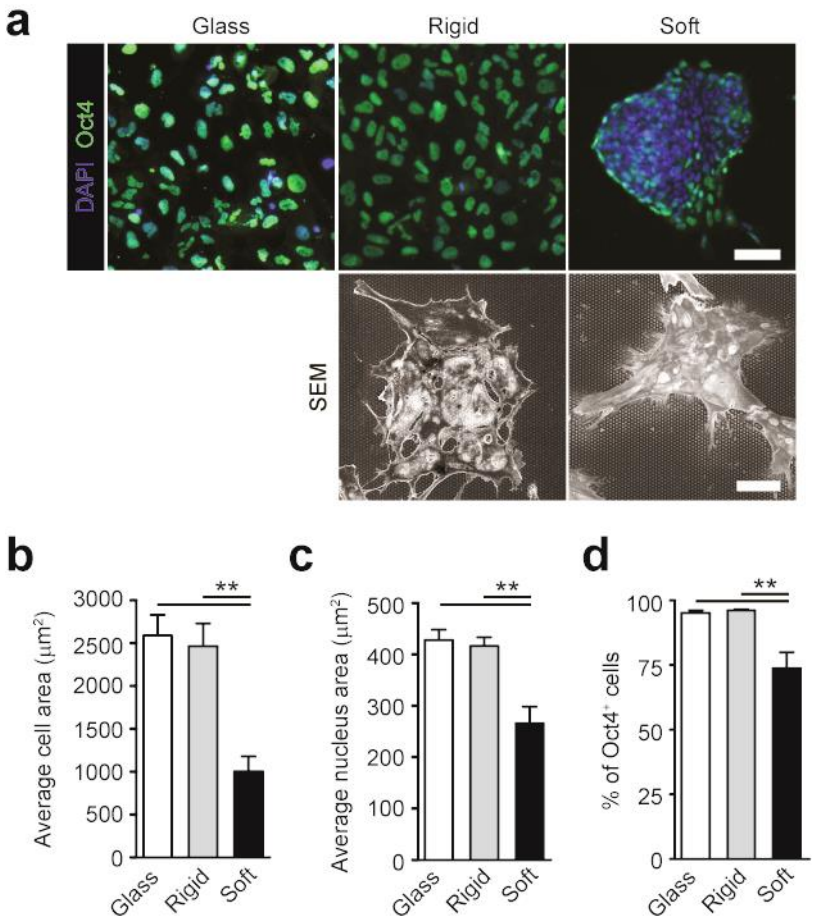

Figure 3-3 Rigidity-dependent cell morphology and self-renewal of hESCs. (**a**) Representative immunofluorescence (*top*) and SEM (*bottom*) images showing morphology and Oct4 expression of hESCs cultured in growth media for 1 d on coverslips and rigid (E = 1,200 kPa) and soft (E = 5 kPa) PMAs. (**b-d**) Quantification of cell spread area (**b**), nucleus area (**c**), and percentage of Oct4$^+$ cells (**d**) for hESCs after 1 d of culture in growth media on coverslips and rigid and soft PMAs. Data represents the mean ± s.e.m with n = 3. *P*-values were calculated using one way *ANOVA* followed by Tukey post hoc analysis. **, $P < 0.01$.

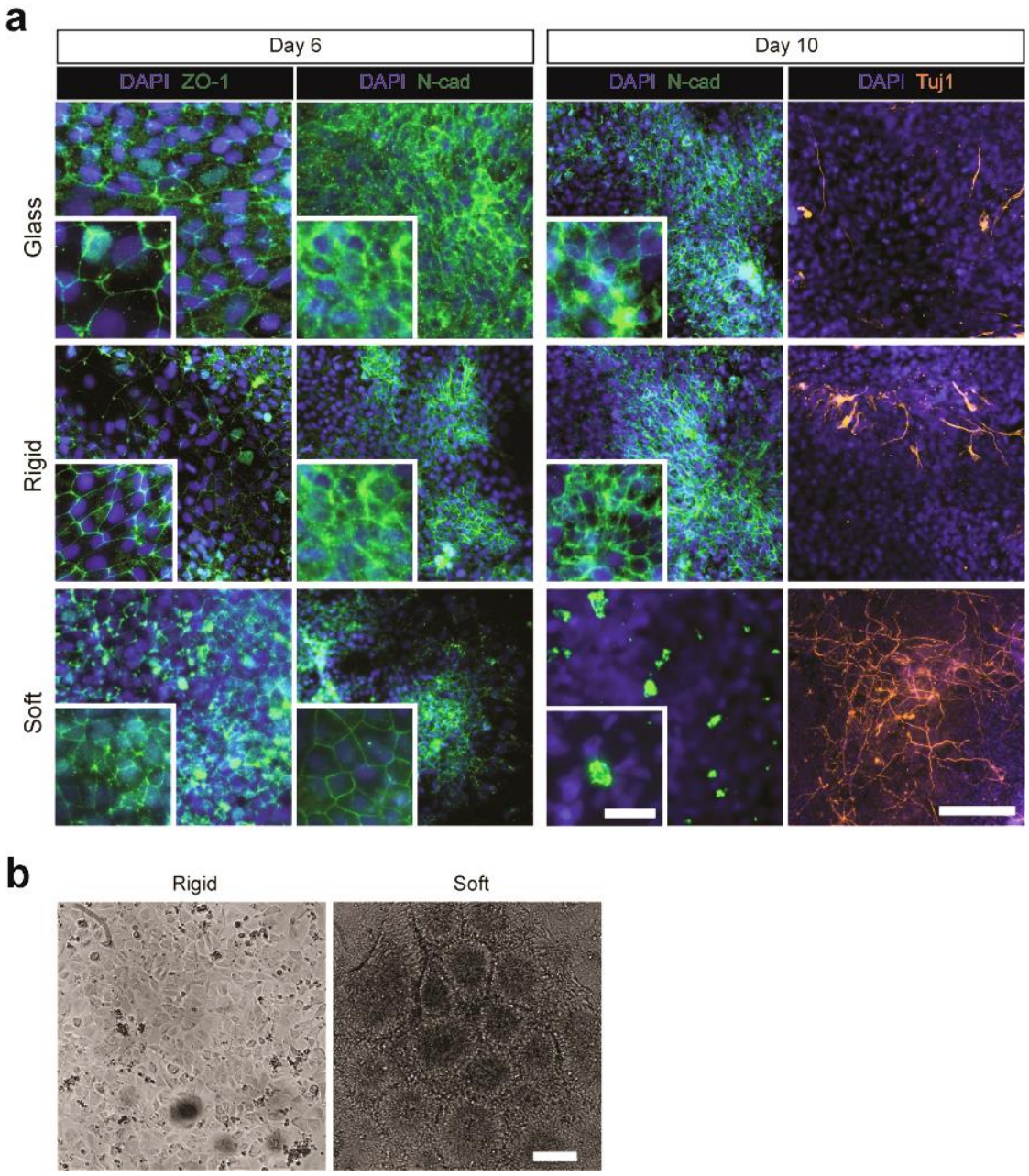

Figure 3-4 Neuroepithelial cells (NEs) derived from hESCs on soft PMAs could more readily form polarized neural tube-like rosettes than those from coverslips or rigid PMAs. hESCs were cultured on coverslips and rigid (E = 1,200 kPa) and soft (E = 5 kPa) PMAs in neural induction media for the first 6 d before switched to modified neural induction media supplemented with 20 ng mL^{-1} bFGF for an additional 4 d. At day 8, putative pre-rosette NEs were passaged onto coverslips and examined for capability to form neural tube-like rosettes. (**a**) Immunofluorescence for tight junction protein ZO-1, N-cadherin (N-cad), and β-III tubulin (or Tuj1, a neuronal form of tubulin) in NEs derived on coverslips (*top*) and rigid (*middle*) and soft (*bottom*) PMAs at day 6 (*left*) and day 10 (*right*). After bFGF treatment, NEs derived on soft but not rigid PMAs or coverslips became polarized as indicated by N-cad staining. In addition, fewer $Tuj1^+$ neurons were derived from hESCs on coverslips or rigid PMAs than from soft PMAs. Scale bars, 100 μm and 20 μm (insert). (**b**) Representative phase contrast images showing morphology of NEs on coverslips at days 9-10. Scale bar, 100 μm.

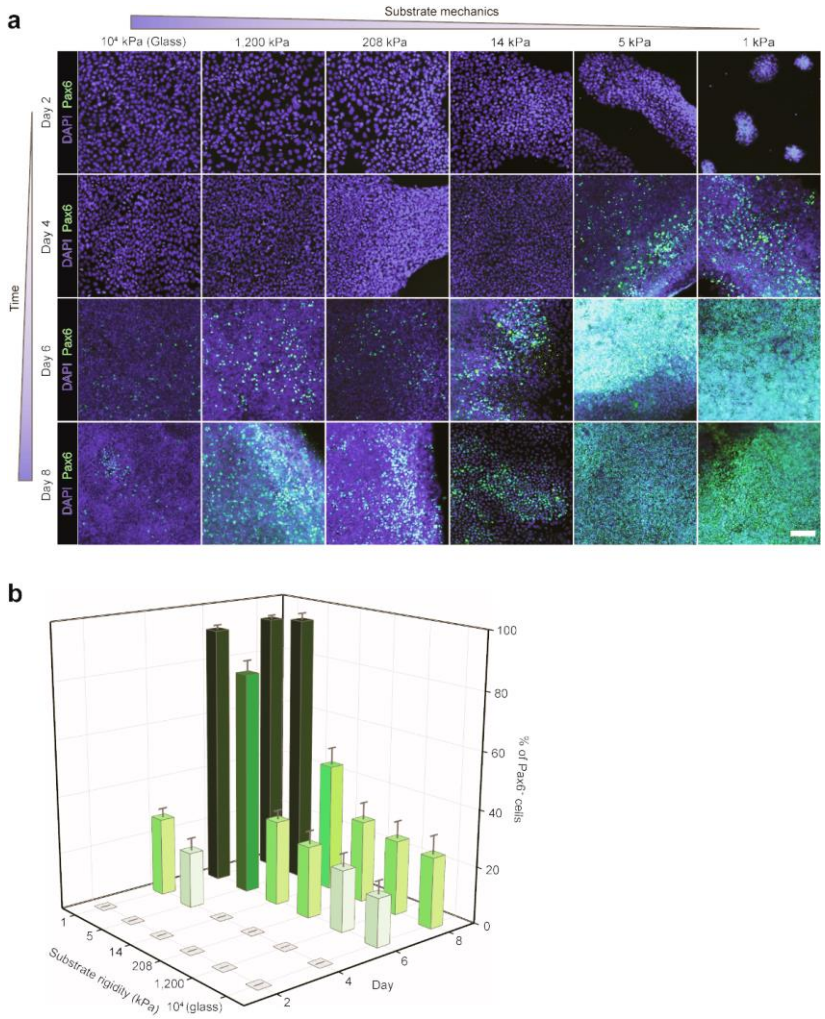

Figure 3-5 Screening assays of hESC neuroepithelial induction using coverslips (E = 10^4 kPa) and PMAs covering a broad range of rigidities (E = 1 - 1,200 kPa). (**a**) Representative immunofluorescence images showing Pax6$^+$ NE cells derived from hESCs cultured in neural induction media for 2, 4, 6 and 8 d on coverslips and PMAs of different rigidities. Scale bar, 100 μm. (**b**) Bar plot showing percentage of Pax6$^+$ NEs derived from hESCs as a function of both substrate rigidity and differentiation period. Data represents the mean ± s.e.m with n = 3.

a

PMA set #1 D = 1.8 μm, S = 4 μm		PMA set #2 D = 0.8 μm, S = 2 μm	
Post height L (μm)	Effective modulus E (kPa)	Post height L (μm)	Effective modulus E (kPa)
0.97	1,200	0.42	1,200
10.3	3.0	4.49	3.0
12.9	1.0	6.23	1.0

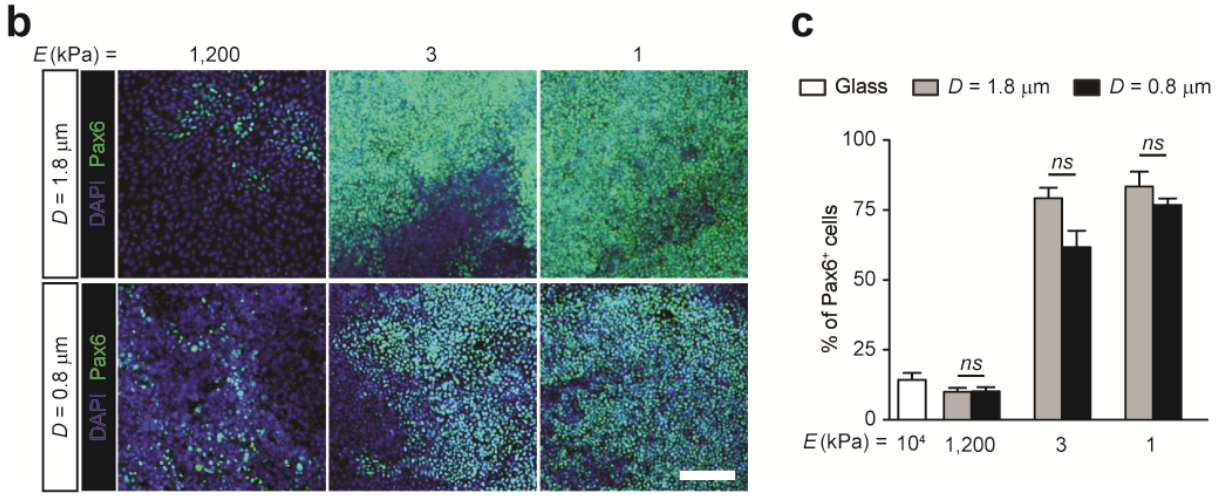

Figure 3-6 Rigidity-dependent hESC neuroepithelial induction is not sensitive to PDMS micropost geometries. (**a**) Table summarizing two sets of PMAs with different post diameters D and post center-to-center distacnes S. Three PMAs with varying post heights L but matching effective modulus E were selected from each PMA set. (**b**) Representative immunofluorescence images showing $Pax6^+$ NE cells derived from hESCs cultured in neural induction media for 6 d on the PMAs as indiciated. Scale bar, 100 μm. (**c**) Bar plot showing percentage of $Pax6^+$ NEs derived from hESCs as a function of substrate rigidity. Percentage of $Pax6^+$ cells are 14.3% ± 2.5% (glass), 9.8% ± 1.5% (D =1.8 μm, E = 1200 kPa), 10.1% ± 1.5% (D =0.8 μm, E = 1200 kPa), 79.1% ± 3.8% (D =1.8 μm, E = 3 kPa), 61.7% ± 5.8% (D =0.8 μm, E = 3 kPa), 83.6% ± 5.3% (D =1.8 μm, E = 1 kPa), and 76.7% ± 2.4% (D =0.8 μm, E = 1 kPa), respectively. For comparision, data from coverslip was included. Data represents the mean ± s.e.m with n = 3. P-values were calculated using one way *ANOVA* followed by Tukey post hoc analysis. *ns*, statistically not significant and $P > 0.05$.

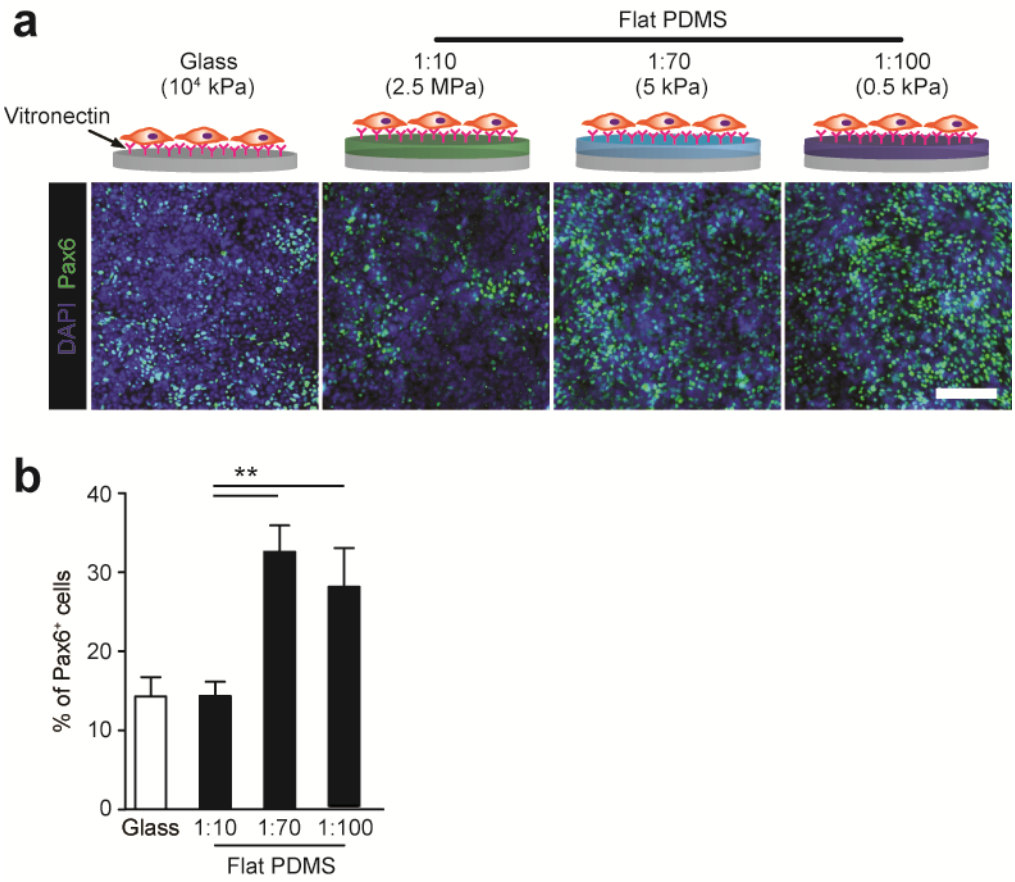

Figure 3-7 hESC neuroepithelial induction is sensitive to bulk modulus changes of flat PDMS substrates. Flat PDMS substrates were prepared with different curing agent to base monomer ratios (*w* / *w*) and thus had different bulk modulus *E*. (**a**) Representative immunofluorescence images showing Pax6$^+$ NE cells derived from hESCs cultured in neural induction media for 6 d on coverslip and 1:10 (*E* = 2.5 MPa), 1:70 (*E* = 5 kPa), and 1:100 (*E* = 0.5 kPa) flat PDMS substrates. Scale bar, 100 µm. (**b**) Percentage of Pax6$^+$ NEs derived from hESCs as a function of different substrates. Percentage of Pax6+ cells are 14.3% ± 2.5% (glass), 14.3% ± 1.8% (1:10 flat PDMS), 32.5% ± 3.3% (1:70 flat PDMS), and 27.7% ± 4.9% (1:100 flat PDMS), respectively. Data represents the mean ± s.e.m with *n* = 3. *P*-values were calculated using one way *ANOVA* followed by Tukey post hoc analysis. **, $P < 0.01$.

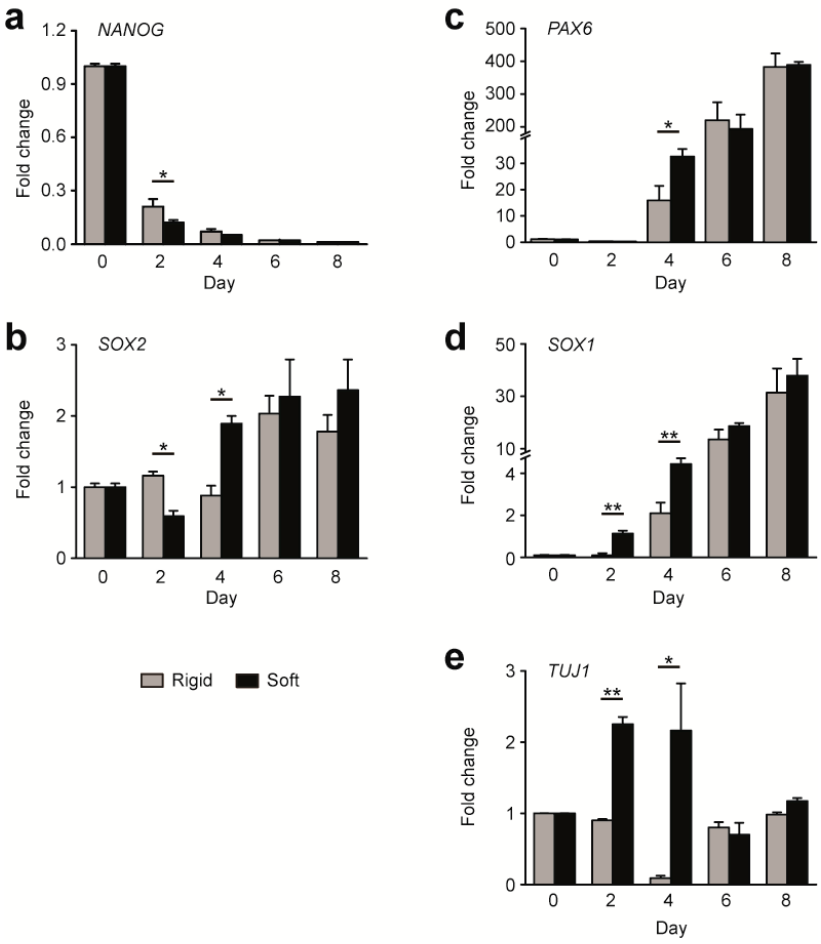

Figure 3-8 qRT-PCR analysis for temporal expression of pluripotency (*NANOG* and *SOX2*; **a&b**) and neuroectodermal (*PAX6*, *SOX1*, and *TUJ1*; **c-e**) markers during neural induction of hESCs. hESCs were cultured in neural induction media on rigid (E = 1,200 kPa) and soft (E = 5 kPa) PMAs. *NANOG*, a gene associated with pluripotency, decreased more significantly at day 2 on soft PMAs as compared to rigid PMAs. Expression level of *SOX2*, another pluripotency marker, was reduced only on soft PMAs at day 2 before recovering to a level greater than that of undifferentiated hESCs at day 4, consistent with a high *SOX2* expression level in neural progenitor cells. Genes associated with neural lineages, including *PAX6*, *SOX1* and *TUJ1* (also known as β-III tubulin, a neuronal form of tubulin), showed greater levels of expression on soft PMAs at day 2-4 when compared to rigid PMAs. The earliest neural markers expressed were *SOX1* and *TUJ1*, preceding induction of *PAX6*, being consistent with previous studies using dual Smad inhibitors. Expression level of each gene was normalized to data from undifferentiated hESCs, except for *SOX1*, which was normalized to data from hESCs cultured on soft PMAs at day 2. *SOX1* amplification in undifferentiated hESCs or hESCs cultured on rigid PMAs at day 2 was undetectable when arbitrary *Ct* values in qRT-PCR were set at 40. Data represents the mean ± s.e.m with at least three biological replicates and three technical replicates. *P*-values were calculated using two-side unpaired student *t*-tests. *, $P < 0.05$; **, $P < 0.01$.

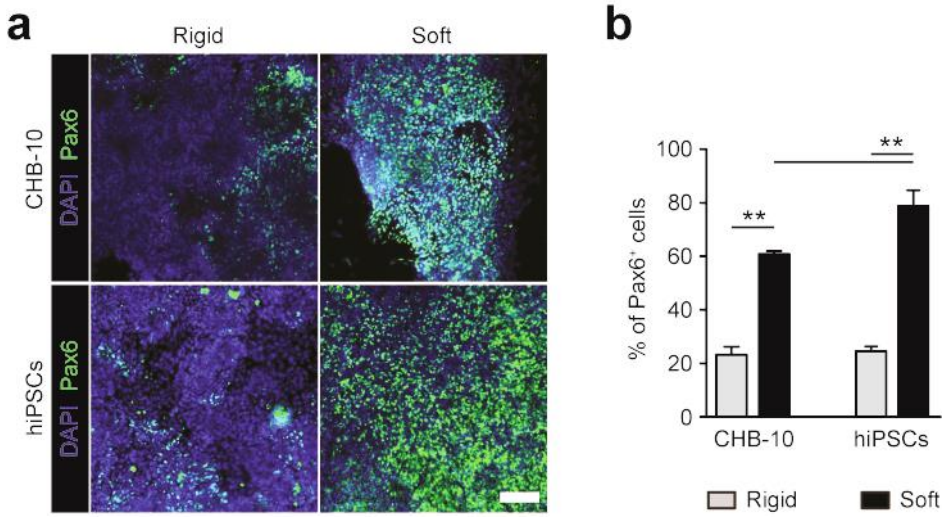

Figure 3-9 Soft substrates promoted neuroepithelial induction of both hESCs and hiPSCs. Representative immunofluorescence images (**a**) and bar plot (**b**) showing percentages of $Pax6^+$ NEs derived from CHB-10 hESCs (*top*) and hiPSCs (*bottom*) after 6 d of culture in neural induction media on both rigid (E = 1,200 kPa) and soft (E = 5 kPa) PMAs. Scale bar in **a**, 100 µm. Data represent the mean ± s.e.m with $n \geq 3$. P-values were calculated using two-side unpaired student t-tests. **, $P < 0.01$.

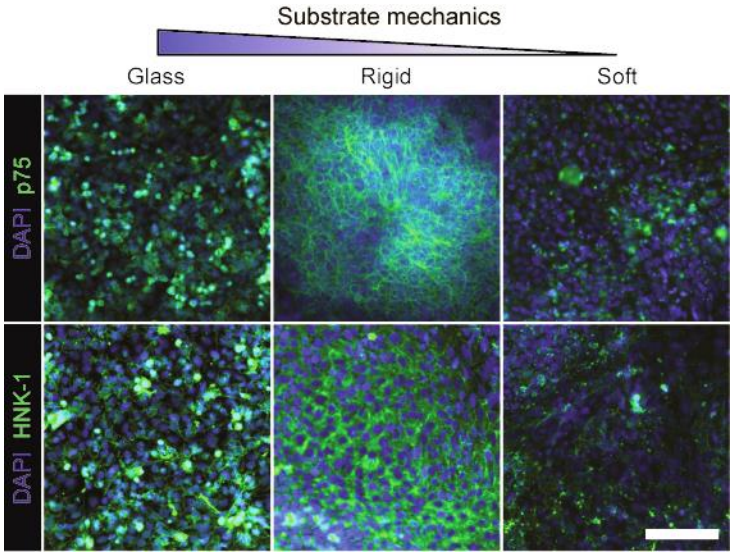

Figure 3-10 Soft substrates inhibited neural crest specification of hESCs. hESCs were cultured on coverslips and rigid (E = 1,200 kPa) and soft (E = 5 kPa) PMAs in neural induction media for 8 d before fixed and stained for NC markers p75 (*top*) and HNK-1 (*bottom*). Scale bar, 100 µm.

To induce functional neurons, NEs require anterior/posterior and dorsal/ventral patterning cues [78, 79]. When the caudalization factor, RA, was added to neural induction media from day 4, the posterior genes, *HOXB1*, *HOXB4*, and *HOXC8* were significantly upregulated, whereas *OTX2*, an anterior identity gene, was suppressed (Figure 3-11a,b). Surprisingly, soft PMAs promoted *HOXB1*, *HOXB4* and *HOXC8* expression in the absence of RA (Figure 3-11b). Although RA's effects exceeded those of soft PMAs on neural caudalization, expression of *HOXB4* and *HOXC8* remained responsive to varying substrate rigidities in the presence of RA, suggesting an additive effect of substrate rigidity on neural caudalization. Otx2 and HoxB4 protein expression levels confirmed the effect of soft PMAs on promoting neural patterning and specification of posterior identity (Figure 3-11c,d).

We next examined whether the ventralization factor, Purmorphamine (Pur), could induce MNs from caudalized NEs derived from soft PMAs, by using oligodendrocyte transcription factor 2 (Olig2) as a MN marker. When NEs were cultured continuously for an additional 8 d in the presence of Pur and RA, 65% ± 6.3% of cells on soft PMAs became $Olig2^+$, whereas only 7.9% ± 1.3% of cells were $Olig2^+$ on rigid PMAs (Figure 3-12). In the absence of RA, 19.3% ± 1.7% of cells on soft PMAs became $Olig2^+$, whereas on rigid PMAs only 3.5% ± 1.6% of cells were $Olig2^+$.

Because soft PMAs accelerate neural induction and caudalization, we investigated whether functional MN production could be expedited using soft PMAs. hESCs were cultured on vitronectin-coated coverslips and PMAs for 16 d to allow neural induction and caudalization prior to passage on poly-l-ornithine/laminin/fibronectin-coated coverslips and treatment with MN maturation media containing neurotrophic factors BDNF and IGF-1 for an additional 14 d (Figure 3-13a). Significantly more soft PMA-derived cells expressed the general neuron marker,

Tuj1, and the MN-associated transcription factors, Isl1 and HB9, at day 23 and the choline acetyltransferase (ChAT, an enzyme catalyzing the formation of neurotransmitter acetylcholine), at day 30, compared to cells from controls (Figure 3-13b,c). Notably, more $Tuj1^+$ cells derived from soft PMAs co-expressed Isl1 compared to those from controls. The purity of MNs, defined as the percentage of $HB9^+$ cells, from soft PMAs was improved about four-fold, compared to controls (Figure 3-13c). Furthermore, subculture of MN progenitors derived from soft PMAs led to about seven-, eleven-, and twelve-fold increases in the numbers (and thus yields) of $Tuj1^+$, $Isl1^+$, and $HB9^+$ cells, respectively (Figure 3-13d).

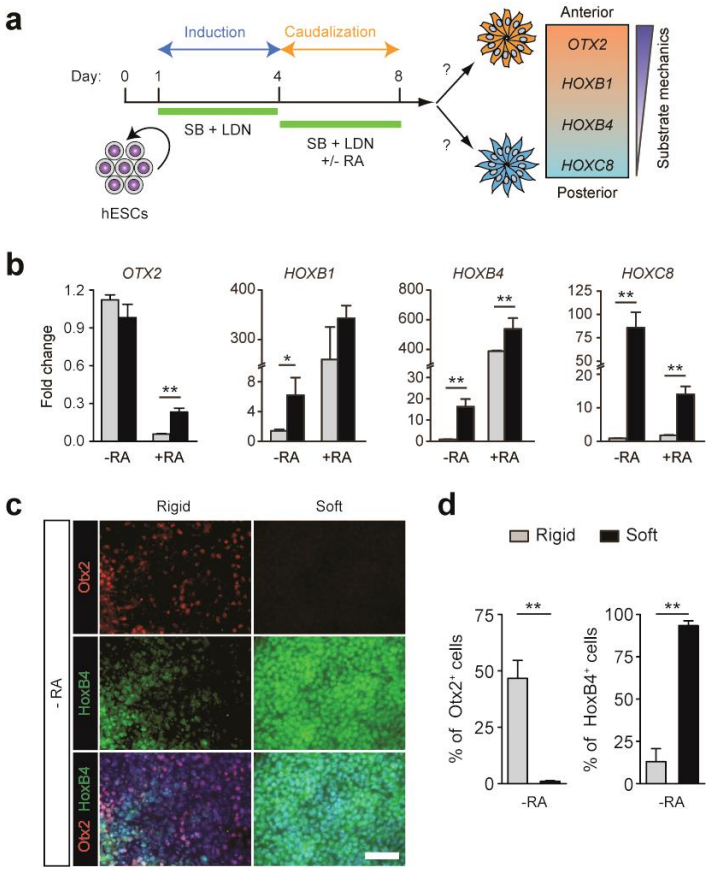

Figure 3-11 Soft substrates promoted caudalization of neuroepithelial cells (NEs). (**a**) Schematic diagram showing experimental design of caudalization of hESC-derived NEs. hESCs were cultured on rigid (E = 1,200 kPa) and soft (E = 5 kPa) PMAs in neural induction media containing the dual Smad inhibitors SB and LDN for 8 d. Culture media were supplemented with or without the caudalization factor, retinoic acid (RA), from day 4. (**b**) qRT-PCR analysis of expression levels of anterior (*OTX2*) and posterior (*HOXB1*, *HOXB4*, and *HOXC8*) markers for hESCs at day 8 as a function of both micropost rigidity and RA supplementation. Otx2 is a homeodomain protein expressed by fore- and midbrain cells, while HoxB1, HoxB4, and HoxC8 are motor neuron-specific transcription factors. Data were normalized to *GAPDH*. (**c&d**) Representative immunofluorescence images (**c**) and bar plots (**d**) showing percentages of $Otx2^+$ and $HoxB4^+$ neurons derived from hESCs at day 8 without RA supplementation. Data represent the mean ± s.e.m with $n \geq 3$. P-values were calculated using two-side unpaired student t-tests. *, $P < 0.05$; **, $P < 0.01$.

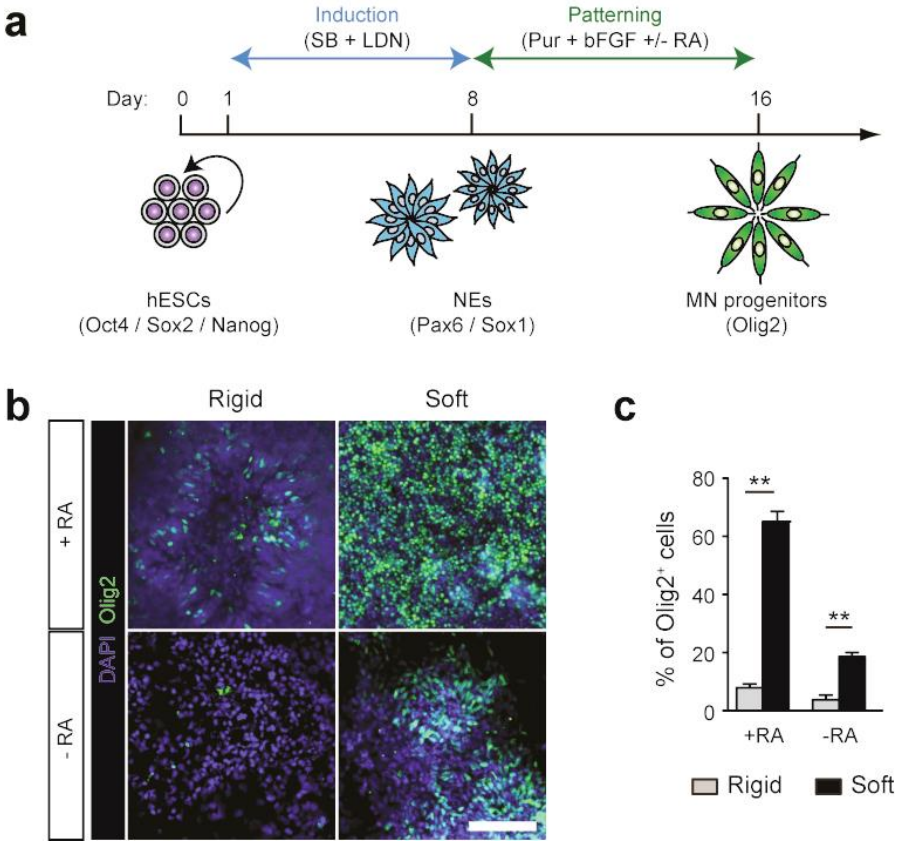

Figure 3-12 Soft substrates promoted motor neuron (MN) specification of hESC-derived neuroepithelial cells (NEs). (**a**) Schematic diagram showing experimental design of neural induction, caudalization, and patterning of hESCs. hESCs were cultured on rigid (E = 1,200 kPa) and soft (E = 5 kPa) PMAs in neural induction media containing the dual Smad inhibitors SB and LDN for 8 d, before switched to MN differentiation media containing purmorphamine (Pur), basic fibroblast growth factor (bFGF), and retinoic acid (RA) for another 8 d. RA was removed from MN differentiation media in some assays as indicated in **b&c**. (**b&c**) Representative immunofluorescence images (**b**) and bar plots (**c**) showing percentages of Olig2$^+$ MN progenitor cells derived from hESCs at day 16 as a function of both micropost rigidity and RA supplementation. Olig2 is a transcription factor expressed by MN progenitors at the pMN domain of the ventral neural tube. Scale bar in **b**, 100 μm. Data represent the mean ± s.e.m with $n \geq 3$. P-values were calculated using two-side unpaired student t-tests. **: $P < 0.01$.

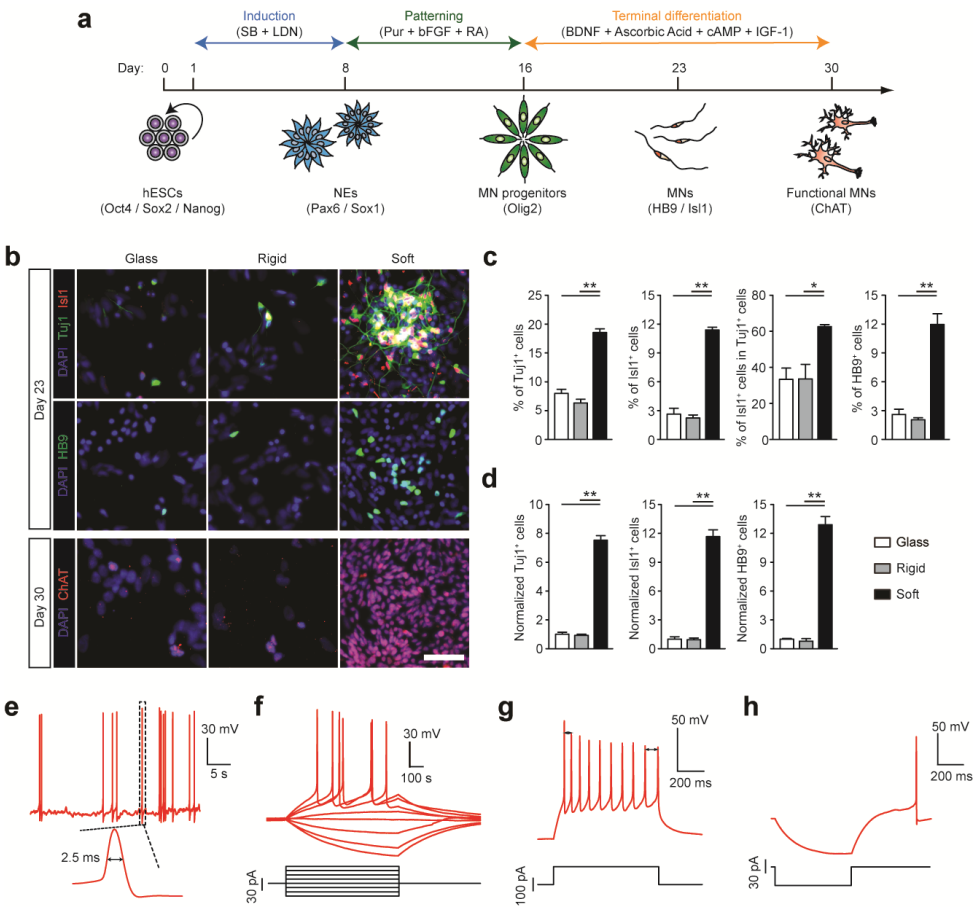

Figure 3-13 Purity and yield of functional motor neurons (MNs) derived from hESCs are improved on soft substrates. (**a**) Schematic diagram showing experimental design for sequential neural induction, patterning, and functional maturation of MNs from hESCs. hESCs were cultured on vitronectin-coated coverslips and rigid (E = 1,200 kPa) and soft (E = 5 kPa) PMAs in neural induction media containing the dual Smad inhibitors SB and LDN for 8 d and then in MN differentiation media containing purmorphamine (Pur), basic fibroblast growth factor (bFGF), and retinoic acid (RA) for an additional 8 d. Putative MN progenitor cells collected at day 16 were transferred onto coverslips and cultured in MN maturation media containing brain-derived neurotrophic factor (BDNF), ascorbic acid, cyclic adenosine monophosphate (cAMP), and insulin-like growth factor 1 (IGF-1) for another 14 d. (**b**) Representative immunofluorescence images showing Tuj1$^+$, Isl1$^+$, and HB9$^+$ cells at day 23, and ChAT$^+$ cells at day 30. Scale bar, 100 µm. (**c&d**) Bar plots showing percentages (**c**) and relative numbers (**d**) of Tuj1$^+$, Isl1$^+$, and HB9$^+$ cells at day 23 as a function of substrate rigidity. Data in **d** was normalized to values from coverslips. Data represents the mean ± s.e.m with $n \geq 3$. P-values were calculated using two-side unpaired student t-tests. *: $P < 0.05$; **: $P < 0.01$. (**e-h**) Electrophysiological characterization of functional MNs derived from soft PMAs at day 30 using whole-cell patch clamp. **e**: spontaneous action potential (AP) with resting membrane potential of -64.5 mV; **f**: voltage response to current step injection; **g**: instantaneous frequency change or spike frequency adaptation (SFA) evoked with positive current injection; **h**: post-inhibitory rebound (PIR) after hyperpolarizing current injection.hout DECMA-1 on both soft (E_{eff} = 1.92 kPa) and rigid (E_{eff} = 1,218.4 kPa) PDMS micropost arrays. Scale bar, 50 µm. (*C*) Bar plot of percentage of Oct$^+$ cells for DECMA-1 treated hESCs and untreated controls as a function of the PDMS micropost rigidity. Data represents the means ± s.e.m from 3 independent experiments. *: $p < 0.05$; **: $p < 0.01$.

Next, action potentials (APs) were evaluated using whole-cell recording. Among 27 cells recorded, 12 generated APs with an average amplitude > 65 mV and were considered functionally mature [80]. Another 5 cells fired APs with the average amplitude < 65 mV. Nine displayed spontaneous APs with an average amplitude of 85.3 mV and a half-height width of 2.5 ms (Figure 3-13e). When injected with depolarizing currents, 15 cells displayed firing activities with an average first spike amplitude of 71.7 mV (Figure 3-13f). MNs can decrease firing rates responding to constant stimuli, a phenomenon called spike frequency adaption (SFA) [81]. Here, 6 of 12 "mature" MNs displayed SFA with a depolarizing current (Figure 3-13g). Moreover, post-inhibitory rebound (PIR, depolarizations and/or spiking following a release from hyperpolarization) was observed in 6 MNs (Figure 3-13h). These data suggest that MNs derived from soft PMAs at day 30 display electrophysiological activities comparable to those from primary neurons *in vivo* [80]. In comparison, hPSCs require up to 50 days under conventional differentiating conditions for complete functional maturation into a MN[82, 83].

To examine whether rigidity-mediated MN production might depend on specific ventralizing and neurotrophic factors, additional 23-day (Figure 3-14) and 35-day (Figure 3-15) MN differentiation assays were conducted using SHH for patterning and ventralization and neurotrophic factors BDNF, GDNF, CNTF, and IGF-1 for terminal differentiation. The purity and yield of MNs derived from soft PMAs were consistently much greater than from controls.

Our data presented in Figure 3-2 suggested a connection between mechanotransduction and inhibition of BMP signaling in hPSCs. Indeed, immunoblots substantiated an inhibitory role of soft PMAs on Smad1/5/8 phosphorylation (Figure 3-16a). Phosphorylated Smads (phosphoSmads) require translocation to the nucleus for transcriptional activation [84]. YAP/TAZ, nuclear transducers in the canonical Hippo pathway, bind phosphoSmads and control

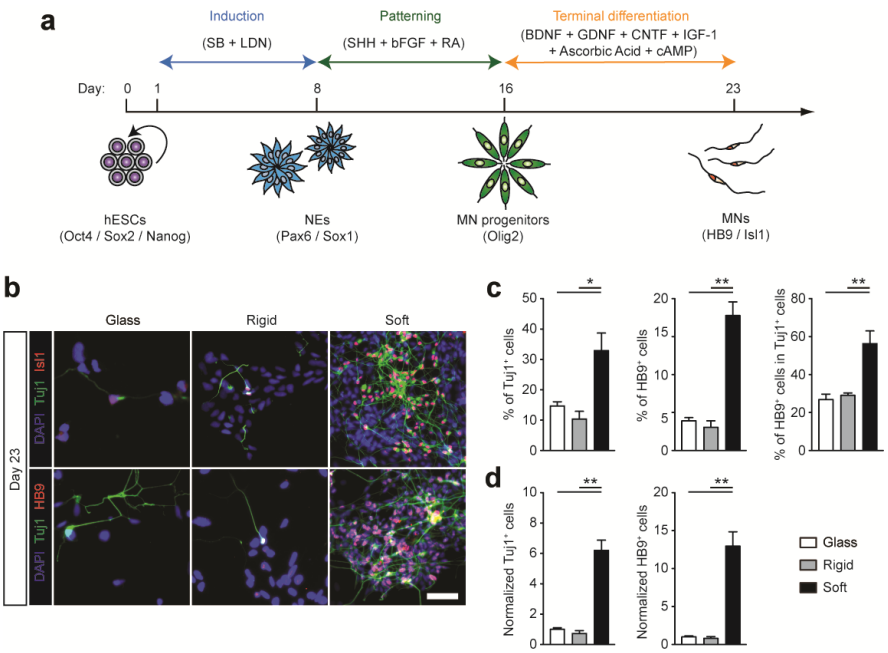

Figure 3-14 Purity and yield of motor neurons (MNs) derived from hESCs are improved on soft PMAs with a shortened 23-day differentiation protocol using modified MN differentiation and maturation media. (**a**) Schematic diagram showing experimental design for sequential neural induction, patterning, and terminal differentiation of MNs from hESCs. hESCs were cultured on coverslip and rigid (E = 1,200 kPa) and soft (E = 5 kPa) PMAs in neural induction media containing the dual Smad inhibitors SB and LDN for 8 d and then in the modified MN differentiation media containing SHH, bFGF, and RA for an additional 8 d. Putative MN progenitor cells collected at day 16 were transferred onto coverslips and cultured in the modified MN maturation media containing BDNF, GDNF, CNTF, IGF-1, ascorbic acid, and cAMP for another 7 d. (**b-d**) Representative immunofluorescence images (**b**) and bar plots (**c&d**) showing percentages (**c**) and relative numbers (**d**) of $Tuj1^+$ neurons and $HB9^+$ MNs derived from hESCs on day 23 as a function of substrate rigidity. The normalized number of Tuj1+ cells are 1 ± 0.09 (glass), 0.7 ± 0.19 (rigid PMAs), and 6.2 ± 0.67 (soft PMAs). The normalized number of HB9 cells are 1 ± 0.13 (glass), 0.80 ± 0.24 (rigid PMAs), and 12.9 ± 1.88 (soft PMAs). Scale bar in **b**, 100 μm. Data in **d** was normalized to values from coverslip. Data represents the mean ± s.e.m with $n \geq 3$. P-values were calculated using one way *ANOVA* followed by Tukey post hoc analysis. *: $P < 0.05$; **: $P < 0.01$.

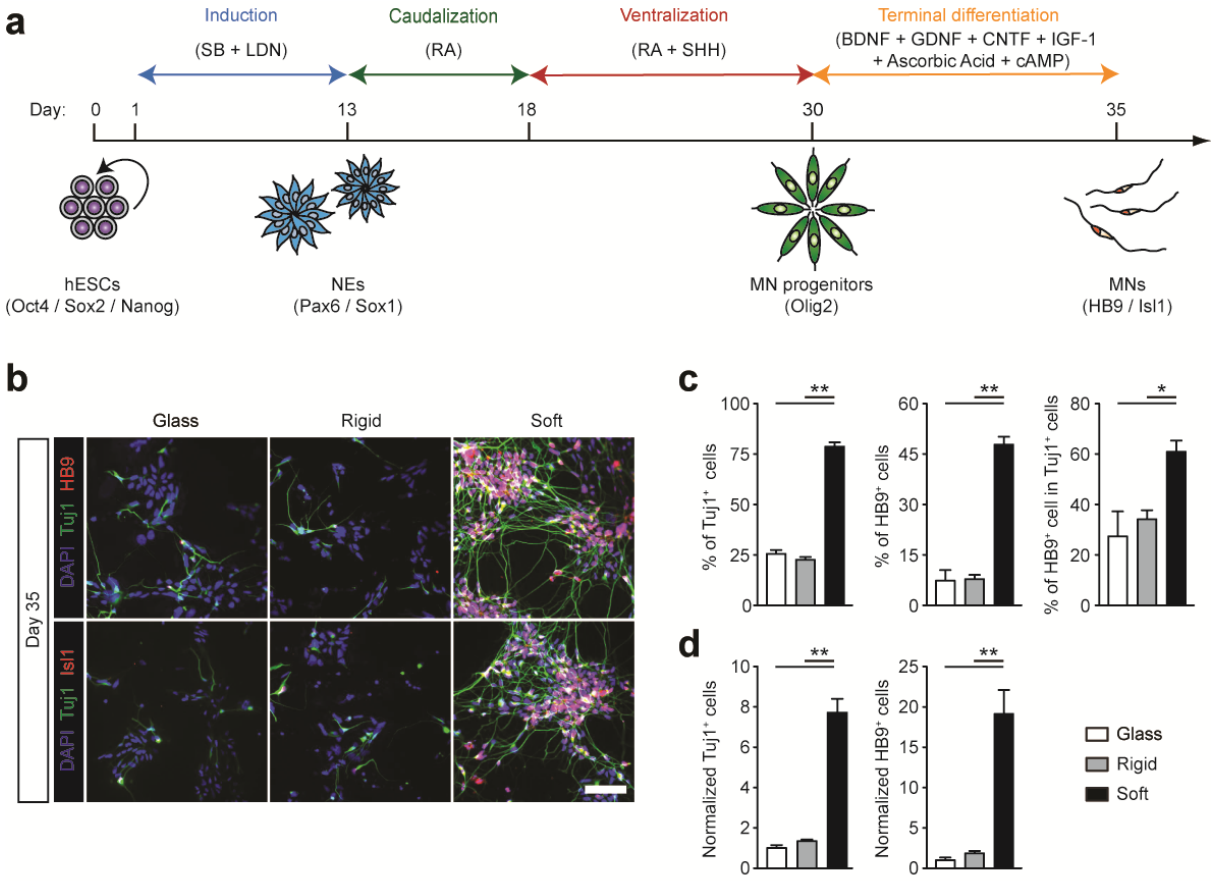

Figure 3-15 Purity and yield of motor neurons (MNs) derived from hESCs are improved on soft PMAs with a standard 35-day differentiation protocol. (**a**) Schematic diagram showing experimental design for sequential neural induction, caudalization, ventralization, and terminal differentiation of MNs from hESCs. hESCs were cultured on coverslip and rigid (E = 1,200 kPa) and soft (E = 5 kPa) PMAs in neural induction media containing the dual Smad inhibitors SB and LDN for 13 d and then in N2 media supplemented with RA for another 5 d. Cells collected at day 18 were transferred onto coverslips and cultured in N2 media supplemented with RA and SHH till day 30. Cells were then switched to the modified MN maturation media containing BDNF, GDNF, CNTF, IGF-1, ascorbic acid, and cAMP for another 5 d. (**b-d**) Representative immunofluorescence images (**b**) and bar plots (**c&d**) showing percentages (**c**) and relative numbers (**d**) of $Tuj1^+$ neurons and $HB9^+$ MNs derived from hESCs on day 35 as a function of substrate rigidity. The normalized number of Tuj1+ cells are 1 ± 0.14 (glass), 1.3 ± 0.08 (rigid PMAs), and 7.7 ± 0.69 (soft PMAs). The normalized number of HB9 cells are 1 ± 0.32 (glass), 1.86 ± 0.28 (rigid PMAs), and 19.1 ± 3.0 (soft PMAs). Scale bar in **b**, 100 µm. Data in **d** was normalized to values from coverslip. Data represents the mean ± s.e.m with $n \geq 3$. P-values were calculated using one way *ANOVA* followed by Tukey post hoc analysis. *: $P < 0.05$; **: $P < 0.01$.

their nucleocytoplasmic shuttling in hESCs [85]. In the Hippo pathway, Lats1/2 kinase phosphorylates YAP/TAZ, which in turn bind the scaffolding protein 14-3-3 to remain cytoplasmic [86]. YAP/TAZ-mediated nuclear accumulation of phosphoSmads is required for hESC pluripotency and its loss results in neuroectoderm differentiation [85]. A recent study also shows that YAP/TAZ are critical in mechanotransduction [87, 88].

Supporting our hypothesis that YAP/TAZ-mediated nuclear accumulation of Smads regulates rigidity-dependent neural induction of hESCs, nuclear YAP/TAZ were observed in 95% ± 2.7% and 38.2% ± 1.6% of hESCs on rigid and soft PMAs, respectively (Figure 3-16b,c). Rigidity-dependent subcellular localization of YAP/TAZ was maintained after 3 d of neural induction and coincided with nucleocytoplasmic shuttling of Smad 2/3 and Smad 1/5/8 (Figure 3-16d). Co-localization of YAP/TAZ and phosphoSmad 1/5/8 was also observed before and after neural induction (Figure 3-17).

We next examined whether substrate rigidity regulates YAP/TAZ in hESCs in a Hippo-dependent manner. Immunoblots showed that soft PMAs promoted YAP phosphorylation on serine 127 (ser^{127}), a key target of Lats1/2 kinase downstream of the Hippo pathway (Figure 3-16e). Silencing of *Lats1* expression using siRNA suppressed YAP phosphorylation on ser^{127} (Figure 3-18). Notably, *Lats1* knockdown hESCs displayed a spread morphology on both rigid and soft PMAs, indicating loss of mechanosensing properties (Figure 3-18). Soft PMAs did not promote neural induction of *Lats1* knockdown hESCs (Figure 3-16f,g), further supporting that Lats-mediated phosphorylation of YAP may relay mechanical signals exerted by substrate rigidity.

Adult mammalian cell studies suggest functional links between two major intracellular mechanotransductive components, Rho GTPase and the actomyosin cytoskeleton (CSK), and the

Hippo-YAP pathway [88-91]. Indeed, hESCs on rigid PMAs exhibited bundled actin microfilaments at cell peripheries, whereas actin microfilaments were diffuse and distributed throughout cells on soft PMAs (Figure 3-19). hESCs were treated independently with Y27632 (inhibitor of Rho-associated kinase, or ROCK, downstream effector of RhoA), which decreases actomyosin contractility while maintaining intact CSK structure; cytochalasin D (CytoD), an inhibitor of actin polymerization; or lysophosphatidic acid (LPA), which stimulates RhoA and facilitates formation of actin microfilaments. Compared to controls, Y27632 promoted cytoplasmic localization of YAP/TAZ and significantly increased the percentage of $Pax6^+$ NEs on rigid but not soft PMAs (Figure 3-20 and Figure 3-16h-j). In contrast, LPA facilitated nuclear localization of YAP/TAZ and inhibited neural induction on both rigid and soft PMAs. Notably, CytoD treatment had a negligible effect on YAP/TAZ translocation on soft PMAs; neural induction was significantly more efficient on soft PMAs without treatment, compared to that on rigid PMAs treated with Y27632 (Figure 3-16h-j). Our data are consistent with findings that ROCK inhibition facilitates neural differentiation of mouse ESCs and embryonal carcinoma stem cells [92, 93], while LPA maintains hESC pluripotency [94, 95].

By combining dual Smad inhibition with PMAs, we generated high-yield and -purity functional MNs from hPSCs. PMAs are fully defined substrates that can be mass-produced for large-scale hPSC culture. We demonstrate that like many human adult stem cells [32-34], hPSCs are intrinsically mechanosensitive and substrate rigidity is an *in vitro* extracellular switch that directs NE vs. NC lineage decisions and anterior vs. posterior patterning. In this work, our studies suggest a putative multi-targeted mechanotransductive process in hPSCs (Figyre 3-21) where soft PMAs inhibit Smad phosphorylation while activating Lats, an actin-binding protein [96], during disassembly of actin microfilaments. This in turn phosphorylates YAP to prevent

nuclear translocation of phosphoSmads and inhibit subsequent activation of Smad target genes. Collectively, our results suggest that mechanical properties of the extracellular matrix *in vivo* may act as a "mechanical organizer" synergizing with morphogens to direct neural plate specification and anterior-posterior axis formation during neurulation.

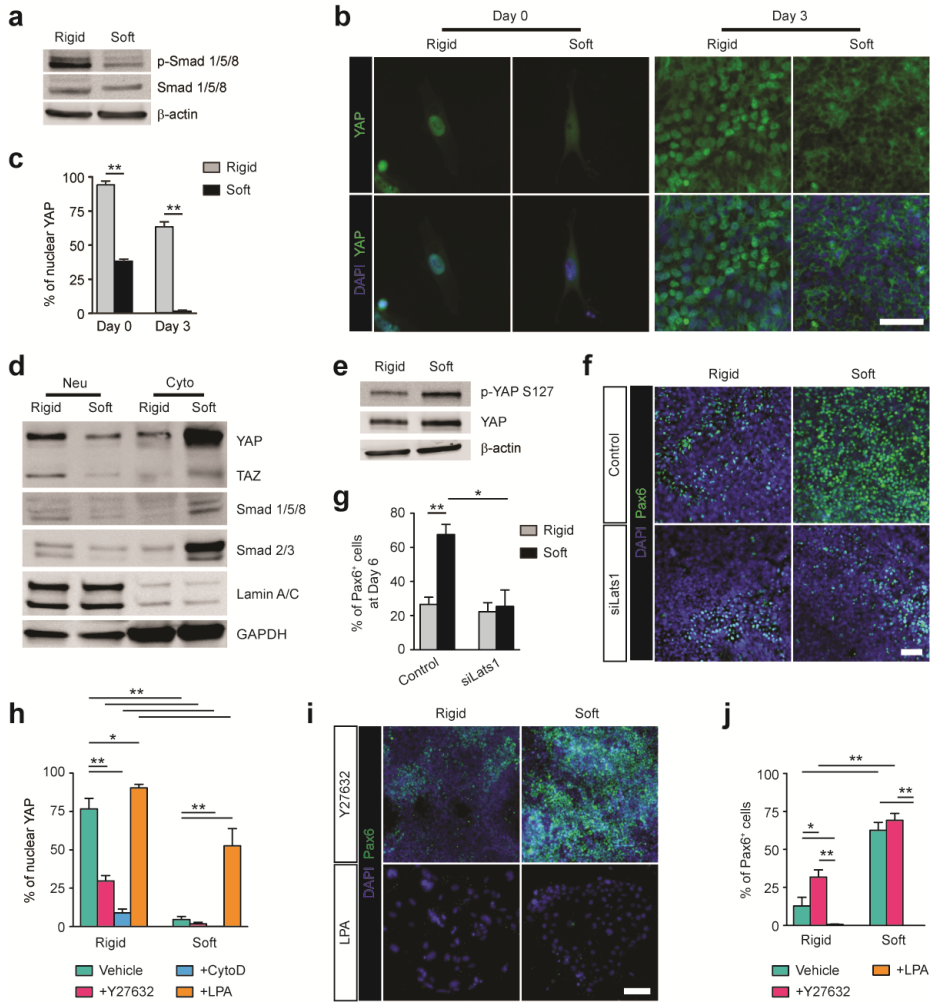

Figure 3-16 Soft substrates promote neuroepithelial conversion of hESCs through a multi-targeted mechanotransductive process involving mechanosensitive Smad phosphorylation and nucleocytoplasmic shuttling regulated by rigidity-dependent Hippo-YAP activities and the actomyosin cytoskeleton (CSK). (**a**) Western blotting of total and phosphorylated Smad 1/5/8 (p-Smad 1/5/8) in hESCs cultured in neural induction media for 3 d on rigid (E = 1,200 kPa) and soft (E = 5 kPa) PMAs. (**b&c**) Representative immunofluorescence images (**b**) and bar plot (**c**) showing rigidity-dependent sub-cellular localization of YAP in hESCs at day 0 and day 3. Scale bar in **b**, 50 μm. (**d**) Western blotting for YAP, TAZ, Smad 1/5/8 and Smad 2/3 in nuclear and cytoplasmic protein fractions from hESCs cultured for 3 d on rigid and soft PMAs. (**e**) Western blotting for phosphorylated YAP S127 (p-YAP S127) and YAP in whole cell lysates of hESCs after 3 d of culture on rigid and soft PMAs. (**f&g**) Representative immunofluorescence images (**f**) and bar plot (**g**) showing the percentage of $Pax6^+$ NEs derived from scramble control and *siLats1* knockdown hESCs after 6 d of culture on rigid and soft PMAs. Scale bar in **f**, 50 μm. (**h**) Bar graph showing the percentage of hESCs with nuclear localization of YAP after 3 d of culture with different drug supplementations, as indicated. (**i&j**) Representative immunofluorescence images (**i**) and bar plot (**j**) showing the percentage of $Pax6^+$ NEs derived from hESCs on rigid and soft PMAs after 6 d of culture with different drug supplementations, as indicated. Scale bar in **i**, 50 μm. β-actin and GAPDH were used as protein loading controls and lamin A/C for nuclear fraction control in Western blots. Data represents the mean ± s.e.m with $n \geq 3$. P-values in **c** & **g** and **h** & **j** were calculated using two-side unpaired student t-tests and one way *ANOVA* followed by Tukey post hoc analysis, respectively. *, $P < 0.05$; **, $P < 0.01$.

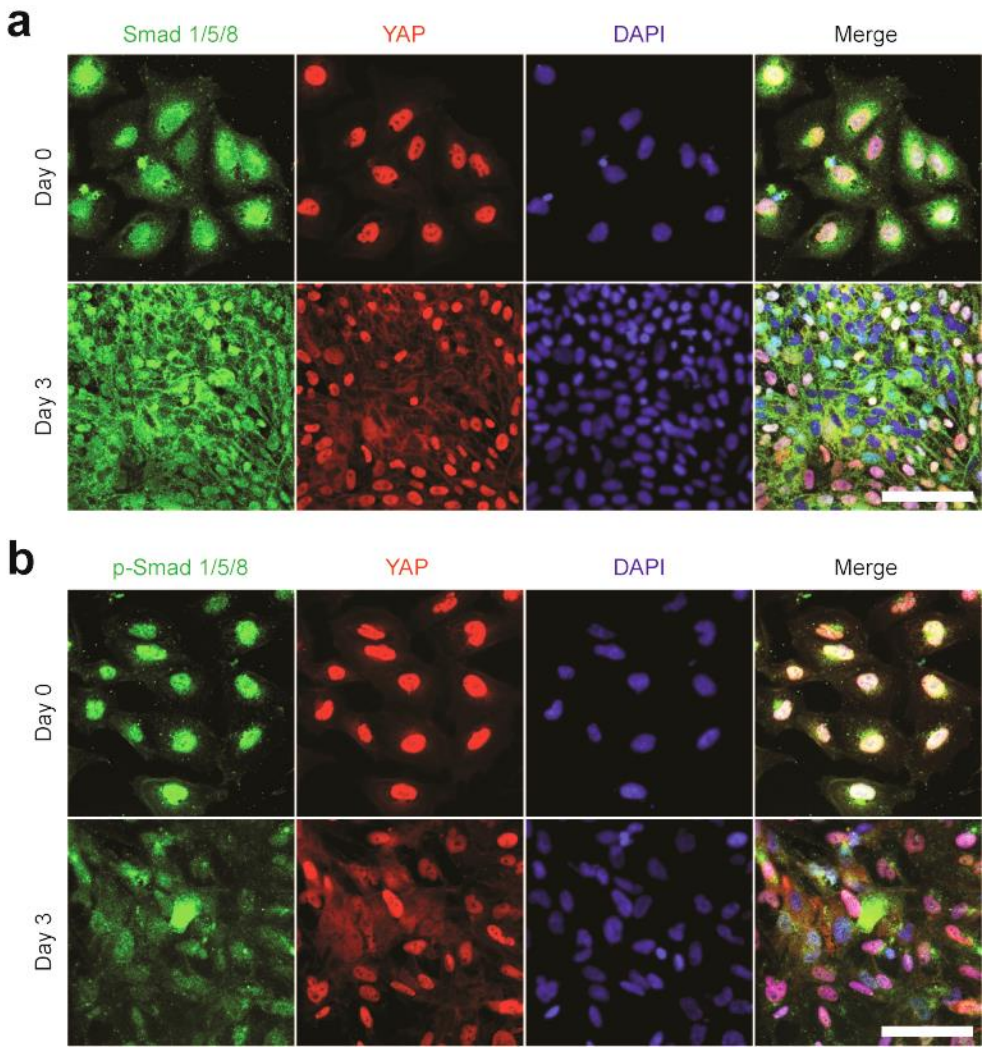

Figure 3-17 Co-localization of phosphorylated Smad 1/5/8 (p-Smad 1/5/8) and YAP in the cell nucleus of hESCs cultured on coverslips undergoing neuronal differentiation, indicating that YAP might be required for nuclear translocation of p-Smad 1/5/8. Immunofluorescence for Smad 1/5/8 (**a**) or p-Smad 1/5/8 (**b**) and YAP in hESCs. hESCs were fixed and immunostained 24 hr after cell seeding (day 0) or after 3 d of culture in neural induction media (day 3). Scale bars in **a&b**, 100 µm.

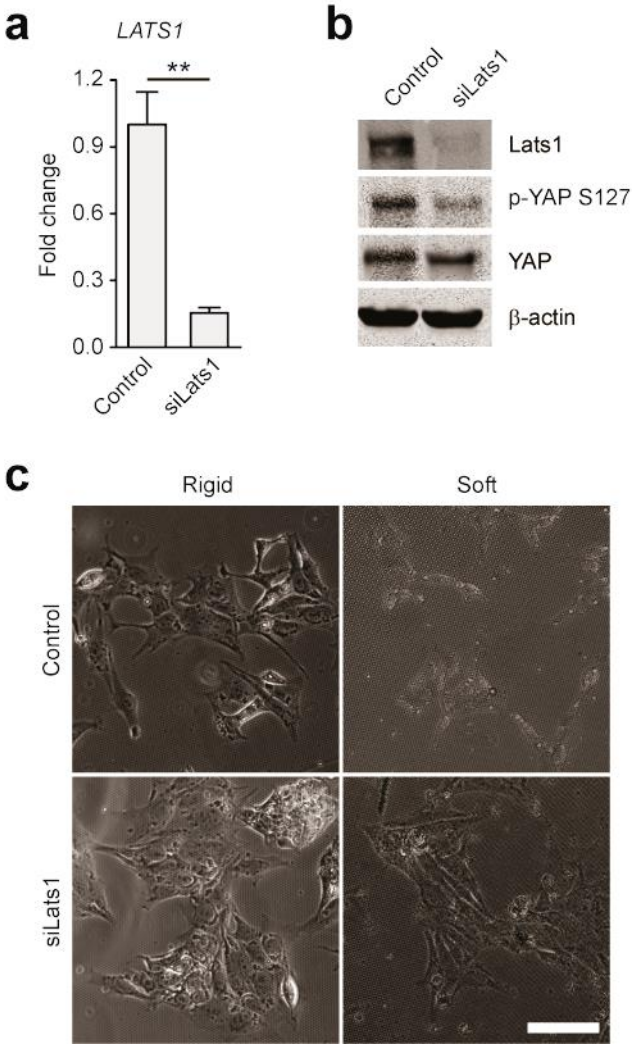

Figure 3-18 Characterization of siRNA-mediated knockdown of Lats1 in hESCs. (**a**) qRT-PCR analysis of *Lats1* expression in scrambled siRNA (control) and Lats1 knockdown (siLats1) hESCs 48 hr after siRNA transfection. Data represents the mean ± s.e.m with $n \geq 3$. *P*-value was calculated using two-side unpaired student *t*-test. **: $P < 0.01$. (**b**) Western blotting for Lats1, total YAP, and phorsphorylated YAP S127 (p-YAP S127) in scramble control and *siLats1* knockdown hESCs. (**c**) Representative phase contrast images of scramble control (*top*) and siLats1 knockdown (*bottom*) hESCs 24 hr after cell seeding in growth media on rigid (E = 1,200 kPa) and soft (E = 5 kPa) PMAs. Similar to non-transfected hESCs (not shown), scramble control hESCs were flat and spread out on rigid PMAs while appearing round and compact on soft PMAs. In distinct contrast, *Lats1* knockdown hESCs showed flat and well-spread morphology on both rigid and soft PMAs, suggesting loss of their mechanosensory properties. Scale bar, 100 µm.DECMA-1 on both soft (E_{eff} = 1.92 kPa) and rigid (E_{eff} = 1,218.4 kPa) PDMS micropost arrays. Scale bar, 50 µm. (*C*) Bar plot of percentage of Oct^+ cells for DECMA-1 treated hESCs and untreated controls as a function of the PDMS micropost rigidity. Data represents the means ± s.e.m from 3 independent experiments. *: $p < 0.05$; **: $p < 0.01$.

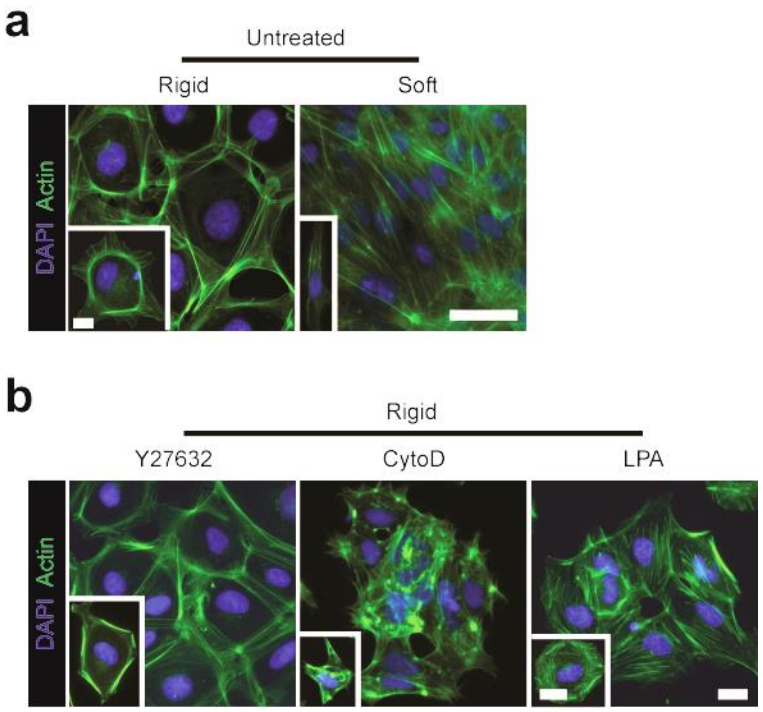

Figure 3-19 Immunofluorescence images showing actin microfilaments in clusters of and single (insert) hESCs cultured in growth media on rigid (E = 1,200 kPa) and soft (E = 5 kPa) PMAs. hESCs were either untreated (**a**) or under treatments with different drugs (**b**) as indicated. Y27632, Rho-associated kinase (ROCK) inhibitor; Cytochalastin D (Cyto D), inhibitor of actin polymerization; Lysophosphatidic acid (LPA), inducer of actin polymerization. Untreated hESCs on rigid PMAs showed mature and thick actin stress fibers, whereas actin stress fibers in untreated hESCs on soft PMAs were diffuse and less evident. Y27632 treatment had no detectable effect on actin stress fibers. CytoD treatment led to depolymerization of stress fibers. LPA facilitated formation of actin bundles in hESCs. Scale bars in **a&b**, 50 μm and 20 μm (insert).

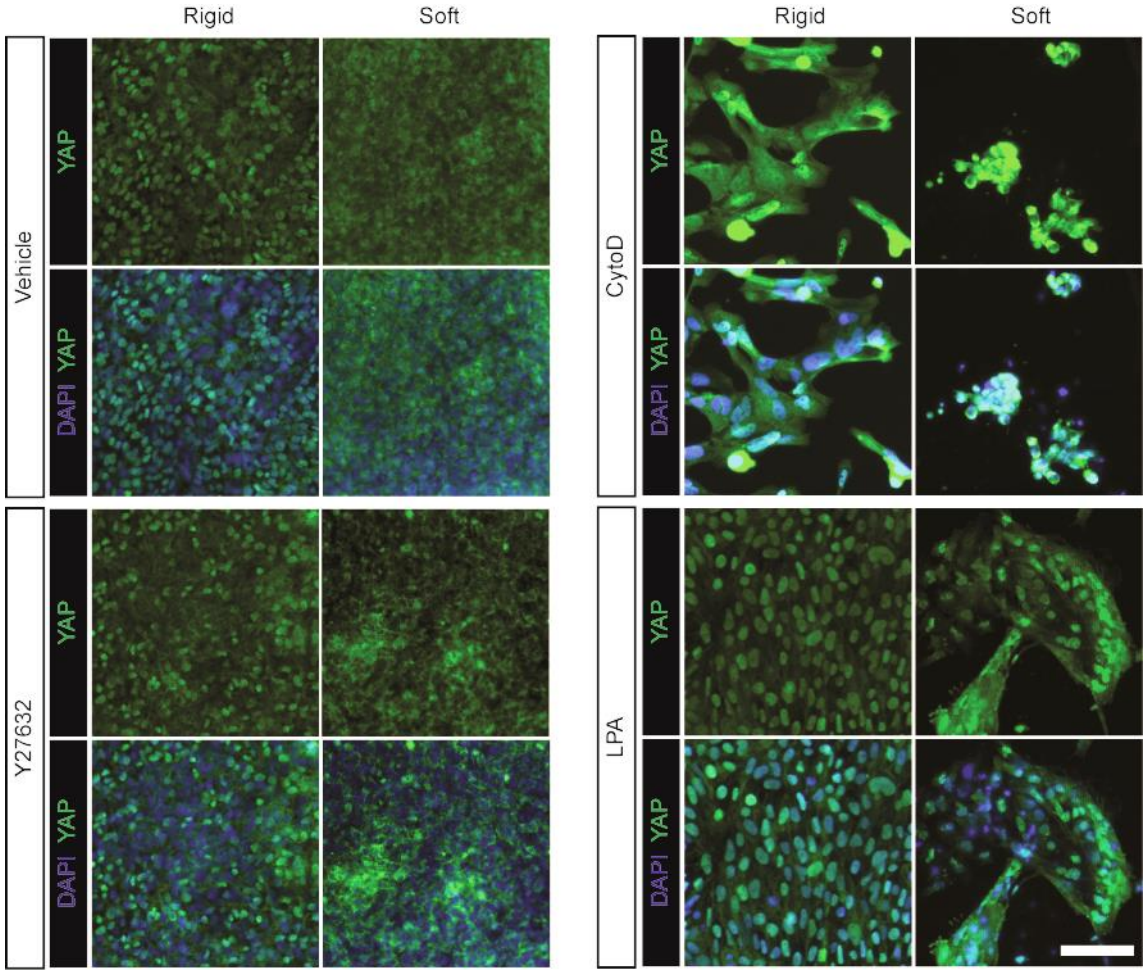

Figure 3-20 Nucleocytoplasmic shuttling of YAP in hESCs regulated by actomyosin contractility and actin cytoskeleton (CSK) integrity. Immunofluorescence images showing subcellular localization of YAP in hESCs on rigid (E = 1,200 kPa) and soft (E = 5 kPa) PMAs. hESCs were cultured for 3 d in neural indcution media supplemented with DMSO (vehicle control; *top left*), ROCK inhibitor Y27632 (*bottom left*), actin polymerization inhibitor cytochalasin D (CytoD; *top right*), and RhoA activator lysophosphatidic acid (LPA; *bottom right*). Scale bar, 100 µm.

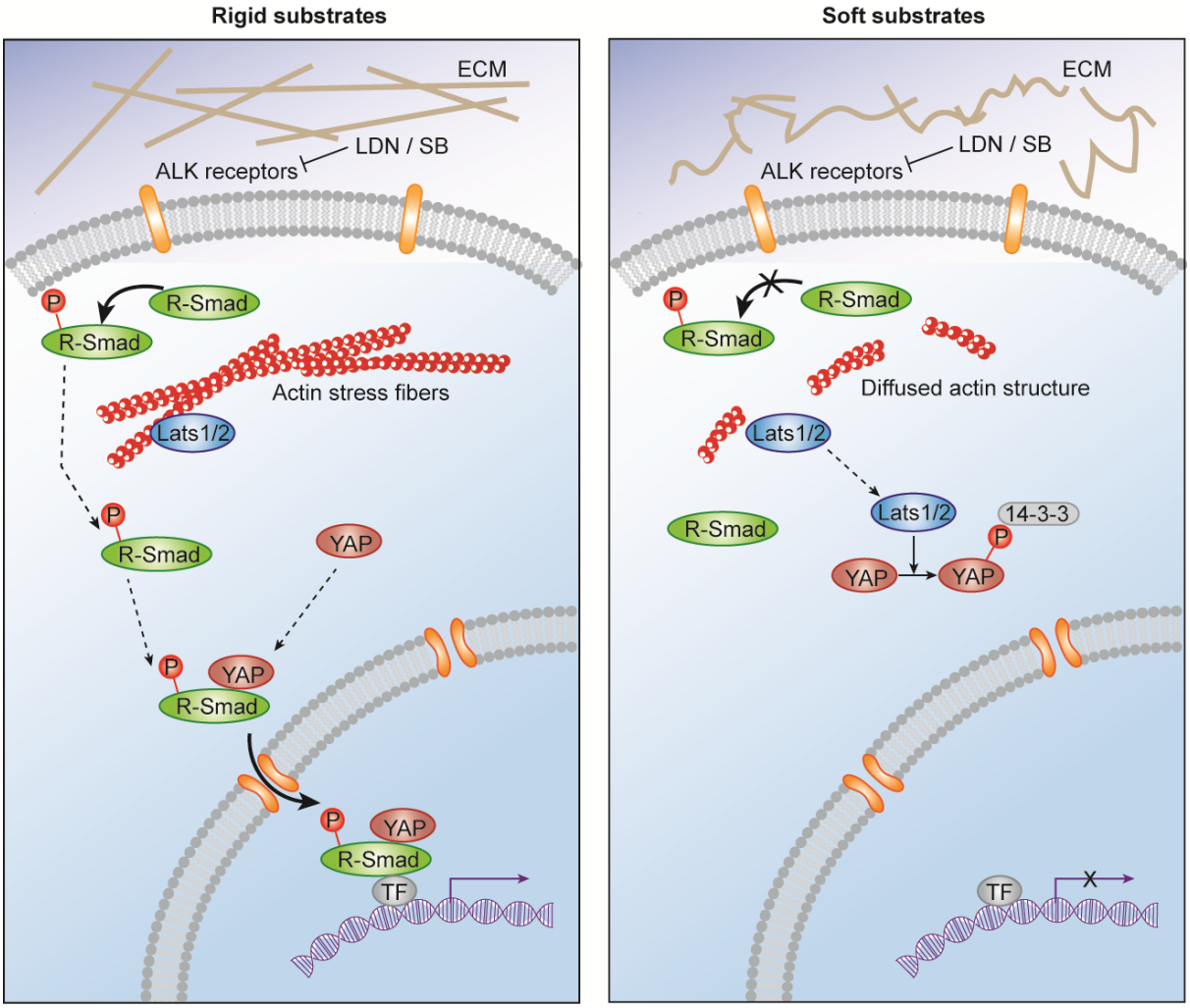

Figure 3-21 A putative mechanotransductive process for rigidity-dependent neural conversion of hPSCs. Activin receptor-like kinase receptors ALK4, ALK5 and ALK7 (inhibited by SB431542) and BMP type I receptors ALK2, ALK3 and ALK6 (inhibited by LDN193189) are activated by extracellular physical cues to phosphorylate Smad proteins. Substrate rigidity directly affects localization or clustering of these cell-surface receptors so that their activation and thus downstream Smad phosphorylation are inhibited on soft substrates. Extracellular matrix is physically tethered to actin cytoskeleton through integrin-mediated cell adhesions, and many intracellular signaling cascades are regulated by dynamics of actin cytoskeleton. It has been reported that Lats, an actin-binding protein, is activated during disassembly of actin microfilaments. Lats phosphorylates YAP, and phosphorylated YAP is retained in the cytoplasm by binding to the scaffolding protein 14-3-3. Non-phosphorylated YAP is required for shuttling of phosphorylated SMAD to the nucleus for transcriptional regulation, such as the neural differentiation program of hPSCs.

Chapter 4

Modeling neural plate development *in vitro*

4.1. Introduction

Understanding the mechanism of human embryo development is not only an extremely intriguing scientific question, but also will shed light on therapeutic approaches for developmental disorders [97]. Currently, developmental biology studies focus on identifying genes and proteins that are important for morphogenesis [98]. Although the role of mechanical forces in driving the morphogenesis has been recognized, how forces are controlled and integrated with biochemical signals are still elusive, largely due to the lack of tools to model human development *in vitro* and to quantify biomechanical forces [99].

Neural plate border (NPB) cells between neuroectoderm cells and epidermal cells give rise to olfactory and lens placodal cells and neural crest cells [100]. The mechanism by which NPB cells are generated remains poorly understood (Figure 4-1). Several studies primarily from Xenopus and chick showed that NPB specification is a result of interactions between adjacent epidermis and / or mesoderm, suggesting that Wnt activation and intermediate BMP levels can induce NPB [101, 102]. More specifically, noggin secreted by notochord inhibits BMP signals and Wnt secreted by paraxial mesoderm activates Wnt signals. A gradient of BMP and Wnt

activity is then established within neural plate based on the diffusion of these signaling molecules. More recent studies revealed that BMP signals are not required until late gastrula stage, and can be induced by Wnt activation localized in the border region of neural plate [103]. However, the spatial control mechanism of Wnt and BMP signals is still unknown.

Although NPB specification is considered as evolutionarily conserved, significant variations in timing, the source of signals and even regulatory genes exist. To fully understand human development, human embryonic stem cells (hESCs) derived organoids offer tremendous

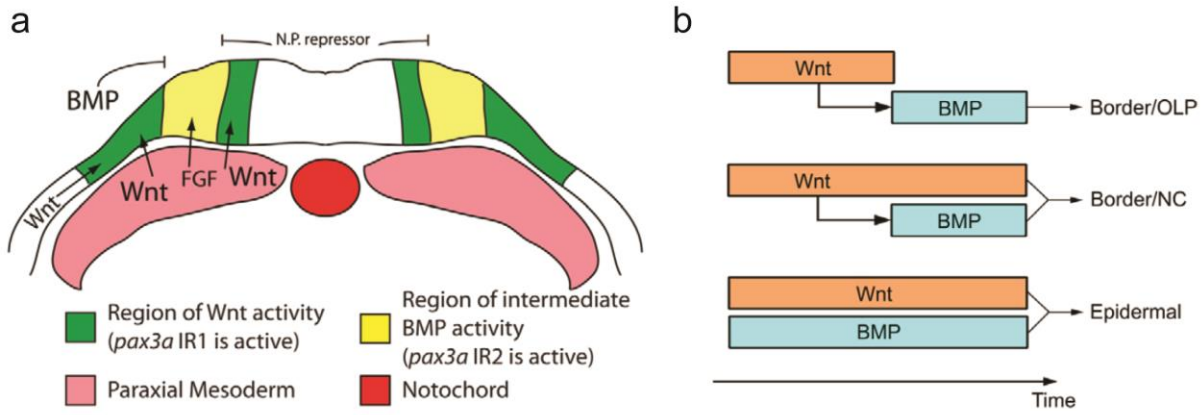

Figure 4-1 Spatiotemporal control of BMP and Wnt signals in neural plate border specification. (**a**) A model for pax3a IR1 and IR2 activity. IR1 is activated by Wnt and FGF signaling in a wide band surrounding the NPB (green). IR2 activity is precisely positioned at the NPB by BMP signaling and a repressive neural plate factor and is amplified by FGF signaling (yellow). Figure adapted from [102] (**b**) Early patterning of the chick non-neural ectoderm isregulated by temporal exposure to Wnt and BMP signals. Proposed Wnt and BMP signaling events required for the specification of rostral and caudal neural plate border cells, and of epidermal cells. Figure adapted from [103].

opportunities to recapitulate human development stages [104-108]. Using hESCs, we previously demonstrated that the rigidity of extracellular matrix is an extracellular regulator of lineage choices between neuroectoderm and NPB, suggesting the important roles of mechanical cues during early neurulation. To fully understand the specific role of these mechanical cues, here we demonstrated a novel method to model and study the NPB specification. Using micropatterning technique to confine hESCs growing areas and introduce geometrical constrains, hESCs

spontaneously differentiated into neural plate and NPB cells, with precise spatial organization. We discovered that mechanical forces and cell shape, synergizing with Wnt and BMP signals, might provide additional instructive guidance to regulate neural plate development.

4.2. Materials and Methods

4.2.1. Neural plate differentiation

Growth media contained DMEM/F12 (GIBCO), 20% KnockOut serum replacement (GIBCO), 0.1 mM β-mercaptoethanol (GIBCO), 2 mM glutamax (GIBCO), 1% non-essential amino acids (GIBCO), and 4 ng mL^{-1} human recombinant basic fibroblast growth factor (bFGF; GlobalStem).

To promote neural induction, TGF-β inhibitor SB 431542 (10 μM; Cayman Chemical) and BMP4 inhibitor LDN 193189 (0.1 μM, unless stated otherwise; Selleckchem) were added into growth media from day 1. CHIR 99021 (3 μm; Tocris Bioscience) was added to growth media at day 2 for 24 hrs.

hESC line H1 (WiCell) was cultured on mitotically inactive mouse embryonic fibroblasts (MEFs; GlobalStem) in growth media with daily medium change. Cells were passaged every 5 d using the STEMPRO EZPassage Disposable Stem Cell Passaging Tool (Invitrogen). Before passaging, differentiated cells were removed manually using a modified pasteur pipette under a stereomicroscope (Olympus). Cells were rinsed briefly with PBS and treated with TrypLE Select (Invitrogen) for 2 min to release MEFs. Cells were rinsed briefly again with PBS before all cells, including hESCs and remaining MEFs, were collected using a cell scraper (BD Biosciences). To remove contaminant MEFs, all cells were transferred onto a 60-mm tissue culture dish (BD Biosciences) coated with gelatin (Sigma) and incubated for 45 min. MEFs

would attach to the dish while hESCs were still in the supernatant. hESCs in the supernatant were collected and centrifuged with the cell pellet re-dispersed in growth media containing Y27632 (10 μM; Enzo Life Sciences).

4.2.2. Microcontact printing

PDMS stamps with patterned relief structures generated using photolithography and replica molding were inked with a vitronectin solution (20 mg/ml; Trevigen) for 1 h, blown dry under nitrogen gas. In parallel, PDMS (hardener and monomer ratio, 1:15) were spin coated (2000 rpm, 30s) on cover glasses and baked for 24 hrs at 60 ^{o}C. PDMS stamps were put into conformal contact with UV-ozone (Jelight) activated PDMS coated cover glasses or PDMS microposts for 30 s and were released by soaking into 100% ethanol.

4.2.3. Scratching assay

hESCs were seeded at high density (80,000 cells/cm2) on vitronectin coated cover glasses and cultured for 24 hrs to reach a monolayer. A scratch was generated in the center of the confluent layer by using a P1000 pipette tip, either at day 2 or day 4 after cell seeding.

4.2.4. Immunocytochemistry

Cells were fixed with 4% paraformaldehyde (Electron Microscopy Sciences) for 15 min and then permeabilized with 0.1% Triton X-100 (Roche Applied Science) for 20 min at room temperature. Primary antibodies (listed in Supplementary Table 2) were used and detected by goat-anti mouse Alexa Fluor 488 and/or goat-anti rabbit Alexa Fluor 546 secondary antibodies.

Percentage of marker-positive cells was quantified with a custom-developed MATLAB program (MathWorks) based on a watershed segregation algorithm.

4.2.5. RNA isolation and quantitative real-time PCR (qRT-PCR) analysis

Total RNA was isolated from cells using RNeasy kit (Qiagen). Real-time PCR (RT-PCR) was performed and monitored using an Bio-rad CFX Connect real time detection system. Quantitative real-time PCR (qRT-PCR) was also performed with SYBR Green PCR mastermix. Human TATA-binding protein (TBP) primers were used as an endogenous control for relative quantifications. Samples in which no expression was detected were given an arbitrary Ct value of 40. All analyses were performed with three replicates. Relative expression levels were determined by calculating $2^{-\Delta\Delta Ct}$ with the corresponding s.e.m.

4.2.6. Western blotting

Whole cell lysates were prepared from cells, separated on SDS-polyacrylamide gel, and transferred to PVDF membranes. NE-PER nuclear and cytoplasmic extraction kit (Thermo Scientific) was used to obtain cytoplasmic and nuclear protein fractions. PVDF membranes were incubated with blocking buffer (Li-Cor) for 1 hr and then incubated with primary antibodies overnight at 4oC. Blots were then incubated with IRDye secondary antibodies (Li-Cor) for 1 hr before protein expression was detected with a Li-Cor Odyssey Sa Infrared Imaging System (Li-Cor).

4.2.7. Fabrication of microchambers

Silicon molds of the microchambers were generated by standard photolithography and reactive ion etching (RIE). PDMS were spin coated on the mold (500 rpm, 90s) to generate a thin PDMS film and were cured at 110 ^{o}C for 20 mins. The PDMS film was then peeled off and bonded to a coverglass through plasma bonding. Distill water was then filled into the channels and chambers and a pressure regulator connected to a compress air outlet was used to apply pressure to deform the PDMS thin film.

4.3. Results and Discussion

4.3.1. Micropatterning induced formation of neural plate-like structure *in vitro*

Neural plate, surrounded by early epidermis and mesoderm, arises in a confined environment. We ask if such mechanical constraint can contribute to the lineage choices of neural plate. hESCs were plated at 5,000 cells/cm^2 on circular micropatterns with a range of diameters from 300 μm to 800 μm and were cultured in growth media supplied with TGF-β inhibitor (SB 431542) and BMP inhibitor (LDN 193189) for 8 days. At day 2, Wnt activator (CHIR 99021, 3μM) was also added to culture media for 24 hrs to stimulate neural crest differentiation. We discovered that at day 8, Pax3$^+$ NPB cells appeared primarily on the border region of the micropatterns, as shown in the representative immunofluorescent images and the heat map of overlapped Pax3 staining images (Figure 4-2a). We also observed that the size of micropatterns also affect the localization of Pax3$^+$ cells. We noticed that on all the patterns, in particular larger patterns (d = 800 μm), Pax3$^+$ cells also showed up in the center of the patterns, with a strong correlation with number of cells on the micropatterns (Figure 4-2b,c). Accumulation of Pax3$^+$ cells on the border regions of patterns appeared only when cell density

are high. When cell density is very low, almost 100% of hESCs differentiated into neural crest cells.

To elucidate whether the curvature of the boundary has an effect, we used an *in vitro* scratch assay to generate a linear gap in the monolayer of hESCs, either at day 1 or day 4 during differentiation. We found that in the scratched area, most cells differentiated into $Pax3^+$ cells, in contrast with unscratched areas (Figure 4-2d).

4.3.2. Mechanical forces are involved in the regionalization of neural crest cells

When a circular patch undergoes shrinkage on a flexible substrate, the strain will vary radially with minimum strain at the center and maximum at the outer radius. It has been observed that in patterned epithelia cells, traction forces accumulated on regions with high curvature [109]. We first examined whether mechanical forces are also involved in the regionalization of NPB cells. We first used micropatterned PDMS micropost arrays (PMAs) to measure intracellular contractility. With low plating density which promotes NPB differentiation, contractile forces of cells at day 2 evenly distributed across the whole pattern, as demonstrated by the representative heat map of the traction forces (Figure 4-3a). In contrast, when cells were plated at high density, traction forces on the periphery of the patterns are significantly larger than the forces in the center of the patterns. These results indicated that cell contractile forces might be involved in the regionalization of $Pax3^+$ NPB cells. Consistent with the traction force measurement, staining of phosphorylated myosin also demonstrated that cells at the periphery of patterns have higher actomyosin activity (Figure 4-3b). To further confirm this hypothesis, we used Y27632, a ROCK inhibitor, and blebbistatin, a myosin inhibitor, to block traction forces (Figure 4-3c). As expected,

with reduced traction forces, Pax3^{+} NPB cells located randomly within the pattern, regardless of cell plating density.

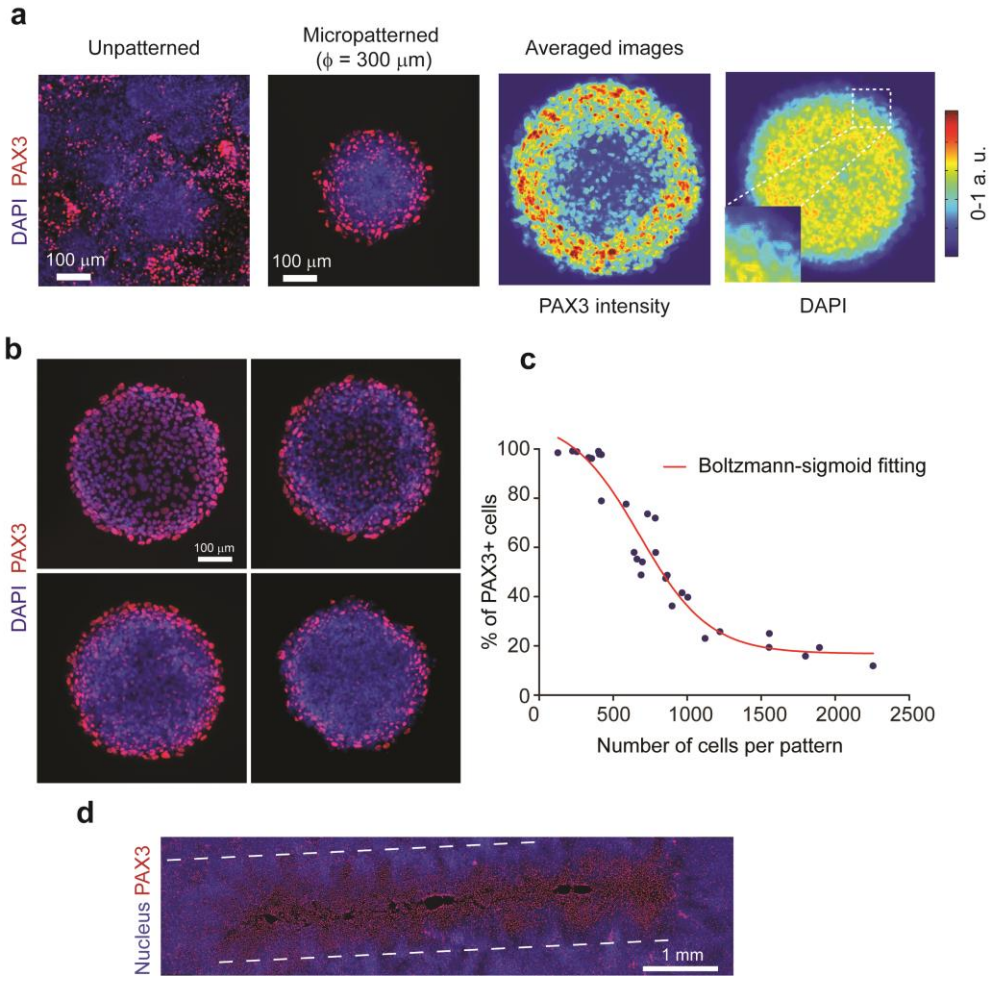

Figure 4-2 Neuronal differentiation of hESCs with geometrical constrains mimic the early neural plate development. (**a**) Representative immunofluorescence images and heat map of average fluorescent intensity showing Pax3+ NPB cells on unpatterned and micropatterned surface. (**b**) Representative immunofluorescence images showing Pax3^{+} NPB cells on patterns with different initial cell density. (**c**) A plot showing the correlation between cell density and percentage of Pax3^{+} NPB cells. (**d**) Representative immunofluorescence images showing Pax3^{+} NPB cells. The scratch was generated at day 1 of differentiation. Data represents the mean ± s.e.m with n = 3.

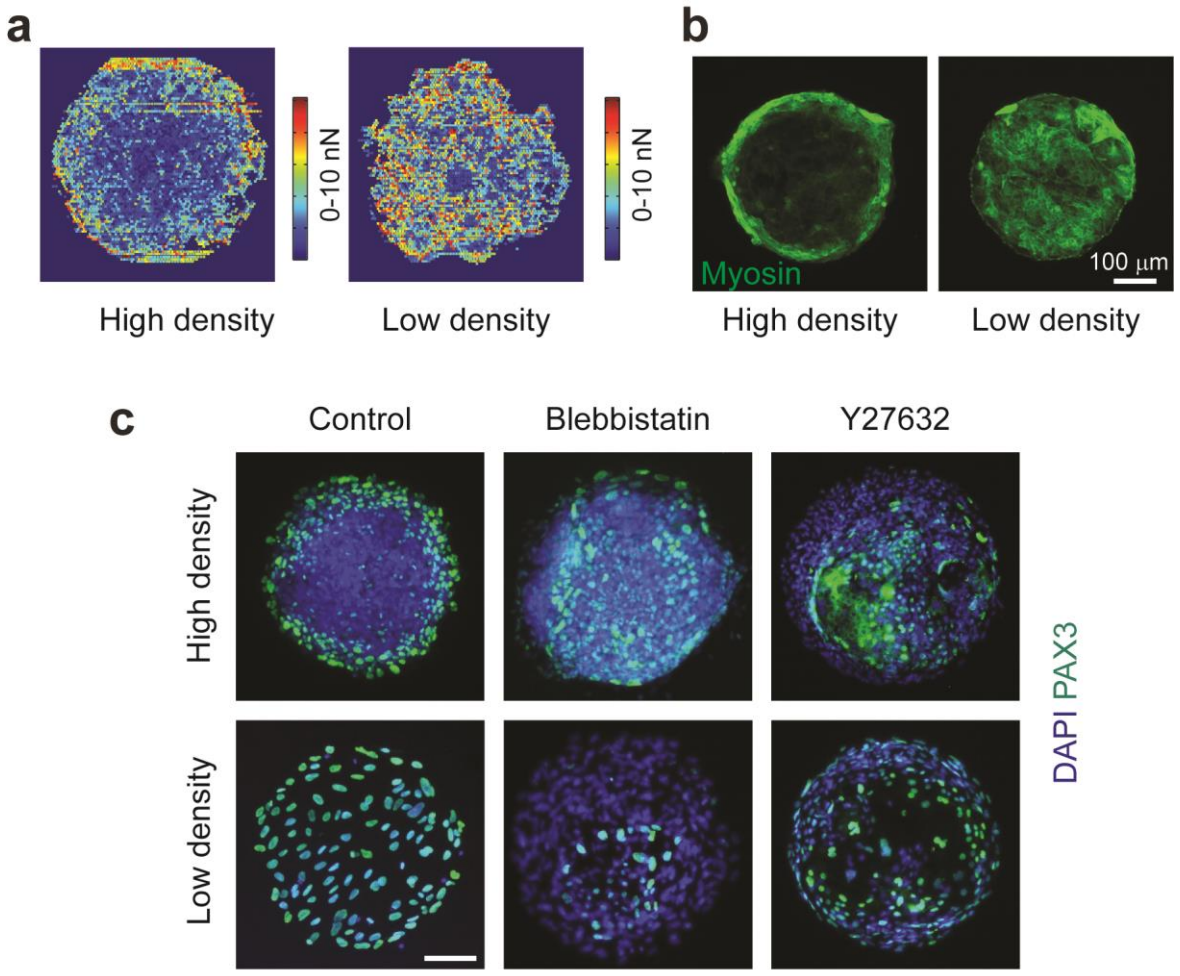

Figure 4-3 NPB regionalization on micropatterns depends on mechanical forces. (**a**) Heat map of the traction forces of hESCs on micropatterns at day 2 of differentiation. (**b**) Representative immunofluorescence images showing myosin expression of hESCs on micropatterns at day 2 of differentiation. (**c**) Representative immunofluorescence images showing Pax3 expression on micropatterns treated with vehicle controls, blebbistatin and Y27632. Scale bar, 100 μm.

4.3.3. Cell shape changes associated with mechanical forces regulate neural crest differentiation

Changes of traction force are often accompanied with changes of cell shape. We therefore stained ZO-1, a cell-cell junction protein, to evaluate the cell projection areas (Figure 4-4a). We observed that at day 2, at high seeding density (> 80,000 cells/cm^2), projection areas of cells at

the periphery of the patterns are significantly larger, compared with cells in the center of the patterns. This finding is consistent with our previous observation that lower seeding density induces NPB differentiation on micropatterns.

Previous report reveals that lower plating density is desirable for the neural crest differentiation [67], which is also confirmed in our system. However, in this assay, it is not clear whether different metabolism status and autocrine signals will affect cell differentiation. The data shown previously using large patterns and scratched surface suggested that, even in the exactly same chemical conditions, cell shape change is sufficient to lead to different cell fate.

To further confirm cell shape is a bona fide property that leads to the NPB differentiation, we used a cell stretching platform to change cell shape during differentiation (4-4b-c). A PDMS film, molded from a silicon mold and patterned with microfluidic channels and chambers, was bonded on a coverglass. When compressed air was applied, the PDMS membranes on top of microfluidic chambers will have uniaxial deformation, allowing additional space for cells to spread. The calibration data showed that over 100% increase could be achieved. hESCs were plated at high density to reach confluence and were stretched for 24 hrs at day 2. We discovered that in the stretched area, 62.6% of cells were $Pax3^{+}$ NPB cells, compared with 12.5% in upstretched control area within the same chip (Figure 4-4d-e). This data strongly suggested that under the chemical environment that supports both neuroepithelial cell and NPB differentiation, change of cell shape alone can regulate the lineage bifurcation in the in vitro neural plate model.

4.3.4. Cell shape mediates BMP but not Wnt activities

Both *in vivo* studies using animal models and *in vitro* studies using embryonic stem cells demonstrated that Wnt activation and moderate BMP activation are required for the neural crest formation [101, 102]. We sought to understand the interaction between biophysical signals (cell shape and/or forces) and these biochemical cues. We first tested whether pharmacological inhibition and activation of Wnt and/or BMP could reverse the effect of cell shape. We found that inhibiting Wnt or BMP signals individually only modestly reduced Pax3 gene expression level when cells were plated at low density, while simultaneous inhibition of these two signals almost completely blocked NPB differentiation (Figure 4-5a). On the other hand, activation of either Wnt or BMP signals can significantly promote Pax3 expression when cells were plated at

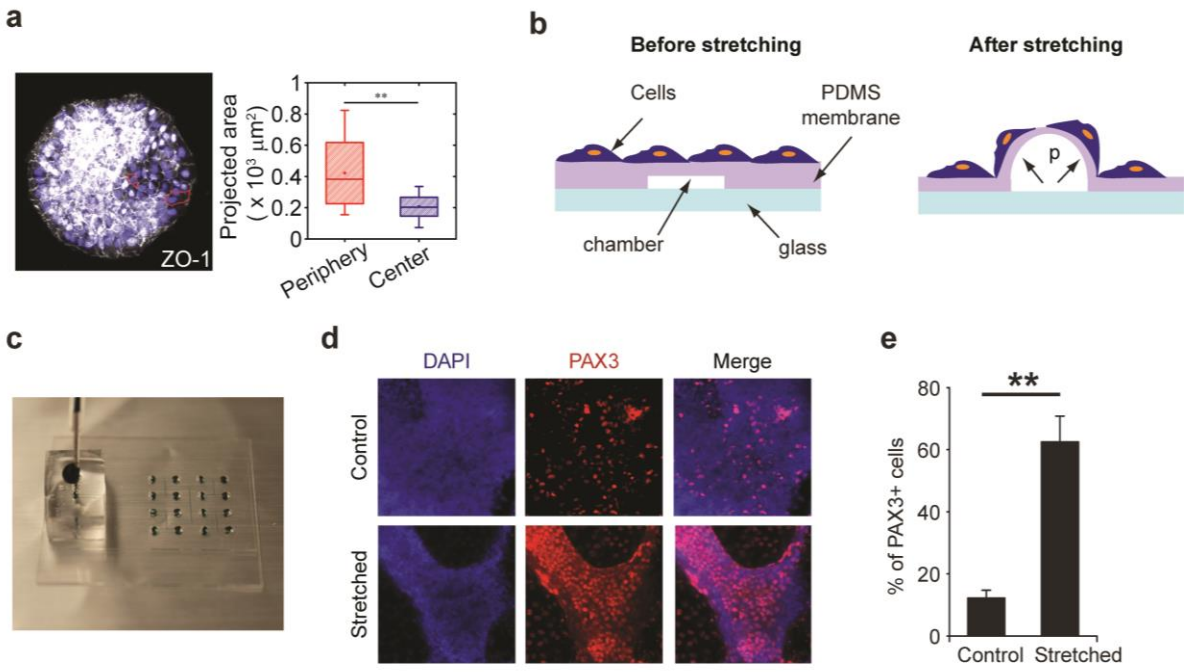

Figure 4-4 Cell shape mediates NPB differentiation. (**a**) Representative immunofluorescence images and bar plot showing ZO-1 staining and quantification of cell projection areas. (**b**) Schematic diagram showing microfluidic devices used to expand cell spreading areas. (**c**) Photograph showing the cell stretching device. (**d-e**) Representative immunofluorescence images (**d**) and bar plots (**e**) showing Pax3 expression on control and stretched areas. Data represents the mean ± s.e.m with $n = 3$. *P*-values were calculated using student t-test. **, $P < 0.01$.

high density, and co-activation of these two signals did not further promote Pax3 gene expression (Figure 4-4a). Similar trend was observed for the expression level of Sox9 (Figure 4-5b), a neural crest marker, suggesting the terminal fate of NPB cells is more likely neural crest cells instead of placodes [110]. Our data suggested that biophysical cues served as upstream regulator rather than downstream effector of Wnt and BMP signals.

Next, we ask how cell shape regulates Wnt and BMP signals. Changing cell plating density is a convenient way to modulate cell shape [111]. Our results in Figure 4-4 also suggest that cell plating density mediated NPB differentiation may result from cell shape changes. We found that expression of BMP target genes Msx1, Id1, and Id3 were downregulated when cells were plated at high density, regardless of the presence of BMP inhibitors or serum replacement (Figure 4-5c-d). In contrast, the expression of Wnt target genes Lef1, Axin2 and Sp5 did not significantly respond to cell plating density, regardless of the presence of CHIR or serum replacement (Figure 4-5e-f). Of note, several conventional Wnt target genes were downregulated when treated with CHIR. The expression of these genes, however, was downregulated when cells were plated at high density (data not shown). Further, to exclude cell-cell interactions, we repeated the same experiments using single cell patterns and discovered that similarly, BMP target genes but not Wnt target genes were responsive to cell shape changes (Figure 4-5g-h). Together, these data suggested that cell shape can directly regulate BMP and Wnt signal activities, revealing a mechano-chemical coupled way to control lineage specification.

In summary, we demonstrated that leveraging micropatterning, ordered spatial distribution of neuroepithelial cells and neural plate border cells found in neural plate can be reestablished spontaneously *in vitro*. Mechanical cues including mechanical forces and cell shape regulate the lineage bifurcation in the in vitro neural plate model likely through BMP signaling.

Our results indicate that i*n vivo*, mechanosensitive BMP activities may synergize with biochemical gradients to ensure robust ectoderm development.

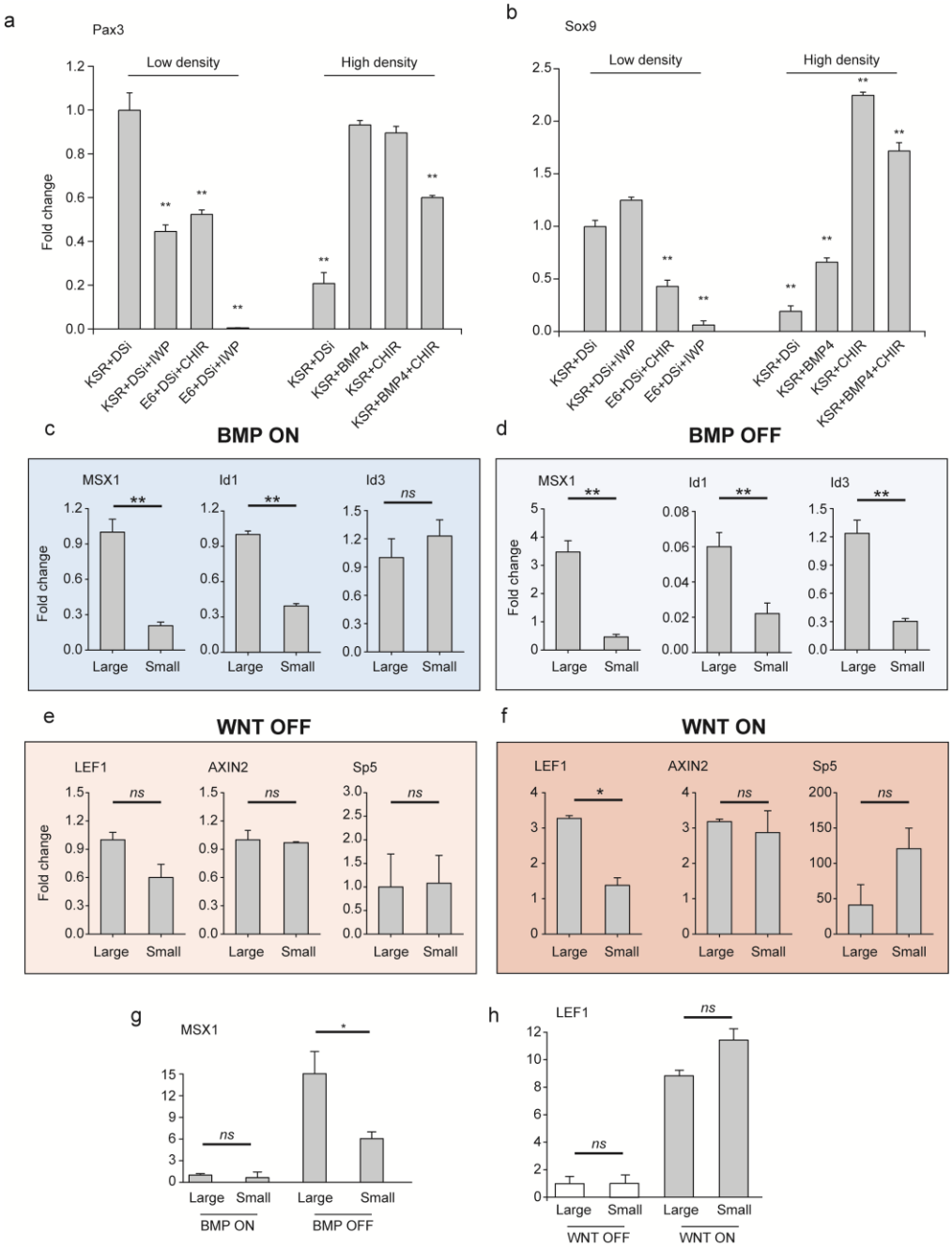

Figure 4-5 Cell shape regulates Wnt and BMP activities. (**a-b**) Bar plots showing the gene expression of Pax3 (**a**) and Sox9 (**b**), with or without BMP and Wnt activities, with high or low seeding density. (**c-d**) Bar plots showing the gene expression of Msx1, Id1 and Id3 under control (**c**) or dual Smad inhibition (**d**) conditions with different initial plating density. (**e-f**) Bar plots showing the gene expression of Lef1, Axin2 and Sp5 under control (**e**) or CHIR 99021 treated (**f**) conditions with different initial plating density. (**g-h**) Bar plots showing expression of Msx1 and Lef1 under different chemical conditions with different cell size confined by single cell micropatterning. Data represents the mean ± s.e.m with $n = 3$. *P*-values were calculated using one-way *ANOVA*, followed by Tukey post hoc analysis. *, $P < 0.05$; **, $P < 0.01$.

Chapter 5

Acoustic tweezing cytometry for stem cell applications

The major content of this chapter is reproduced from our previously published papers: "Acoustic tweezing cytometry for live-cell subcellular modulation of intracellular cytoskeleton contractility" in *Scientific Report*, 2013 [39] and "Improving Survival of Disassociated Human Embryonic Stem Cells by Mechanical Stimulation Using Acoustic Tweezing Cytometry" in *Biophysical Journal*, 2015 [40].

5.1. Introduction

5.1.1. Engineering tools to apply mechanical forces to cells

Mechano-sensitivity or -responsiveness to extracellular biomechanical signals is a fundamental characteristic that controls the function of many types of mammalian cells. However, the molecular mechanism of such mechanotransduction processes is still elusive [1, 15]. Although shear stresses and stretch forces applied to adherent mammalian cells can induce cellular responses such as reorganization of actin cytoskeleton and changes of intracellular contractile force, it is difficult to identify cell membrane receptors responsible for force transmission and converting external mechanical signals into intracellular biochemical events at a subcellular resolution [112, 113]. Optical [114] and magnetic tweezers [115, 116] have been commonly employed to apply local subcellular forces using functionalized microbeads attached to cell membrane via ligand-receptor binding. Optical tweezer can apply forces typically in the

piconewton (pN) range, which is suitable for manipulation of single molecules but not large enough to induce cellular functional responses [117, 118]. Further, optical tweezer can only apply stimuli to one single cell at a time and thus is prohibitive for large-scale, high-throughput cellular functional assays involving many single cells simultaneously. Magnetic tweezer can apply local subcellular pulling force as well as twisting stress in the range of pN to nanonewton (nN) by actuating magnetic beads functionalized with specific membrane receptor ligands [119]. Magnetic tweezer has been successfully applied to mammalian cells to regulate gene expression and even stem cell differentiation [44, 120].

Given the importance of mechanical forces to modulate mechanoresponsive behaviors of cells, as well as the need of new cellular bioengineering tools for high-throughput multiparametric screening and translational applications, it is highly desirable to develop new tools with expanded capabilities that can apply controllable mechanical forces with a subcellular precision on a large number of live single cells simultaneously.

Here we report a novel acoustic tweezing cytometry technique that utilizes ultrasound excitation of membrane-bound gaseous microbubbles to generate controllable subcellular mechanical stimulations to live single cells. Stabilized microbubbles encapsulated by lipids or a thin protein layer have been recently developed successfully as contrast agents for ultrasound imaging in clinical diagnostic radiological applications [121, 122]. Recently, lipid-stabilized microbubbles coated with streptavidin have been developed to enable functionalization of bubbles with specific ligands on the bubble shell encapsulating the gas core. Functionalized bubbles allow selective or targeted attachments of bubbles to mammalian cells via specific ligand-receptor binding, [123-125] enabling *in vivo* ultrasound molecular imaging by recognizing molecular markers associated with specific diseases including inflammation and

angiogenesis [126-129]. In addition, ultrasound excitation of functionalized lipid microbubbles have been exploited for delivering cell-membrane impermeable DNAs, drugs, and other therapeutic compounds from extracellular space into cells [130, 131] by transiently disrupting cell membrane via stable [132, 133] or inertial cavitation (sonoporation) [134]. Ultrasound-induced microbubble activities can generate localized yet significant mechanical impact on cells [132, 134, 135].

Microbubbles are highly responsive to ultrasound excitation owing to a large difference in acoustic impedance between gas inside bubble and surrounding liquid media. Oscillatory positive and negative pressure of an ultrasound field readily induces microbubble expansion and contraction (stable cavitation, resulting in fluid microstreaming), and/or violent collapse (inertial cavitation, which can generate high-speed fluid micro-jet that can penetrate cell membrane) if the pressure amplitude is high enough [136-138]. In addition to rapid volumetric expansion/contraction and collapse of microbubbles, an ultrasound field can also generate a directional force on the bubble, [139-141] recognized as the acoustic radiation force, which can compress the bubble against cell membrane to exert a mechanical force on the cell. The acoustic radiation force resulted from ultrasound stimulated microbubbles can lead to rupture of cell membrane [141]. In this work, we will describe fine-tuned ultrasound conditions to drive displacement of microbubbles without disrupting cell membrane as a way to apply mechanical stimulations to live cells.

5.1.2. Disassociation-associated apoptosis of single hPSCs

The survival rate and cloning efficiency of fully disassociated single hPSCs during enzymatic passaging is extremely low (< 1%), as single hPSCs tend to undergo massive cell

death (apoptosis) upon complete dissociation into single cells. Pharmacological drugs such as Y27632 (a chemical inhibitor of Rho-associated kinase (ROCK)) are currently used to enhance survival and cloning efficiency of fully disassociated single hPSCs. However, long-term effects of these drugs on hPSCs are unclear, and these drugs have been associated with aneuploidy, which is implicated in cell transformation [142]. An alternative method for passaging hPSCs is performed by mechanically fragmenting hPSC colonies into small clusters or clumps and subsequently transferring these cell clusters or clumps to a new tissue culture plate - a tedious, inefficient and difficult process with limited reproducibility and automation possibility. Together, the unique sensitivity of hPSCs to their culture condition has made it difficult in the culture to maintain and expand hPSCs and to efficiently direct their lineage specification. These technical challenges in hPSC culture have prevented the establishment of controllable, reproducible, and scalable fully-defined synthetic culture system for hPSC self-renewal and differentiation, a critical requirement for large-scale applications of hPSCs.

The unique sensitivity of hPSCs to their culture conditions stems mainly from the poorly understood cell-extracellular matrix (ECM) and cell-cell physical interactions of hPSCs with their local cellular microenvironment. The study by Watanabe *et al*. in 2007 has reported that Y27632, a ROCK inhibitor, can drastically rescue the apoptosis and thus improve the survival threshold of single hPSCs [143]. As a result, ROCK inhibitors began to be routinely used in hPSC culture. It has been suggested by several recent studies that dissociation-induced apoptosis of single hPSCs is likely attributable to hyper-activation of myosin-based cytoskeleton tension that is triggered by disruption of cell-cell contacts of hPSCs, and this hyperactive cytoskeleton tension is the upstream regulator and direct cause of hPSC apoptosis [144, 145]. These studied have also suggested that integrin-mediated cell-ECM adhesions disrupted during enzymatic

passaging are not important for dissociation-induced apoptosis of single hPSCs, and E-cadherin-regulated adhesive interactions alone are insufficient to promote survival of hPSCs [64, 144].

Recent studies have suggested that myosin II-mediated cytoskeleton tension and E-cadherin expression can form a positive feedback loop to promote maintenance of pluripotency of hPSCs [61]. Depletion of myosin-II or treatment with blebbistatin, a small molecule inhibitor for myosin-II, for hPSC colonies reduces E-cadherin accumulation at the cell-cell junction sites and impairs the formation of characteristic hPSC colonies [61, 146]. As a result, those hPSC cells show a lower level of alkaline phosphatase activity and reduced expressions of OCT4, SOX2 and NANOG proteins, indicating an impaired status of self-renewal. On the other hand, cell-cell adhesion can directly regulate RhoA signaling [147].

Collectively, these lines of evidence support a possible mechano-sensing and -transduction mechanism based on cell-ECM and cell-cell interactions and involving the RhoA/ROCK/myosin-II signaling axis and its interplay with E-cadherin-mediated cell-cell contacts for regulation of survival of hPSCs. However, so far it has not been tested that if external mechanical forces could be utilized to rescue the apoptosis of disassociated hESCs. In this work, we discovered that using ATC to apply mechanical forces to single hESCs can significantly improve their survival rate.

5.2. Materials and Methods

5.2.1. Fabrication and surface functionalization of PDMS microposts

The PDMS micropost array was fabricated using a protocol described previously.[54] Briefly, a silicon micropost array master was fabricated by standard photolithography and deep

reactive ion etching (DRIE). The height of silicon micropost was modulated by controlling DRIE etch time. The silicon master was silanized with (tridecafluoro-1, 1, 2, 2-tetrahydrooctyl)-1-trichlorosilane (United Chemical Technologies, Bristol, PA) for 4 hrs under vacuum before 1:10 (*w*/*w*, curing agent/base monomer) ratio PDMS prepolymer (Sylgard 184, Dow-Corning, Midland, MI) was poured over the silicon master and cured at 110°C for 20 min. Negative PDMS molds were then peeled off the silicon master, oxidized with oxygen plasma for 1 min (200 mTorr; Plasma Prep II, West Chester, PA), and silanized with (tridecafluoro-1, 1, 2, 2-tetrahydrooctyl)-1-trichlorosilane for 24 hrs. To generate final PDMS micropost arrays, 1:10 (*w*/*w*, curing agent/base monomer) ratio PDMS prepolymer was poured over the negative PDMS mold and degassed under vacuum for 10 min. A clean 25 mm × 25 mm cover glass was then placed on top of the negative mold, and the whole assembly was cured at 110°C for 40 hrs. The final PDMS micropost array was then peeled off the negative PDMS mold. When peeling induced collapse of PDMS microposts, we regenerated the array by sonication in 100% ethanol for 30 sec followed by dry-release with liquid CO_2 using a critical point dryer (Samdri®-PVT-3D, Tousimis, Rockville, MD). The cover glass holding the PDMS micropost array was finally attached to a 35 mm dish with a 20 mm hole at the dish center (MatTek dish; Glass Bottom Dishes, MatTek, Ashland, MA).

To promote cell adhesion, top surface of the PDMS micropost array was functionalized with fibronectin (Sigma, St. Louis, MO) using microcontact printing. Briefly, a flat PDMS stamp made from 1:30 (*w*/*w*, curing agent/base monomer) ratio PDMS prepolymer was soaked in a fibronectin solution (50 μg mL^{-1}) in distilled water for 1 hr at room temperature. The PDMS stamp was then thoroughly rinsed with distilled water and blown dry with a stream of nitrogen. In parallel, the PDMS micropost array was treated with a UV-ozone cleaner (Jelight, Irvine, CA)

for 7 min for surface activation. The PDMS stamp was placed in conformal contact with the PDMS micropost array for 10 sec to transfer fibronectin from the stamp to the top surface of the PDMS micropost array. The PDMS micropost array was then labeled with 5 μg mL^{-1} Δ^9-DiI (Invitrogen, Grand Island, NY) in distilled water for 1 hr. To prevent non-specific protein absorption to non-functionalized surface of the PDMS micropost array, the PDMS micropost array was incubated in 0.1% - 1% (*w*/*v*) Pluronics F127 NF (BASF, Sigma, St. Louis, MO) in distilled water for 30 min at room temperature.

5.2.2. Cell culture

NIH/3T3 mouse fibroblasts (ATCC, Manassas, VA) were maintained at 37°C and 5% CO_2 in a growth medium consisting of low-glucose Dulbecco's modified Eagle's medium (DMEM; Invitrogen) supplemented with 10% bovine serum (Invitrogen), 1% L-glutamine and 1% penicillin/streptomycin. Human mesenchymal stem cells (Lonza, Walkersville, MD) were maintained at 37°C and 5% CO_2 in the MSCGM mesenchymal stem cell growth medium (Lonza). Cells were harvested 8-16 hrs before experiments and seeded as single cells on the PDMS micropost array in the MatTek dish at a density of 3,000 cells cm^{-2}.

5.2.3. Targeted lipid microbubbles and their attachment to cells

Targestar™-SA lipid microbubbles from Targeson (San Diego, CA) were used in this study. Microbubbles (with a mean diameter of 2.3 ± 0.2 μm; $n = 39$) were first mixed with biotinylated Arg-Gly-Asp (RGD) peptides (Peptides International, Louisville, KY) for 20 min at room temperature, with a molar ratio of 5:1 for microbubbles (5×10^8 mL^{-1}) and RGD (0.01 mg mL^{-1}). Following a recommended procedure from the manufacturer, immediately after removal

of culture media in the dish where cells were seeded on the PDMS microposts, 20 μL of the microbubble-RGD mixture was added into the dish. The dish was then flipped upside down for 10 min to allow bubbles to float up towards cells to facilitate binding of microbubbles to the cells. Unbound bubbles were removed by some gentle wash with culture media. The concentration of microbubbles used in this study ensured that for most single cells, only one bubble was attached to cell membrane.

5.2.4. Ultrasound application

An ultrasound transducer (Advanced Devices, Wakefield, MA) driven by a function generator (Agilent Technologies 33250A, Palo Alto, CA) and a 75 W power amplifier (Amplifier Research, Souderton, PA, USA) was used to generate ultrasound pulses to excite microbubbles. The ultrasound transducer was positioned at a 45º angle relative to the horizontal MatTek dish, in order to avoid formation of standing wave in the dish and to permit unobstructed microscopic imaging. The transducer activation surface was submerged in the medium 7 mm (*Rayleigh* distance) away from cells. To further minimize formation of standing waves in the MatTek dish, a chirp technique[148] for ultrasound application was applied. Each ultrasound pulse was produced by sweeping or chirping the driving frequency around the center frequency, *i.e.* 1.1 – 1.4 MHz. The acoustic pressure amplitude of the chirped pulses was further calibrated in a free field using a needle hydrophone (HNR-0500, ONDA, CA, USA).

5.2.5. Videomicroscopy and ultrasound driven microbubble activities

Images of microbubbles excited by ultrasound exposures were acquired using a high-speed camera (FASTCAM SA1, Photron, San Diego, CA; with the frame rate up to 20 Kframes

s^{-1}) and a water immersion 60× objective (1.0 NA; Nikon, Melville, NY, USA) mounted on an inverted fluorescence microscope (Eclipse Ti-U; Nikon). Ultrasound driven bubble activities such their translational movement and change in bubble radius were quantified using commercial image processing software (FASTCAM Viewer 3, Photron). Specifically, bubble displacement was quantified by manually locating the bubble center and tracking its position in each frame. Bubble radius was determined by counting pixels within a manually-defined boundary for the bubble in each frame.

5.2.6. Acoustic radiation force acting on microbubbles

A first-order estimate of the primary acoustic radiation force F acting on microbubbles by an ultrasound field at a resonance frequency of ω_0 was obtained from $F = 2\pi P_A^2 R_0 / (\delta_{tot}\rho_0 c\omega_0)$,[149] where P_A is the acoustic pressure, R_0 is the bubble radius, δ_{tot} is the total damping constant (δ_{tot} = 0.16), ρ_0 is the medium density (1000 kg m^{-3}), and c is the sound speed in media (1500 m s^{-1}). It should be noted that this estimation did not consider the effect of the lipid shell on bubble resonant frequency.

5.2.7. Flow velocity and shear stress generated by ultrasound excitation of microbubbles

Ultrasound driven microbubble expansion and contraction generates microstreaming or flow field near the bubble.[150, 151] We applied the micron-resolution Particle Image Velocimetry (micro-PIV) to measure flow velocity near a bubble, by using 0.5 μm diameter polystyrene particles (Thermo Scientific, CA, USA) as flow tracers. Specifically, tracer particles at a stock solution (1.46×10^{11} particles mL^{-1}) were diluted first in deionized water with a 1:2

(*v/v*) ratio. 2 µL of diluted tracer solution was then added to culture media right before ultrasound applications for cells seeded on the PDMS micropost array in the MetTak dish. Positions of tracer particles near a bubble during ultrasound application were continuously recorded using the high-speed camera at a frame rate of 20 Kframes s^{-1}. Velocities of polystyrene particles and thus the flow field near the bubble were obtained by processing the image sequence using Image J (US National Institutes of Health, Bethesda, MD). Shear stress τ exerted on cell membrane due to microstreaming of fluid was then calculated as $\tau = \mu \Delta v / \Delta y$, where μ is the medium viscosity (7.26×10^{-4} Pa sec), Δv is the flow velocity difference between bubble equator plane and cell membrane, and Δy is treated equal to the bubble radius.

5.2.8. Fluorescence imaging

An air-cooled CCD camera (Photometrics QuantEM, Tucson, AZ, USA) was used for fluorescence imaging. Calcium imaging was performed using a method described previously.[152] Briefly, cells seeded on the PDMS micropost array were first incubated with 10 µM Fura2-AM (Invitrogen) and 0.05% (*w/v*) Pluronic F-127 (Invitrogen) in culture media for 60 min at 37°C and 5% CO_2. Fluorescence emission intensities of Fura2 at 510 nm from cells excited at wavelengths of 340 nm and 380 nm were acquired to generate ratiometric images inferring to intracellular free calcium concentrations.

Changes in cell membrane permeability were assessed by detecting intracellular fluorescence intensity of nucleic acid intercalating agent propidium iodide (PI) (Sigma Aldrich, St. Louis, MO). PI was added into culture media (final PI concentration of 100 µM) right before ultrasound application. Cells were excited at 539 nm, and emission was detected at 610 nm to detect the presence of PI inside cells.

To assess cell viability, calcein AM (Invitrogen) was added into culture media 30 min after ultrasound treatments at a final working concentration of 1 μM. In live cells, non-fluorescent calcein AM is converted to green fluorescent calcein after acetoxymethyl ester hydrolysis by intracellular esterases.

5.2.9. Quantification of cytoskeleton contractile forces using PDMS microposts

Fluorescent images showing the top surface of PDMS microposts were obtained from fluorescence microscopy (Eclipse Ti-U; Nikon) and processed by a custom-developed MATLAB program (MathWorks, Natick, MA; details of the program was described previously[54]) to quantify deflections of PDMS microposts from their unbent, unloaded positions, which were then converted to horizontal contractile forces by multiplying with the nominal spring constant K of the PDMS micropost.

To study spatial distribution of subcellular contractile force changes, we divided cells into two groups based on the relative location of microbubbles on the cells. In the first group, each cell had a bubble attached to a position in the cell peripheral region, defined as the outer 1/3 radial position from the cell centroid. The other group included cells with bubbles attached at locations in the more interior region. Subcellular maps of contractile force changes before and 30 min after ultrasound applications were generated for all individual cells in each group, and these maps were spatially aligned such that microbubbles were aligned along with the nearest cell boundary. All the force change maps for each group of cells were summed up to demonstrate show the overall subcellular contractile force changes based on the microbubble location.

5.2.10. Drug inhibition assays

Cells seeded on the PDMS micropost array in the MatTek dish were treated with Cytochalasin D (40 μM; Invitrogen), Blebbistatin (100 μM; Sigma) and Y-27632 (10 μM; Enzo Life Sciences, Farmingdale, NY) in culture media for 30 min before applying ultrasound to activate lipid microbubbles attached to cells.

5.3. Results

5.3.1. Ultrasound tweezing cytometry to control subcellular contractile response

To study ultrasound-mediated changes in intracellular cytoskeleton contractility, we utilized an elastomeric micropost array we have recently developed as subcellular live-cell force sensors to quantify intracellular contractile forces [31]. The micropost array consists of an array of uniformly spaced, vertical, elastomeric posts fabricated using photolithography and replica molding with silicone elastomer polydimethylsiloxane (PDMS) (Figure 5-1A). After adhesive proteins are coated using microcontact printing on the post tips, cells are able to adhere, spread out, and exert contractile forces that deflect underlying posts. Each post, therefore, functions as a cantilever, capable of measuring local cellular traction force exerted at the post tip. For tip deflections δ that are small compared to the post height L, the PDMS post can be modeled as a linearly elastic beam subjected to pure bending. Thus, intracellular contractile force F applied at the tip of the PDMS post can be calculated as $F = 3\pi Ed^4\delta / (64L^3)$, where E is the elastic modulus of PDMS and d is the post diameter. In this study, NIH/3T3 fibroblasts and hMSCs were first seeded as single cells on fibronectin-coated PDMS microposts. Individual lipid

microbubbles with a mean diameter of 2.3 μm and functionalized with Arg-Gly-Asp (RGD) peptides using avidin-biotin conjugation chemistry were then attached to the cells through specific binding to integrins on cell membrane.

We first applied low amplitude ultrasound pulses with a peak negative pressure of 0.05 MPa, center frequency of 1.25 MHz, pulse repetition frequency (PRF) of 1 Hz, and duty cycle of 5% (i.e., pulse duration of each individual pulse was 50 ms) to stimulate individual NIH/3T3 fibroblasts with one microbubble attached to cell membrane for a total period of 10 sec. A gradual and sustained increase of intracellular cytoskeleton contractile force in NIH/3T3 fibroblasts was observed immediately after ultrasound application (Figure 5-1B). Total cytoskeleton contractility of NIH/3T3 fibroblasts increased up to 148.5% ± 3.6% (mean ± standard error of mean) (n = 31) 30 min after ultrasound stimulation compared to pre-ultrasound contractile levels. Cytoskeleton contractile response to ultrasound excited microbubbles appeared to be dose-dependent (Figure 5-1C&D). For ultrasound stimulation for 20 sec with other ultrasound parameters remained unchanged, the total cytoskeleton contractility of NIH/3T3 fibroblasts at 30 min after ultrasound exposure increased to 163.7% ± 5.0% (mean ± standard error of mean) of pre-ultrasound contractile levels (n = 10; Figure 5-1C&D), significantly higher than the contractile force increase observed for 10 sec ultrasound exposure (p = 0.02 from a student's t-test). NIH/3T3 fibroblasts examined in control groups without microbubbles attached or without ultrasound treatments exhibited no observable change in cytoskeleton contractile force (Figure 5-1D). Ratiometric calcium imaging using calcium indicator Fura-2-acetoxymethyl ester (Fura-2AM) showed that mechanical stimulations of cells with ultrasound conditions used in Figure 5-1 caused no change in intracellular calcium ion concentrations ([Ca2+]i), indicating

an absence of based cell viability assay performed 30 min after ultrasound stimulations showed that NIH/3T3 fibroblasts were able to convert non-fluorescent calcein AM into green fluorescent calcium signaling initiation (Figure 5-1B, C&E). Further, no intracellular entry of cell-membrane impermeant propidium iodide (PI) was detected, indicating that ultrasound stimulation in Figure 5-1 did not cause cell membrane disruption (Figure 5-1F). Calcein AM-calcein and confine it inside cell cytoplasm, indicating cell viability (Figure 5-1F).

To demonstrate that cytoskeleton contractile response to ultrasound tweezing was not cell-type specific, we applied the same ultrasound stimulation used in Figure 5-1 for 10 sec to single live hMSCs. Total cytoskeleton contractility of hMSCs increased up to 148.2% ± 9.8% (mean ± standard error of mean) (n = 8) 30 min after ultrasound exposure compared to pre-ultrasound contractile levels (Figure 5-2), an enhancement comparable in magnitude to that observed for NIH/3T3 fibroblasts.

Taken together, our results in Figure 5-1 and Figure 5-2 demonstrated a sustained cytoskeleton contractility increase in both NIH/3T3 fibroblasts and hMSCs resulted directly from ultrasonic excitation of cell membrane bound lipid microbubbles without membrane disruption or calcium signaling initiation. Our results were consistent with previous studies using optical and magnetic tweezers, where mechanical stimulations of microbeads functionalized with RGD peptides attached on cell membranes lead to cytoskeleton contractility increase at adhesion contacts between microbeads and cell membrane [153].

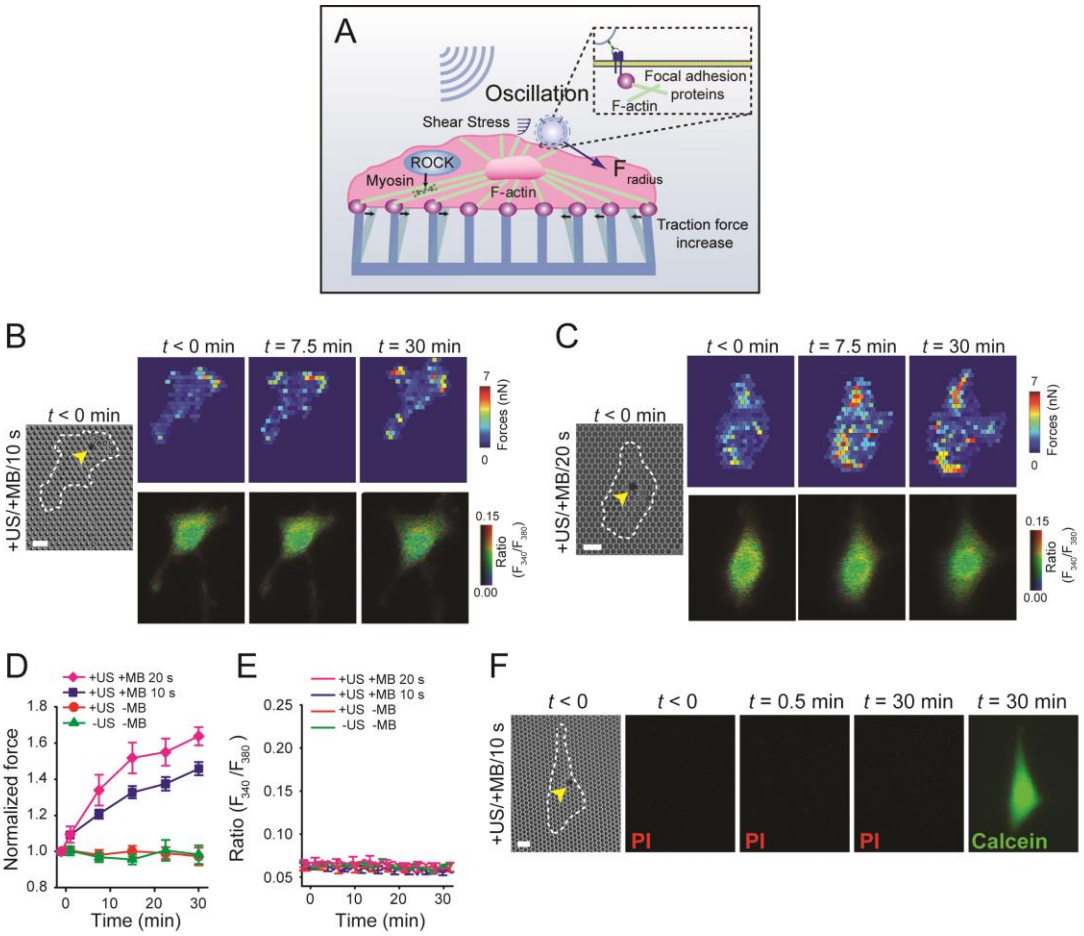

Figure 5-1 Modulation of subcellular cytoskeleton contractility by ultrasound (US) excitation of microbubbles attached to cell membrane ("acoustic tweezing cytometry"). (A) A schematic showing US excitation of microbubbles (MB) attached via RGD-integrin binding to the membrane of a cell seeded on the PDMS micropost array. (B&C) Single NIH/3T3 fibroblasts with one MB (arrow head) attached to cell membrane and subjected to 10 sec (B) or 20 sec (C) US stimulations. Subcellular contractile force distributions (top panels) and pseudocolor ratio images of intracellular free calcium concentration ($[Ca^{2+}]$) (bottom panels) before ($t < 0$ min) and after US application were shown. Scale bars, 10 μm. (D) Temporal evolution of total cytoskeleton contractile force (normalized to contractility before US excitation). (E) Fluorescence ratio representing $[Ca^{2+}]$ as a function of time. Data in D and E are shown as mean ± s.e.m. $n = 31$ for 10 sec US exposure, and $n = 10$ for 20 sec US stimulation. Control groups without MBs attached and treated with ($n = 8$) or without ($n = 10$) US were included for comparison. (F) No intracellular propidium iodide (PI) was detected in NIH/3T3 fibroblasts with MBs attached after US stimulation. Calcein AM essay showed the same cell could convert calcein AM into green fluorescent calcein and confine it within cell cytoplasm. US parameters used in Fig. 1: US frequency of 1.25 MHz, acoustic pressure of 0.05 MPa, PRF of 1 Hz, and duty cycle of 5%.

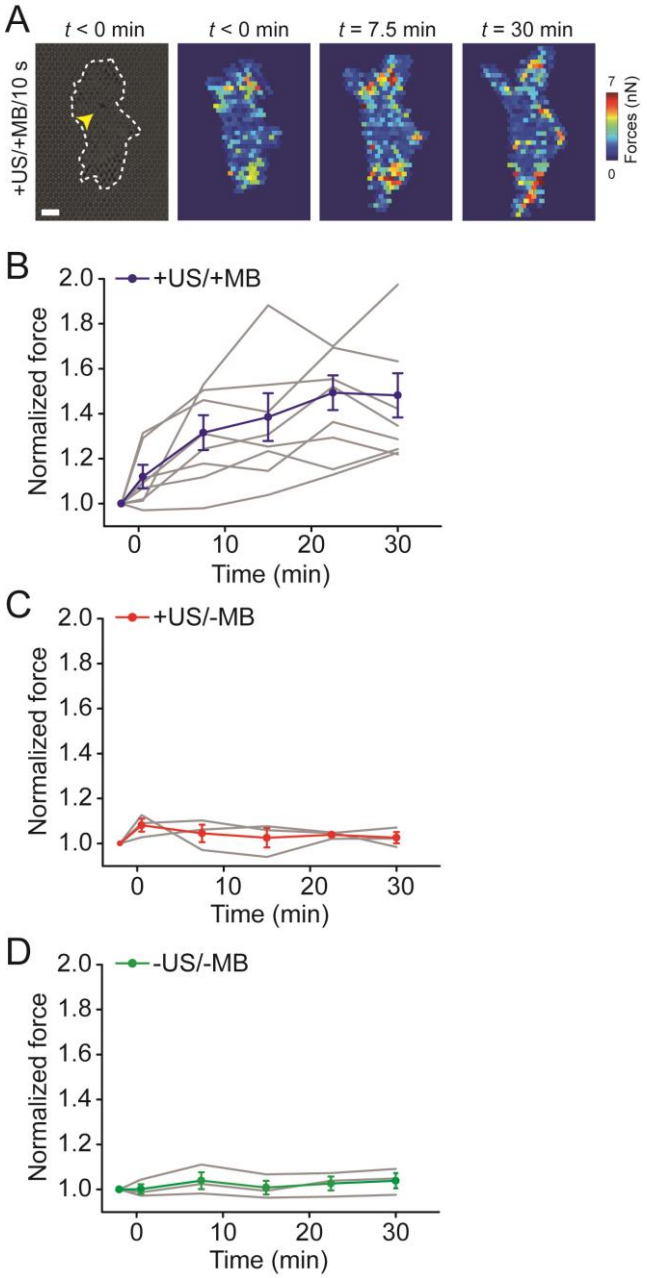

Figure 5-2 (A) Brightfield and colorimetric images showing individual hMSCs and their subcellular cytoskeleton contractile force maps before (t < 0 min) and after 10 sec stimulation with acoustic tweezing cytometry. Scale bar, 10 μm. (B-D) Temporal evolution of total cytoskeleton contractile force (normalized to contractility before US applications) for individual hMSCs (thin grey lines) and population means (colored lines with symbols). hMSCs were treated under different conditions as indicated. For B, individual hMSCs was attached with one microbubble and was exposed to 10 sec US stimulation (n = 8). Control groups without MBs attached and treated with (C; n = 3) or without (D; n = 3) US were included for comparison. US was applied at t = 0 min, with a peak negative pressure amplitude of 0.05 MPa, PRF of 1 Hz, and duty cycle of 5%. Data plotted in B-D using colored lines with symbols are means ± s.e.m.from hESCs as a function of both substrate rigidity and differentiation period. Data represents the mean ± s.e.m with n = 3.

5.3.2. Ultrasound excitation of microbubbles with membrane disruption

To investigate how cytoskeleton contractile force would respond to ultrasound excitation of microbubbles with membrane disruption, we applied ultrasound pulses with a greater acoustic pressure (0.13 MPa) and shorter pulse duration (8 μs) to excite microbubbles attached to cell membrane. (These parameters have been shown previously to be capable of generating sonoporation of cells with localized membrane disruption.28) Under such ultrasound stimulations, cytoskeleton contractile force of NIH/3T3 fibroblasts immediately decreased before slowly recovering to the contractile level prior to ultrasound treatments (top panel in Figure 5-3A&B). Transient calcium influx was simultaneously observed in ultrasound-stimulated cells, as indicated by a rapid increase of intracellular Fura-2 fluorescence intensity after ultrasound stimulations (bottom panel in Figure 5-3A&C). For NIH/3T3 fibroblasts in a control group without microbubbles attached, cytoskeleton contractile force and [Ca2+]i remained unchanged under the same ultrasound perturbation (Figure 5-3B&C). Further, PI uptake into cells at subcellular locations where lipid microbubbles were attached was detected after ultrasound application (Figure 5-3D), suggesting transient cell membrane disruption by ultrasonic excitation of lipid bubbles. Calcein AM-based cell viability assay performed 30 min after ultrasound application confirmed cell viability (Figure 5-3D).

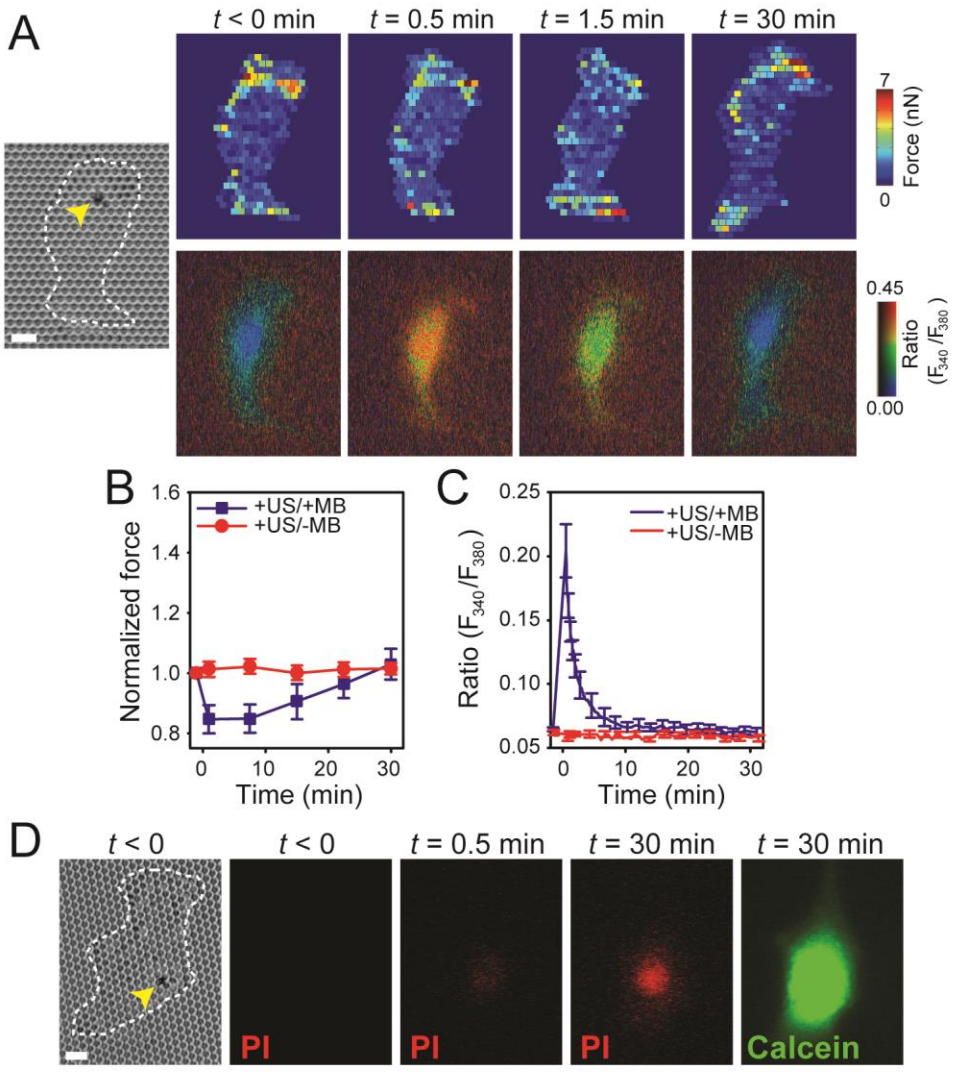

Figure 5-3 Transient disruption of cell membrane by acoustic tweezing cytometry induced transient calcium influx and rapid cytoskeleton contractile force decrease. (A) Brightfield image (left) showing a single NIH/3T3 fibroblast attached with one MB (arrow head) before US stimulation (t < 0 min). Subcellular cytoskeleton contractile force distributions (top panel) and pseudocolor ratio images of [Ca^{2+}] (bottom panel) before (t < 0 min) and after US exposure were included. Scale bar, 10 μm. (B) Temporal evolution of total cytoskeleton contractile force (normalized to contractility before US excitation). (C) Fluorescence ratio representing [Ca^{2+}] as a function of time for NIH/3T3 fibroblasts exposed to US excitation. Data in B & C are shown as mean ± s.e.m. n = 10 for cells attached with one MB, and n = 10 for cells without MBs attached. (D) Excitation of microbubble resulted in transient pore formation on cell membrane, as indicated by emergence of PI fluorescence at the MB attachment location (arrow head). Calcein viability assay performed 30 min after US excitation showed that the cell was able to convert non-fluorescent calcein AM into green fluorescent calcein and confined it within cell cytoplasm. US parameters used in Fig. 2: acoustic pressure of 0.13 MPa and duration of 8 μs.

5.3.3. Subcellular distribution of cytoskeleton contractile force response

We next examined the effect of the attachment location of microbubble on subcellular distribution of reactive cytoskeleton contractile force increase. We divided NIH/3T3 fibroblasts examined in Figure 5-1 into two groups based on the location of microbubble on cell membrane. In the first group (n = 15), each cell had a microbubble attached to the cell periphery region (i.e. outer 1/3 region from cell centroid) (see Methods), while in the other group (n = 16), each cell had a bubble attached to the cell central area. Contractile force maps obtained by summation of the contractile force change for each cell with the bubble location aligned (Figure 5-4) showed that when the microbubble was attached to cell periphery, cytoskeleton contractile force enhancement was concentrated in the local subcellular area surrounding the bubble (Figure 5-4A). In contrast, when the bubble was located near cell centroid, contractile force increase was distributed evenly across entire cell area (Figure 5-4B). It should be noted that the total contractile force increase for the two cell groups was of a similar magnitude (Figure 5-4C).

5.3.4. Actin, myosin II and RhoA/ROCK signaling required for cytoskeleton contractile response to ultrasound tweezing

The actin cytoskeleton consists of multiple molecular structures and components, with actin microfilaments and myosin II molecules as primary determinants for intracellular force transmission properties. RhoA/ROCK signaling is also critically involved in mechanotransduction and regulation of intracellular cytoskeleton contractility [1, 142, 154]. To investigate functional roles of actin polymerization, myosin II activity and RhoA/ROCK signaling in regulating ultrasound-mediated contractile force enhancement, we treated NIH/3T3 fibroblasts with small molecule inhibitors to target specifically actin polymerization

(cytochalastin D, an inhibitor of actin polymerization), myosin II activity (blebbistatin, a myosin II ATPase inhibitor), and RhoA/ROCK signaling (Y27632, a ROCK inhibitor) (Figure 5-5). NIH/3T3 fibroblasts attached with microbubbles were first treated with individual drugs for 30 min before stimulated by ultrasound. Cytoskeleton contractile forces of drug-treated NIH/3T3

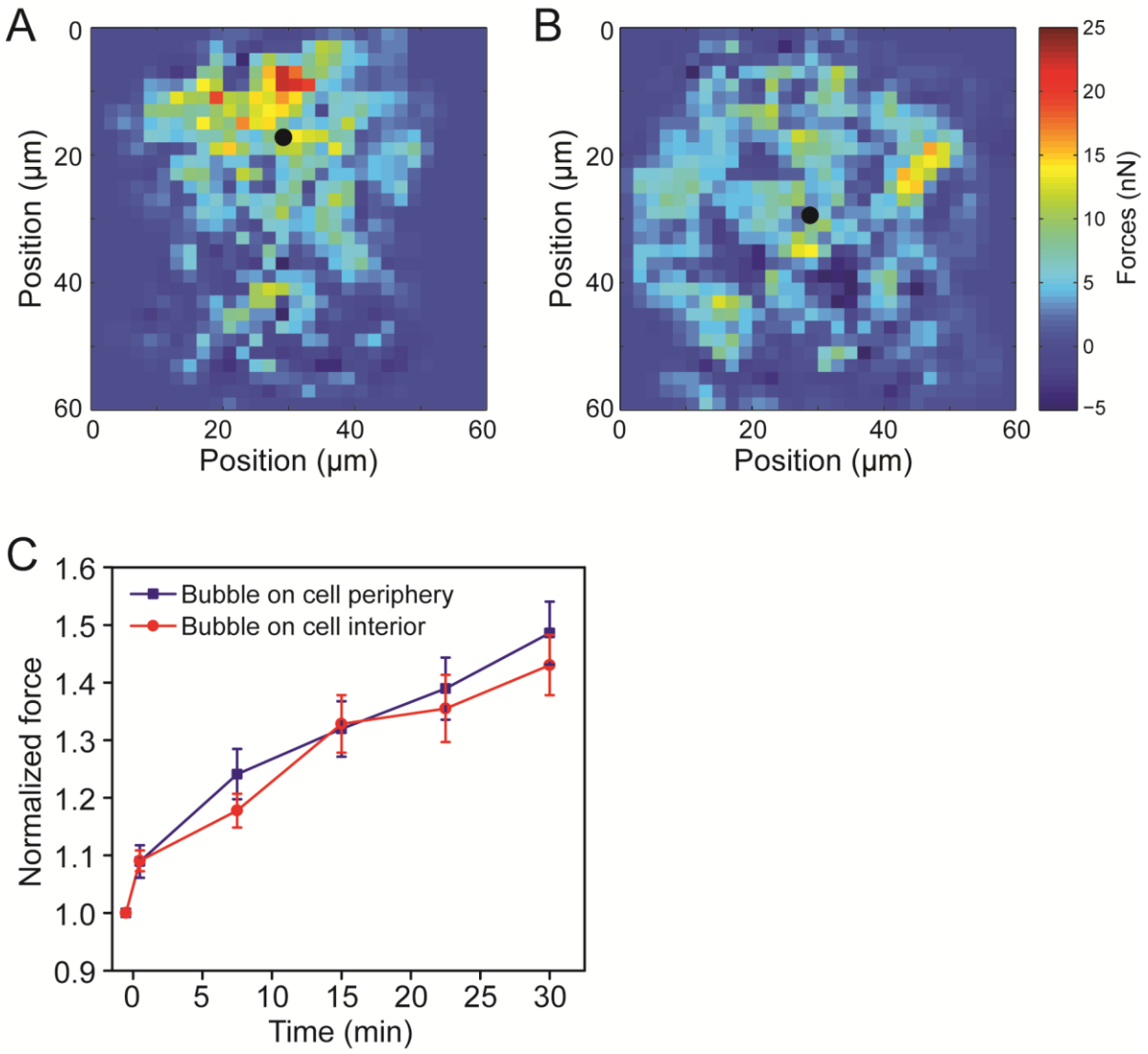

Figure 5-4 Dependence of subcellular distribution of contractile force increase on MB attachment location. (A&B) Colorimetric maps showing summation of contractile force increase for individual NIH/3T3 fibroblasts, with MB on each cell aligned at the same location (black circle). For A (n = 15), MB was located within the outer 1/3 region to the cell periphery. For B (n = 16), MB was located within the cell interior region. (C) Temporal evolution of total cytoskeleton contractile force (normalized to contractility before US excitation) for the two groups of cells where MBs were located either close to cell periphery (*blue*) or within the cell interior region (*red*).

fibroblasts decreased rapidly within the first 10 min after the onset of drug treatments before reaching an equilibrium contractile state at the end of the 30-min period (data not shown). More specifically, after 30-min treatments with cytochalastin D, blebbistatin, and Y27632, cytoskeleton contractile forces of live single NIH/3T3 cells decreased by 70.1% ± 4.5% (n = 5), 71.2% ± 9.3% (n = 5), and 60.0% ± 4.5% (n = 4), respectively. Interestingly, drug-treated NIH/3T3 fibroblasts did not show any contractile force response after the same ultrasound stimulations used in Figure 5-1 (acoustic pressure 0.05 MPa, center frequency 1.25 MHz, PRF 1Hz, duty cycle 5%, and total stimulation 10 sec), supporting that cytoskeleton integrity, myosin II activity, and RhoA/ROCK signaling were all required for ultrasound induced cellular biomechanical responses.

5.3.5. Shear stress and microbubble displacement induced by ultrasound tweezing

To investigate the biomechanical mechanism(s) underlying ultrasonic bubble excitation-mediated cytoskeleton contractile force enhancement, we employed high-speed imaging to examine in situ bubble activities driven by ultrasound exposures. We observed that microbubbles exhibited translational movements or displacements relative to their original location on cell membrane when stimulated using ultrasound. As shown in Figure 5-6A, using the same ultrasound condition as in Figure 5-1 (acoustic pressure 0.05 MPa, center frequency 1.25 MHz, PRF 1Hz, and duty cycle 5%), a microbubble initially bound to cell membrane was pushed away from and then pulled back to its original position repeatedly during ultrasound stimulation, and such periodic bubble displacement corresponded temporarily with pulsed ultrasound exposures. During ultrasound "pulse-on" periods, the microbubble was pushed away in the ultrasound propagation direction by the primary acoustic radiation force acting on the

bubble (Figure 5-6A&B). Assuming a plane ultrasound field, the maximum acoustic radiation force on a bubble with a radius of 2.3 μm was estimated to be 17.0 nN (see Methods), comparable in magnitude to mechanical forces generated by magnetic tweezers [119]. During ultrasound "pulse-off" periods, the microbubble was pulled back partially or fully sometimes to its original position, indicating a biomechanical recovery process dictated by elastic properties of the bubble-focal adhesion-cytoskeleton mechanical linkage after release of external acoustic force.

Besides bubble displacement, the rapid volumetric expansion and contraction of microbubbles driven by ultrasound excitation can generate fluid flow (microstreaming) and thus shear stress on cells.[155-157] Shear stress exerted on cells were estimated from the peak fluid flow velocity near the bubble measured using the Micron-resolution Particle Image Velocimetry (micro-PIV) (see Methods; the peak velocity was 20.15 ± 3.92 mm/s (n = 28) corresponding to a maximum shear stress exerted on cell membrane of 7.05 ± 1.41 Pa). Note that our calculation was based on the peak value of a pulsatile shear stress field surrounding a microbubble during the 10-sec pulsed ultrasound application. Thus, the time-averaged shear stress during the whole ultrasound stimulation was much less. It has been reported that sustained shear stress above a value of 1 – 2.5 Pa can affect behaviors of NIH/3T3 fibroblasts;[158] however cells examined in such studies have been exposed to a sustained shear stress for > 8 hr.

A time-resolved measurement of actual bubble expansion and contraction at the ultrasound frequency of 1.25 MHz and with the ultrasound pulse of 50 ms is technically challenging and requires a frame rate above several Mframes per sec. Nonetheless, we recorded high-resolution images of microbubbles during the entire ultrasound application duration (10 sec) at a frame rate of 20 kframes per sec to assess changes of bubble size. We observed that

microbubbles gradually reduced their size during ultrasound application (Figure 5-6C), likely owing to disruption of bubble lipid shell during repeated bubble expansion and contraction, causing gas diffusion out of bubble [130]. A reduction of microbubble size resulted in a decrease of acoustic radiation force acting on the bubble, leading to a shortened bubble displacement driven by later pulses as shown in Figure 5-6B. The total or accumulative forward displacement of a microbubble during the entire 10-sec ultrasound application period appeared to be positively correlated with the overall cytoskeleton contractile force increase during the 30-min observation period (Figure 5-6D) ($R2 = 0.72$ and $n = 13$), suggesting the important role of the physical displacement of integrin-mediated cell adhesion in regulating cytoskeleton contractile force response. The broad distribution of accumulative displacement of microbubbles was attributable to the bubble initial size distribution (and thus different acoustic radiation forces acting on bubbles) as well as inevitable variations in RGD-integrin binding and their intracellular connection to actin cytoskeleton.

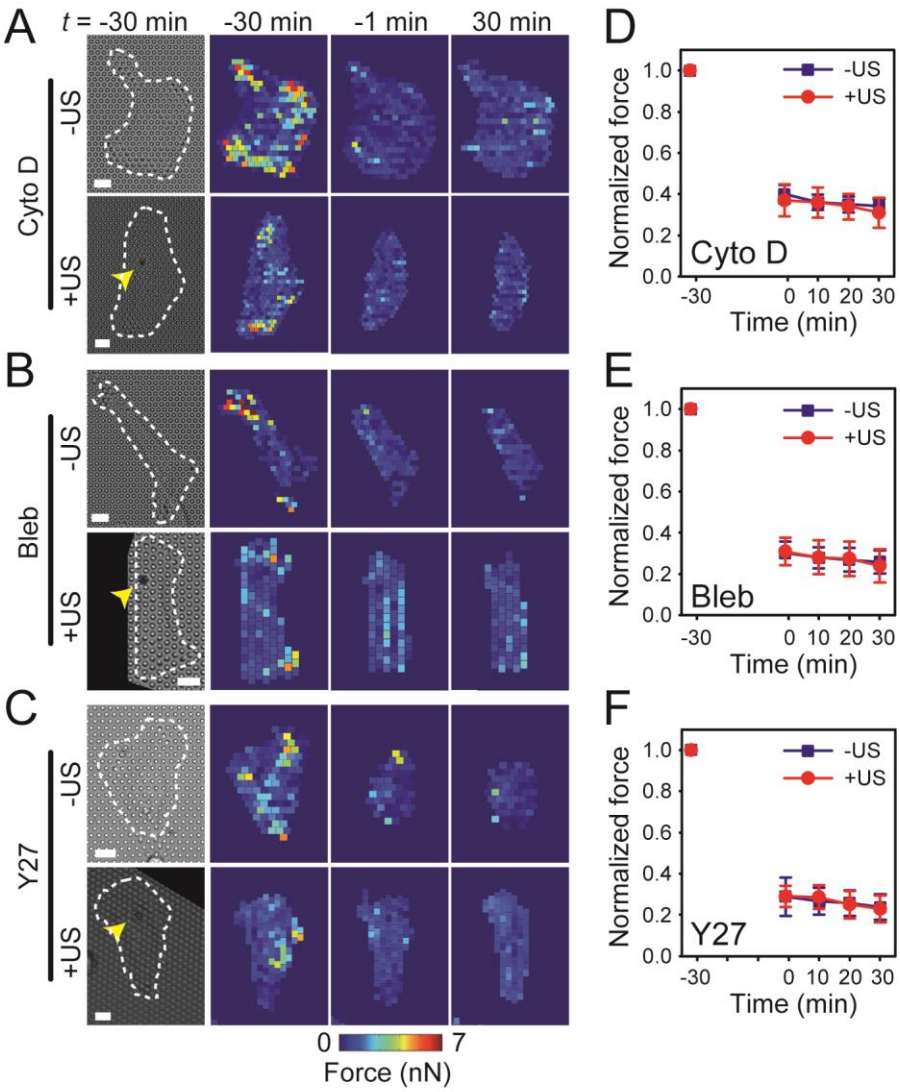

Figure 5-5 Dynamic regulation of cytoskeleton contractility by acoustic tweezing cytometry was ROCK dependent and required intact actin cytoskeleton and actomyosin activity. (A-C) Representative brightfield images (left) showing single NIH/3T3 fibroblasts with (bottom panel) or without (top panel) one MB (arrow head) attached to cell membrane, with the cells attached with MBs treated with 10 sec US stimulation at t = 0 min. Pharmacological drugs were added to culture media 30 min before US application (t = -30 min): Cytochalasin D (40 μM; A), Blebbistatin (100 μM; B), and Y-27632 (10 μM; C). Corresponding colorimetric maps of subcellular contractile force distribution right before drug treatments (t = -30 min), 1 min before US application (t = -1 min), and 30 min after US application (t = 30 min) were included as indicated. The US pulses with a center frequency of 1.25 MHz had a peak negative pressure of 0.05 MPa, PRF of 1 Hz, and duty cycle of 5%. Scale bars in A-C, 10 μm. (D-F) Evolution of total cytoskeleton contractile force (normalized to contractility prior to drug treatments) for single NIH/3T3 fibroblasts before and after US treatments. Cells were treated with Cytochalasin D (D), Blebbistatin (E), and Y-27632 (F) at t = -30 min. US stimulation was applied at t = 0 min. Data in D-F are shown as mean ± s.e.m. ($n \geq 4$).

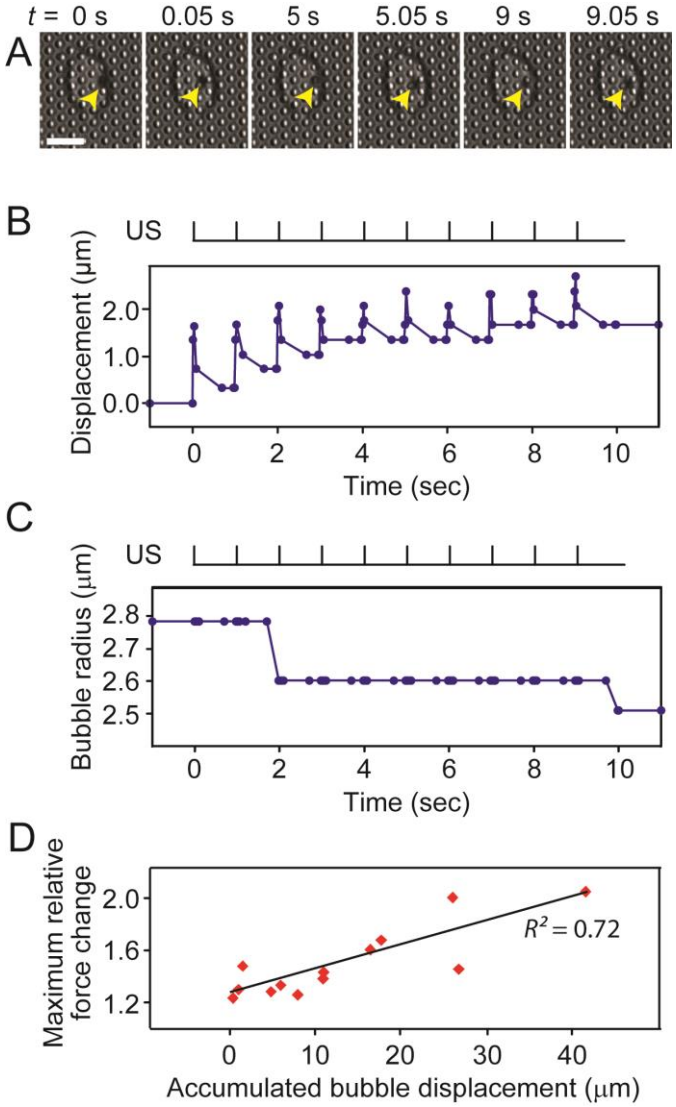

Figure 5-6 *In situ* microbubble activities induced by acoustic tweezing cytometry. (A) Time-lapse brightfield images showing one MB (arrow head) attached to a single NIH/3T3 fibroblast during 10 sec pulsed US stimulation. US was applied at t = 0 min, with a peak negative pressure amplitude of 0.05 MPa, PRF of 1 Hz, and duty cycle of 5%. Scale bars, 12 μm. (B) Translational displacement of MB during the 10 sec US stimulation. (C) Temporal evolution of MB radius during ultrasound application. (D) Positive correlation between the maximum relative cytoskeleton contractile force change 30 min after US treatments and the accumulated MB translational displacement (n = 13, and R^2 = 0.72).

5.3.6. Improving survival of disassociated human embryonic stem cells by mechanical stimulation using acoustic tweezing cytometry

So far we have demonstrated that ATC can apply mechanical forces to cells through MB-integrin linkage. As reviewed in the introduction section, the apoptosis of enzymatically disassociated single hESCs involves multiple mechanosensitive machineries including Rho/ROCK and myosin signals. Therefore, we specifically examined whether subcellular mechanical forces exerted by ATC might improve survival of disassociated single hESCs [39]. For ATC stimulation of hESCs, disassociated single hESCs were first seeded on tissue culture plates (TCPs) at a density of 10,000 cells cm^{-2} for 1 hr before incubated for 10 min with MBs (3×10^7 mL^{-1}) functionalized with Arg-Gly-Asp (RGD) peptides (RGD-MBs) using avidin-biotin conjugation chemistry to allow specific integrin binding. US pulses (center frequency 10 MHz, pulse duration 50 ms, pulse repetition frequency 10 Hz, acoustic pressure 0.08 MPa) were then applied to hESCs bound with RGD-MBs for 30 sec every hour for four consecutive hours (Figure 5-7b&c, supporting material).

Live cell imaging was performed using a synchronized high-speed camera to monitor dynamic changes of cell morphology and activities of MBs during and after ATC applications (Methods; Figure 5-7d). MBs exhibited robust reponses to repeated US pulses, including MB displacements due to the acoustic radiation forces (ARFs) [139] acting on MBs [39]. As expected, for negative controls without MBs and without US treatments (-US/-MB), most hESCs during cell seeding exhibited marked changes in cell morphology that included cell body contraction and membrane blebbing before undergoing apoptosis within 24 hrs after disassociation, resulting in a limited survival rate of 16.8% ± 3.1% (n = 5) (Figure 5-7e). Notably, for hESCs attached with RGD-MBs, ATC treatments elicited spreading of originally rounded hESCs and their adherence to TCPs. As a result, 67.0% ± 2.0% (n = 5) of such cells survived

within 24 hrs after disassociation (+US/+MB; Figure 5-7d&e). hESCs that spread before ATC treatments also survived for at least 24 hrs regardless of the presence of MBs or US treatment (Figure 5-7d), suggesting that cell spreading and adhesion might be critical for promoting hESC survival. Interestingly, US application alone (+US/-MB) or the presence of RGD-MBs alone (-US/+MB) had marginal but significant effect in enhancing hESC survival, resulting in a survival rate of 28.6% ± 2.2% (n = 5) for hESCs without MBs but treated with US (+US/-MB) (Figure 5-7e), and 35.7% ± 3.0% (n = 5) for hESCs with RGD-MBs but without US treatment (-US/+MB) (Figure 5-7e).

To investigate the role of integrin-mediated adhesion in hESC survival, we conducted experiments to apply ATC treatments to hESCs conjugated with MBs coated with acetylated low density lipoprotein (AcLDL; AcLDL-MBs), a ligand for transmembrane metabolic receptors that does not bind integrins. Under the same ATC treatments, survival rate of hESCs with AcLDL-MBs was unchanged compared to cells without MBs (-US/-MB and +US/-MB, Figure 5-7e), even though AcLDL-MBs exhibited significantly greater displacements than RGD-MBs (data not shown). These data suggested that integrin-mediated adhesion was required for improved hESC survival by acoustic actuation of integrin-anchored RGD-MBs.

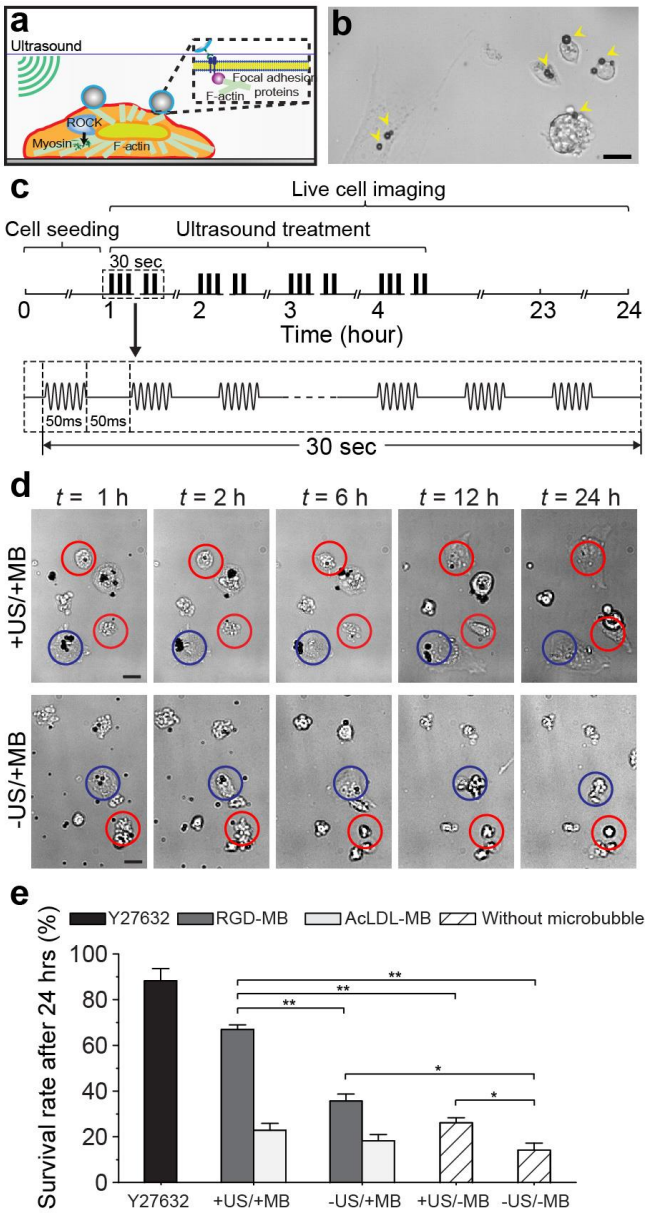

Figure 5-7 (a) ATC stimulation by acoustic excitation of microbubbles (MBs) attached to cells. (b) Bright filed image showing hESCs attached with MBs. Scale bar, 20 μm. (c) Illustration of ultrasound (US) protocol. (d) Live cell imaging showing hESCs exposed to ATC. Rounded hESCs were indicated in red circles with spread hESCs indicated in blue circles. Scale bar, 10 μm. (e) Survival rate of hESCs exposed to ATC treatments with RGD-MBs, AcLDL-MBs, and without MB. (n = 5, number of cells in each experiment > 200). Error bars, s.e.m. ** $p < 0.01$, * $p < 0.05$, Student's t-test.

To ascertain details of acoustic actuation of integrin-anchored MBs on hESCs, we divided originally rounded single hESCs into different sub-groups based on the initial number of RGD-MBs attached to each cell (Figure 5-8a). We examined hESC survival rate and corresponding MB displacements for each sub-group. hESCs with two or more RGD-MBs per cell exhibited significantly greater survival rate than cells with no or only one RGD-MB under ATC treatments (Figure 5-8b). The total accumulative RGD-MB displacement per cell for hESCs with two to four RGD-MBs was also significantly greater than that for hESCs with only one RGD-MB per cell (Figure 5-8c). It should be noted that the heightened total accumulative displacement of RGD-MBs was not only due to the greater number of RGD-MBs per cell, but also from the secondary ARF between MBs [139], which could efficiently displace MBs toward each other. For hESCs with three RGD-MBs per cell, the total accumulative MB displacement was similar to two-bubble cases (Figure 5-8c), as one of three MBs often exhibited a minimal movement due to balanced forces in the presence of multiple MBs and mutual interactions among them. Four-MB cases could be considered as a combination of one-, two-, three-MB cases with variations in the patterns of individual MB movements (Figure 5-8c). In addition, initially rounded hESCs bound with RGD-MBs and treated with ATC stimulations (+US/+MB) initiated their spreading about 5 hrs after cell seeding and became fully spread by 12 hrs (Figure 5-8d), significantly slower than conventional cell spreading processes [159]. Areas of hESCs without MBs (+US/-MB) or without US treatments (-US/+MB) remained unchanged during the first 24 hr after cell seeding (Figure 5-8d), corresponding to low survival rates for these groups.

To evaluate possible long-term effects of ATC treatment, we conducted alkaline phosphatase (ALP) assay to determine hESC cloning efficiency. Consistent with improved initial

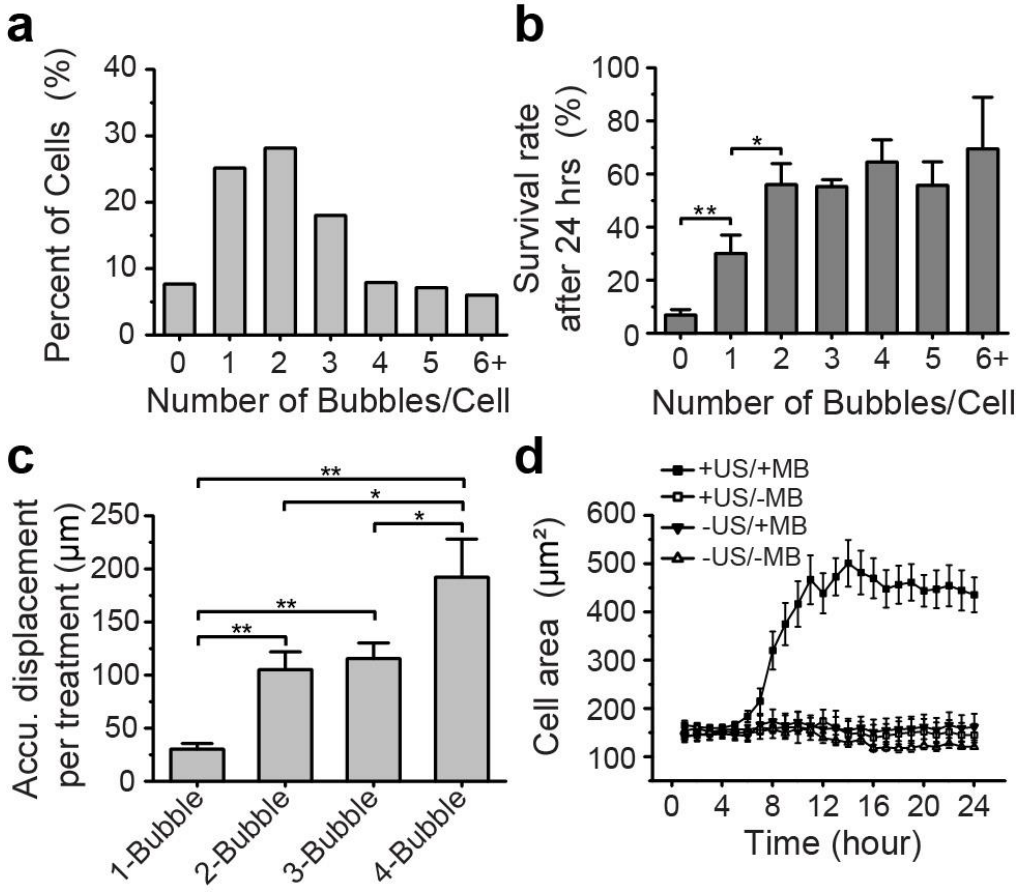

Figure 5-8 (a) Distribution of microbubbles (MBs) per cell (5 independent experiments, $n > 200$ cells for each). (b) Survival rate of hESCs with different initial numbers of RGD-MBs/cell. $n > 200$ cells for each experiment, $n > 20$ cells for each subgroup with different number of MBs per cell. Error bars, s.e.m. ** $p < 0.01$, * $p < 0.05$, Student's t-test. (c) Accumulative MB displacement per ATC treatment. Error bars, s.e.m. ** $p < 0.01$, * $p < 0.05$, Student's t-test. (d) Change of cell area for different subgroups.

survival rate, cloning efficiency of ATC-treated hESCs increased about 3-fold compared to untreated -US/-MB controls (Figure 5-9a&b), suggesting that the effect of ATC was mainly due to the improvement of initial survival of disassociated hESCs rather than cell proliferation or migration [160, 161]. ATC treatments did not adversely impact hESC stemness marker expression, as shown by positive immunostaining of pluripotency markers Oct4, Sox2, and E-cadherin 7 d after ATC treatments (Figure 5-9c).

5.4. Discussion

Our study demonstrates that ultrasound excitation of targeted microbubbles provides a robust strategy for biomechanical stimulation of mechano-sensitive and -responsive mammalian cells. The strong contractile response of NIH/3T3 fibroblasts as well as hMSCs to ultrasound excited microbubbles suggests that our ultrasound tweezing cytometry technique may have a great utility in regulating cellular behaviors.

Cells can sense mechanical stimuli and convert them into downstream intracellular biochemical signals, and such mechanotransduction process has profound impact in many physiological and pathological contexts. For example, endothelial cells respond to blood flow

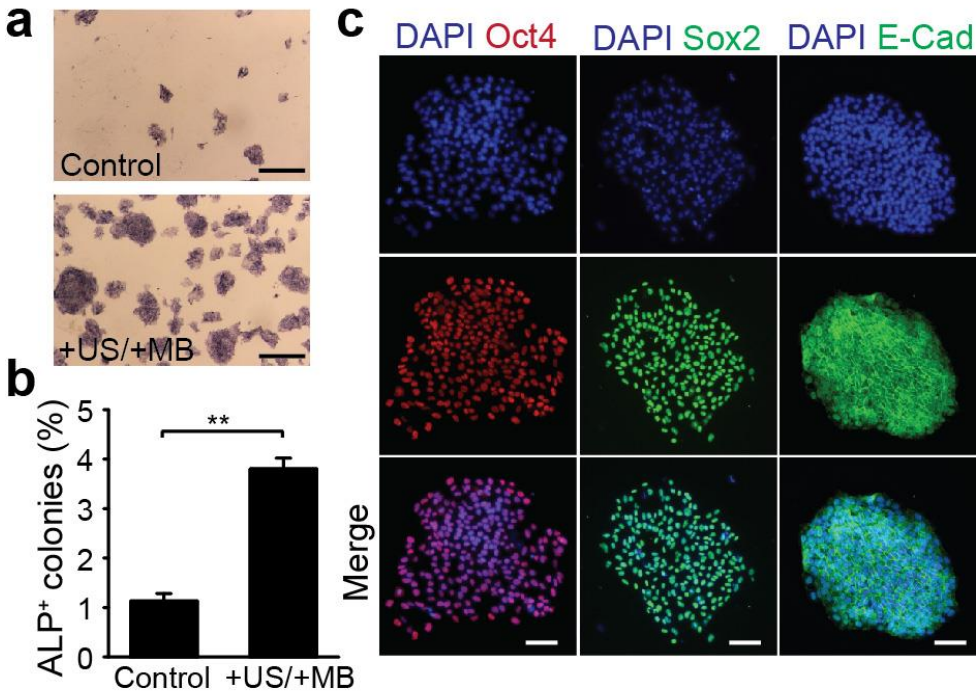

Figure 5-9 (a) Alkaline phosphatase (ALP) assay for dissociated hESCs with or without ATC treatments as indicated. Scale bar, 1 mm. (b) Relative ratio of ALP+ colonies to the number of hESCs initially seeded. (c) Immnuostaining with anti-Oct4, anti-Sox2, and anti-E-cadherin antibodies for hESC colonies 7 d after ATC treatments. Scale bar, 100 μm.

shear stress by regulating actin cytoskeleton structure [113]. Cytoskeleton contractility has also been implicated as a non-destructive live-cell predictor for hMSC differentiation [31]. Thus, the ultrasound tweezing cytometry methodology reported here can be effectively applied, in principle, to regulate biomechanical and cellular responses of different cell types.

Like magnetic and optical tweezers, our acoustic tweezing cytometry can generate controllable localized mechanical forces to single live mammalian cells. However, acoustic tweezing cytometry has several unique advantages. Unlike microbeads used in magnetic or optical tweezers, microbubbles provide a versatile multifunctional platform that can enable multifaceted applications. Microbubbles have been established as an effective imaging contrast agent for ultrasound imaging, [162-164] and they are also routinely used as drug carrier.[165, 166] Thus, the acoustic tweezing cytometry reported here has the potential for *in vivo* imaging guided manipulation of cellular contractility and thus downstream cellular effects. In addition, ultrasound excitation of targeted microbubbles is capable of intracellular delivery of drugs in a spatiotemporally controlled fashion, as we have previously demonstrated [130].

Thus, besides direct mechanical perturbation of cells, sonoporation can be seamlessly implemented and integrated in the same platform with acoustic tweezing cytometry to deliver membrane-impermeable drugs into cells for additional biochemical modulations of intracellular signaling. Many types of mammalian cells, either adherent in a monolayer or embedded in a three-dimensional matrix, can be treated simultaneously by ultrasound stimulation that can readily excite all microbubbles within the ultrasound field, providing a high-throughput cytometric assay on a large number of single cells with a subcellular precision. Further, by focusing ultrasound field to a local region or spatially patterning microbubbles [167], a selected group of cells within a monolayer or other multicellular configurations can be targeted for

biomechanical mmanipulations, thus enabling investigation of intercellular biomechanical interactions.

In this study, we developed a novel ultrasound tweezing cytometry utilizing ultrasound-excitable microbubbles targeted to cell membrane to apply spatiotemporally controlled subcellular mechanical forces to live single cells. By applying ultrasound pulses with appropriate amplitude and duration, functionalized lipid microbubbles attached to individual cells were actuated to exert subcellular mechanical forces in the pN - nN range to live single cells. Specifically, using NIH/3T3 fibroblasts and human mesenchymal stem cells (hMSCs) as mechanosensitive cell models, we showed that ultrasonic excitation of lipid microbubbles attached on cell membrane through integrin-mediated adhesions could elicit a rapid and sustained reactive intracellular cytoskeleton contractile force increase. Such ultrasound-mediated intracellular cytoskeleton contractility enhancement was dose-dependent and required an intact actin cytoskeleton structure as well as RhoA/ROCK signaling for intracellular transmission and conversion of mechanical signals. Our results demonstrated for the first time the potential of ultrasound tweezing cytometry technique using targeted microbubbles as an actuatable, biocompatible, and multifunctional agent for biomechanical stimulation of mechano-sensitive and -responsive cells. Compared to established methods for applying subcellular forces using solid microbeads (*i.e.*, optical and magnetic tweezers), ATC utilizes MBs that do not exhibit cellular internalization and can be easily removed from hESCs without leaving behind exogenous materials [168], providing a promising biocompatible platform for large-scale hESC culture.

Chapter 6

Conclusions and Future work

6.1. Summary of Thesis

6.1.1. Substrate mechanics regulate hPSCs fate

In this work, our results demonstrated that cytoskeleton contractility, focal adhesion formation, and E-cadherin expression were all critically involved in mechanoresponsive differentiation of hESCs [36]. Specifically, hESCs were mechanosensitive and increased their cytoskeleton contractility with matrix rigidity, and rigid substrates were supportive for maintenance of pluripotency of hESCs. Matrix mechanics-mediated cytoskeleton contractility might be functionally correlated to E-cadherin expressions in cell-cell contacts and involved in fate decisions of hESCs. Our results highlighted the important functional link between matrix rigidity, cellular mechanics, and pluripotency of hESCs. In addition, our micropost array system provided a novel approach to characterize and understand mechanotransduction and its involvement in hESC function. Mechanotransduction in hESCs is a largely unexplored area, and advancing understanding of mechanoresponsive behaviors of hESCs will help in the design of biologically inspired *in vitro* cellular microenvironments to guide growth, differentiation, and functional assembly of hESCs.

6.1.2. Hippo/YAP mediated rigidity dependent motor neuron differentiation

In this work, our studies suggest a putative multi-targeted mechanotransductive process in hPSCs where soft PMAs inhibit Smad phosphorylation while activating Lats, an actin-binding protein [169], during disassembly of actin microfilaments [37]. This in turn phosphorylates YAP to prevent nuclear translocation of phosphoSmads and inhibit subsequent activation of Smad target genes. The Hippo-YAP signaling pathway is highly conserved and under intense study given its importance in development and cancer. The current view implicates that cell polarity and adhesion proteins could regulate Hippo signaling . Our data reveal functional crosstalk between Hippo-YAP signaling and the classic mechanotransductive components, Rho GTPase and the actomyosin CSK. Other mechanosensory components, such as adhesion molecules including integrins and cadherins and cell morphology, may also regulate Hippo-YAP signaling in hPSCs. Supporting this view, increased internalization of integrins in mesenchymal stem cells on soft substrates represses Smad 1/5/8 phosphorylation and induces neurogenic differentiation [170]. Also, NIH/3T3 cell morphology regulates the Hippo pathway [88].

By combining dual Smad inhibition with PMAs, we generated high-yield and -purity functional MNs from hPSCs. PMAs are fully defined substrates that can be mass-produced for large-scale hPSC culture. We demonstrate that like many human adult stem cells [32, 171-174], hPSCs are intrinsically mechanosensitive and substrate rigidity is an *in vitro* extracellular switch that directs NE *vs.* NC lineage decisions and anterior *vs.* posterior patterning. Mechanical properties of the extracellular matrix *in vivo* may act as a "mechanical organizer" synergizing with morphogens to direct neural plate specification and anterior-posterior axis formation during neurulation.

6.1.3. Modeling neural plate development *in vitro*

In this work, we demonstrated that micropatterning hESCs can effectively recapitulate neural plate *in vitro* with proper biochemical conditions. Using this tool, we discovered that cell traction forces and cell shape, working upstream of Wnt and BMP signals, are important regulators of neural crest cell differentiation. Cell shape can regulate the activities of BMP but not Wnt signals. These results, together, suggest a novel mechanism in neural plate development. In addition to the BMP gradient, spontaneous contraction within neural plate induced a mechanical gradient (both stress and strain) radially, which serve as another mechanism to tightly control the lineage specification and regionalization of neural crest cells. This work highlight the importance and detailed mechanism of biomechanical cues in development.

6.1.4. Acoustic tweezing cytometry for stem cells and mechanobiology applications

In this work, we demonstrated for the first time that ultrasound excitation of targeted microbubbles could enable controlled application of subcellular biomechanical stimuli to live single cells [39]. Drug inhibition experiments demonstrated that intact actin cytoskeleton, myosin activity, and RhoA/ROCK signaling were all required for force sensing and transmission. We envision that the acoustic tweezing cytometry employing targeted microbubbles as a biocompatible and multifunctional agent can be further developed in the future as a powerful cell mechanics and mechanobiology tool to regulate cell function, gene expression, and stem cell differentiations both *in vitro* and *in vivo*.

Our data indicate that ATC stimulations improve the clonogenicity of disassociated hESCs by increasing their initial survival rate [40]. While the molecular mechanism underlying such mechanosensitive behavior of hESCs requires further study, our results suggest that

integrin-mediated adhesion formation and strengthening by ATC stimulations may facilitate spreading of disassociated hESCs, which in turn rescues the cells from hyper-activated actomyosin activities triggering downstream caspase-mediated apoptotic signaling pathways.

6.2. Future Research and Applications

6.2.1. Mechanobiology of hPSCs

Research in mechanobiology of hPSCs is still in its infancy; there are many important questions unanswered that require concerted and collaborative efforts from stem cell biologists and biomaterial scientists. I envision that mechanobiology of hPSCs will be under intense study in the coming years given its importance in development and for rational designs of synthetic culture systems for large-scale manufacturing of hPSCs and their functional derivatives (such as MNs for MN-related neurodegenerative diseases). Future studies will likely focus on identifying the role of dynamic biophysical cues on differentiation of hPSCs toward other lineages and subpopulations of progenitors and stem cells. Another critical research direction is to tease out detailed signaling pathways and regulatory networks that are responsible for relying biophysical signals from extracellular space to regulate gene expressions and fate control of hPSCs.

hPSCs offer great promise for developmental biology studies and cell replacement therapies. However, large-scale preclinical and clinical applications of hPSCs remain elusive owing to their unique sensitivity to the culture environment, which can be largely attributed to the poorly understood dynamic cell-ECM and cell-cell physical interactions of hPSCs. In addition, the puzzling mechano-sensitive and -responsive properties of hPSCs have just started to emerge, and our current understanding of the mechanotransductive systems in hPSCs is still very

limited. Thus, in my view, advancing understanding of how mechanobiology is involved in regulating hPSC behaviours will contribute significantly to improvements of large scale production of clinical grade hPSCs and their derivatives, a critical requirement for future hPSC applications.

Existing data suggests that the cytoskeleton structure and tension of hPSCs are very sensitive to the environmental cues and may be a critical controller of their survival, self-renewal, and lineage specification. RhoA/ROCK, myosin II, and E-cadherin seem to form a closely interconnected regulatory loop to control adhesion signaling and thus the survival and self-renewal of hPSCs. bFGF/MAPK, TGF-β/Activin/Nodal, BMP4 signalling in hPSCs are also regulated by mechanical stimuli, and they are central pathways controlling the self-renewal and differentiation programmes of hPSCs [25, 27]. Moreover, YAP/TAZ has been shown to transmit mechanical signals to nucleus through a Hippo independent pathway [87], and YAP/TAZ controls many critical downstream signals such as SMAD in hPSCs [175]. Collectively, discovering the hPSC mechanotransductive systems based on the cell-ECM and cell-cell interactions and their functional cross-talk during the self-renewal and differentiation processes of hPSCs will significantly improve our molecular understanding of the unique sensitivity of hPSCs to the culture environment during early embryogenesis and tissue development. It remains to be determined the relative importance of endogenous *vs.* exogenous cellular forces in regulating the mechano-sensitive and -responsive behaviours of hPSCs and how such force-mediated functional regulations for hPSCs are different in two-dimensional *vs.* three-dimensional culture environments [176]. These general but significant questions in mechanobiology of hPSCs remain to be answered in future studies.

Looking forward, I envision that innovative high-throughput, high-content approaches and tools integrating cellular biotechnology, materials science, microscale technology, mechanobiology, and advanced stem cell biology will be developed or adopted to characterize and understand the mechano-sensing and -transduction mechanisms and their involvements in regulation of hPSC self-renewal and differentiation. Due to the space limit, a detailed discussion of such high-throughput, high-content bioengineering and biointerfacial approaches and tools is not possible. The readers are referred to some excellent reviews elsewhere [177-179]. The ultimate functional goal for such research is to achieve the capability for predicting and ultimately controlling the integrated functional response of hPSCs. In the near future, these innovative tools, which can span different scales, from molecular (or subcellular) to cellular to organ levels, can allow us to generate dynamic and complex synthetic cellular microenvironments, with the molecular, structural, hydrodynamic, and mechanical cues well controlled in conjunction with their spatial and temporal levels and combinations, to regulate cell-ECM and cell-cell interactions of hPSCs. Miniaturized cell array methods based on these innovative techniques should also be developed to minimize reagent requirements. Such integrated cell-based high-throughput assays can be coupled with advanced biological tools to permit rapid, high-content, real-time monitoring of the effects of multiple mechanobiological stimuli on hPSC self-renewal and differentiation, speeding up the capacity for discovery of novel mechano-sensitive and -responsive behaviours of hPSCs.

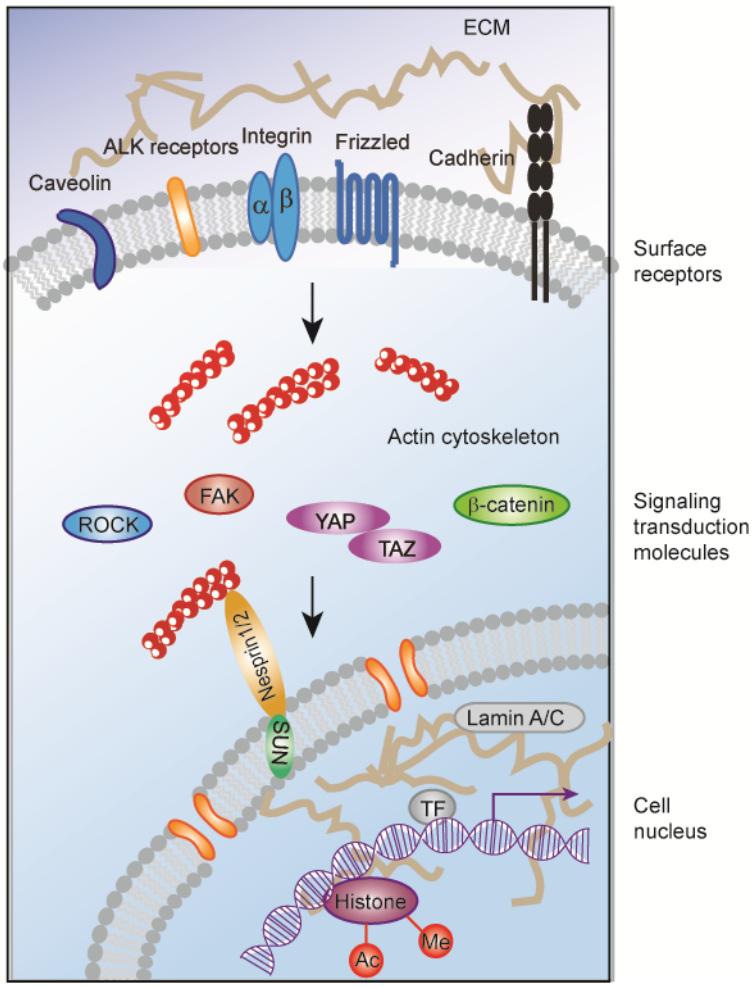

Figure 6-1 Mechanotransduction as a multi-targeted process. Cell surface receptors such as integrins, caveolin, ALK receptors, cadherins, and frizzled (Wnt receptors) are known to be mechanosensitive. Kinases such as Rho-associated protein kinase (ROCK) and focal adhesion kinase (FAK) and transcription factors such as YAP/TAZ and β-catenin can relay mechanical signals from cell surface to the nucleus. Remodeling of actin cytoskeleton can directly influence gene expression through nesprin, SUN proteins, and nuclear matrix protein Lamin A/C. Histone modification such as demethylation and deacetylation may also be regulated directly by biophysical cues in the cell microenvironment.

Detailed molecular mechanisms responsible for mechanosensitive behaviors of hPSCs are still elusive, and likely mechanotransduction of hPSCs requires cellular responses and regulations at multiple levels (genetic and epigenetic, transcriptional, and post-transcriptional including microRNA) and time scales (Figure 6-1). It has been demonstrated that cell surface receptors and adhesion molecules (*e.g.* integrins), intracellular signaling molecules (*e.g.* YAP

and RhoA/ROCK), nuclear components (*e.g.* SUN proteins and lamin A/C), and transcriptional factors (*e.g.* NF-κB and EGR1) all contribute to mechano-sensitivity and -responsibility of mammalian cells. Our mechanistic study also reveals a multi-targeted mechanotransductive process in hPSCs, in which soft substrates can simultaneously inhibit Smad 1/5/8 phosphorylation, lead to disassembly of actin microfilaments, and activate kinase Lats which in turn phosphorylates YAP to prevent nuclear translocation of phosphoSmads and inhibit subsequent activation of Smad target genes [180]. It is also worth noting that in a recent study by Downing *et al.*, the authors have discovered that patterned cell culture surfaces can lead to increased histone H3 acetylation and methylation by reducing histone deacetylase activity and up-regulation of the expression of WD repeat domain 5 (WDR5) - a subunit of H3 methyltranferase in fibroblasts during cell reprogramming, highlighting the effect of biophysical cues on directly modifying epigenetic status [181]. It is important to recognize mechanotransduction as an integrated cellular regulation process that can effectively drive hPSCs toward specific phenotypes with associated functions.

6.2.2. Modeling human development *in vitro* using stem cells

Micropatterning in two-dimension successfully recapitulates neural plate development. However, after gastrulation, embryo develops quickly into sophisticated three-dimensional structures with multiple cell types and complex geometry. Due to the unique advantages of using human materials to study developmental diseases, embryonic tissues and organ buds are valuable resources for regenerative medicine and drug screening applications. It is therefore a high-risk, high-pay off concept to reconstruct those tissues or organs *in vitro* using embryonic stem cells or diseases-specific induced pluripotent stem cells. For example, folding neural plate into neural tubes will help understand neural tube defect diseases and neural patterning dynamics. To

achieve that goal, one need to develop novel engineering tools to guide and facilitate the formation of such complex structures, either using embryonic stem cells or combining different types of cells. This strategy is different from current organ-on-chip techniques. While organ-on-chip strategies were proclaimed to be able to successfully recapitulate some physiological processes, the complexity of such system is still significantly lower than actual tissues/organs, limiting to co-culture of several types of cell lines with limited mechanical stimulations. Human stem cells-generated organoids are very comparable to human physiology but are difficult to generate and study. With the help of engineering tools, the generation of organoids can be facilitated and better controlled.

6.2.3. Mechanical stimulation of stem cells using ATC

Our research has demonstrated that ATC is a powerful tool to apply controllable forces to cells. The future research will focus on the application of this technology. The most attractive application of ATC is to use it *in vivo*, due to the unique advantage of microbubbles. Being able to stimulate microbubbles *in vivo* and in turn to control cell fate will open a new avenue in mechanical-based therapeutics [125, 182-184].

As a first step, it is critical to understand how mechanical stimulations using ATC regulate stem cell behaviors. It has been shown that subcellular mechanical forces can induce the loss of pluripotency in mouse embryonic stem cells and also, shear stresses can induce osteogenesis of mesenchymal stem cells. It will be interesting to explore the differentiation potential of embryonic or somatic stem cells under ATC stimulation.

Another important question that has not been answered by our current research is what the molecular mechanism of improved survival rate of single hESCs by ATC is. Although hyperactivation of myosin is found to be responsible for such disassociation-associated apoptosis,

our finding suggested that alternative mechanism may also contribute to the reestablish of new, and stable adhesion sites that facilitate the balance of excessive mechanical forces. The understanding of such novel mechanism will help find new ways to enable the large scale expansion of hPSCs, a requirement for future use of hPSCs in regenerative medicine.

6.3. Conclusion and Outlook

The mechanobiology field is quickly expanding over the past decade. The number of journal papers published per year in mechanobiology steadily increased from approximately 203 paper/year in 2004 to 694 paper/year in 2014 (data analyzed using Web of Science database). Mounting researchers from both bioengineering field and biology field start to appreciate the important role of biophysical cues in cell microenvironment and many important new findings result from close collaborations between engineers and biologists. My thesis research, together with those from others, unambiguously established that the self-renewal, differentiation and survival of hPSCs are mechanosensitive. Fine tuning the mechanical environment of hPSCs can effectively improve the large scale expansion and differentiation of hPSCs, a requirement for the stem cell-based regenerative medicine. My research established a novel mechanistic framework centering on Hippo/YAP signaling for understanding mechanosensitive hPSC behaviors. I proposed a multi-targeted mechanotransductive process involving surface receptors (e.g., integrins, R-Smad receptors, etc.), transcriptional co-activators (YAP/TAZ), Rho GTPase, E-cadherin, and actomyosin cytoskeleton. These signaling molecules, together with mechanical forces, interplay with each other and form a robust feedback network that instruct the proliferation, differentiation and patterning of hPSCs.

Despite of its rapid growth, the mechanobiology field is still in its infancy. I envision that the opportunities of mechanobiology lie in the following areas. It is of utmost importance to tease out the detailed genetic, epigenetic and biochemical mechanism of mechanotransduction. Although many mechanosensitive molecules have been identified, their interactions with mechanical stimulation and crosstalk with other major signaling pathways are still elusive. It is still unclear why different cell types show drastically different responses to similar mechanical stimulations. In addition to single cell behaviors, it is also important to understand how mechanical stimulations regulate collective cell behaviors. Therefore, engineers need to work more closely with biologists to discover new phenomenon and more importantly, new biology.

From the engineering side, there are still many theoretical and experimental works need to be done to clarify the mechanical environment of cells. Most current mechanobiology studies are using static, elastic, continuous, and two-dimensional culture conditions while in reality, cells are in a dynamic, viscoelastic, fibrillary, and three-dimensional environment. With advances in materials science and mechanics, several recent studies started to tackle these challenges and discovered interesting new findings which improve our current understanding of mechanobiology [185-187]. Thus, engineers need to refine current tools and develop novel tools to recapitulate such complex cellular microenvironment for fundamental studies.

To boost the impact of mechanobiology research, a critical step is to find out novel therapeutic applications. One way to do that is by developing drugs targeting some downstream effectors of mechanotransduction pathway, which might be underappreciated previously. Another possibility is to develop injectable biomaterials to guide stem cell behaviors *in vivo*, as has been shown by Mooney's group [72, 188]. Some recent evidence suggests that it is even possible to engineer the cells *in vitro* before transplantation due to the mechanical memory effect

[189]. With a more comprehensive understanding of mechanobiology, I envision that novel therapeutic approaches targeting mechanosensitive components will be available in the near future.

Appendix A

Maintenance and neural differentiation of hPSCs

A.1 Culture medium conditions

Growth media contained DMEM/F12 (GIBCO), 20% KnockOut serum replacement (GIBCO), 0.1 mM β-mercaptoethanol (GIBCO), 2 mM glutamax (GIBCO), 1% non-essential amino acids (GIBCO), and 4 ng mL^{-1} human recombinant basic fibroblast growth factor (bFGF; GlobalStem).

Neural induction media: Growth media were used as neural induction media from day 1 to day 3. N2 media containing DMEM/F12, 1% N2 supplement (GIBCO), 2 mM glutamax, and 1% non-essential amino acid were used to gradually replace growth media from day 4 as following: 25% N2 media and 75% growth media at day 4, 50% N2 media and 50% growth media at day 5 and 6, 75% N2 media and 25% growth media at day 7, 100% N2 media at day 8. To promote neural induction, TGF-β inhibitor SB 431542 (10 μM; Cayman Chemical) and BMP4 inhibitor LDN 193189 (0.1 μM, unless stated otherwise; Selleckchem) were added into neural induction media from day 1.

Motor neuron (MN) differentiation media contained N2 media supplemented with 1 μM retinoic acid (RA; Cayman Chemical), 1 μM purmorphamine (Pur; Cayman Chemical), and 20 ng mL^{-1} bFGF.

Motor neuron (MN) maturation media contained basal media that was a 1:1 mixture of N2 and B-27 media. B-27 media contained neurobasal media (GIBCO), 2% B-27 supplement (GIBCO), and 2 mM Glutamax. The following chemicals were added to basal media freshly before each medium change: 10 ng mL^{-1} brain-derived neurotrophic factor (BDNF; R&D systems), 10 ng mL^{-1} insulin-like growth factor 1 (IGF-1; Peprotech), 1 µM cyclic adenosine monophosphate (cAMP; Sigma), 0.2 µg mL^{-1} ascorbic acid (Sigma), 0.1 µM RA, and 1 µM Pur.

All the media were pre-equilibrated at 37^{o}C in 5% CO_2 before use.

A.2 Cell culture and differentiation

hESC line H1 (WiCell) or H9 (WiCell) was cultured on mitotically inactive mouse embryonic fibroblasts (MEFs; GlobalStem) in growth media with daily medium change. Cells were passaged every 5 d using the STEMPRO EZPassage Disposable Stem Cell Passaging Tool (Invitrogen). Before passaging, differentiated cells were removed manually using a modified pasteur pipette under a stereomicroscope (Olympus). Cells were rinsed briefly with PBS and treated with TrypLE Select (Invitrogen) for 2 min to release MEFs. Cells were rinsed briefly again with PBS before all cells, including hESCs and remaining MEFs, were collected using a cell scraper (BD Biosciences). To remove contaminant MEFs, all cells were transferred onto a 60-mm tissue culture dish (BD Biosciences) coated with gelatin (Sigma) and incubated for 45 min. MEFs would attach to the dish while hESCs were still in the supernatant. hESCs in the supernatant were collected and centrifuged with the cell pellet re-dispersed in growth media containing Y27632 (10 µM; Enzo Life Sciences).

Both hESC line CHB-10 (Children's Hospital Corp., Boston, MA) and hiPSC line were cultured on poly[2-(methacryloyloxy)ethyl dimethyl-(3-sulfopropyl)ammonium hydroxide] (PMEDSAH) in human cell conditioned media (GlobalStem) as described previously[55], before seeded onto the PMA by digesting in TrypLE Select. The hiPSC line was derived from human foreskin fibroblasts by over-expression of *Oct4*, *Sox2*, *Klf4*, and *c-Myc* using the Sendai virus constructs (Invitrogen).

When cell passaging was needed for neuroepithelial cells (NEs), cells were first cut into small cell aggregates using the STEMPRO EZPassage Disposable Stem Cell Passaging Tool or dispase (STEMCELL Technologies) before transferred onto new substrates *en bloc*.

Appendix B

Fabrication of PDMS micropost arrays

B.1 Fabrication of the PDMS micropost array

B.1.1 Silicon mold fabrication

1. Photoresist Patterning

a) Spin coat 3 μm SPR220 photoresist and softbake at 110°C for 3min, manually or using ACS 200 cluster tool.

b) Expose the photoresist using GCA AS200 AutoStep Aligner.

c) Develop the exposed photoresist using AZ 300 Developer for 30s, manually or using ACS 200 cluster tool.

2. Plasma Etching

Etch silicon using deep reactive ion etching, DRIE (Deep Silicon Etcher, STS; Etch rate ~ 5μm/min). The height of the silicon micropost was modulated by controlling the DRIE etch time.

3. Silicon Surface Silanization

a) O2 Plasma activate the Silicon mold surface for 2 min (Plasma Cleaner PDC-001, Harrick Plasma: O2, 80W, 250 mT, 5min), right before silanization.

b) Silanize the Silicon mold using 100μl of Silane (tridecafluoro- 1, 1, 2, 2,-

tetrahydrooctyl)-1-trichlorosilane (United Chemical Technologies) for 4 hr under vacuum to facilitate subsequent release of the negative PDMS mold.

B.1.2 PDMS negative mold fabrication

1:10 (w/w, curing agent: base monomer) ratio PDMS prepolymer (Sylgard 184, Dow-Corning, Midland, MI) was poured over the silicon micropost master and cured at 110°C for 20 min. The negative PDMS mold was then generated by peeling off from the silicon master, oxidized with the oxygen plasma for 1 min (200 mTorr; Plasma Prep II, West Chester, PA), and silanization with (tridecafluoro-1,1,2,2,-tetrahydrooctyl)-1-trichlorosilane for 24 hrs to obtain the PDMS negative mold. To generate the final PDMS micropost array, 1:10 ratio PDMS prepolymer was poured over the negative PDMS mold and degassed under vacuum for 10 min. Then a clean 25 cm × 25 cm cover glass was placed on top of the negative mold and the whole assembly was cured at 110°C for 40 hrs. The negative mold was then peeled off to release the final PDMS micropost array. The collapsed PDMS microposts during peeling off was rescued by sonication in 100% ethanol for 30 sec followed by dry-release with liquid CO_2 using a critical point dryer (Samdri®-PVT-3D, Tousimis, Rockville, MD).

B.2 Surface functionalization of the PDMS micropost array

The top surface of the PDMS micropost array was functionalized with human recombinant vitronectin (R&D system, Minneapolis, MN) to promote adhesion of hESCs. Briefly, a flat 1:30 PDMS stamp was soaked with vitronectin at a concentration of 20 $\mu g\ mL^{-1}$ in distilled water for 1 hr at room temperature. The PDMS stamp was then thoroughly rinsed with distilled water and blown dry with a stream of nitrogen. In parallel, the PDMS micropost array

was treated with ozone generated by a UV-ozone cleaner (Jelight, Irvine, CA) for 7 min to activate the surface of the PDMS micropost array, so that the hydroxyl group generated during this process on the PDMS surface could covalently bond to vitronectin. The PDMS stamp was then placed in conformal contact with the PDMS micropost array for about 10 sec. To prevent non-specific protein absorption to the non-functionalized surface of the PDMS micropost array, the PDMS micropost array was soaked in pluronics F127 NF dissolved in PBS (0.2%, w/v; BASF, Ludwigshafen, Germany) for 30 min. For the PDMS micropost array used for traction force measurement, an additional labeling step was performed by soaking the PDMS micropost array with 1,1'-dioctadecyl-3,3,3',3'-tetramethylindodicarbocyanine perchlorate ('DiD' oil; Invitrogen, Carlsbad, CA) before the treatment with the pluronics F 127 NF.

B.3 Cell culture and seeding cells on the PDMS micropost array

hESCs (H9 and H1, obtained from WiCell, Madison, WI) were cultured on a feeder-free synthetic polymer coating (PMEDSAH) [55, 56] with the Human-Cell-Conditioned Medium (GlobalStem, Rockville, MD) supplemented with 8 ng/mL of human recombinant basic fibroblast growth factor (bFGF; Globalstem). Before plating cells, differentiated cells were removed manually by a modified pasteur pipette under a stereomicroscope (Leica MZ9.5, Leica Microsystems Inc., Buffalo Grove, IL). Then, undifferentiated colonies were collected as small cell aggregates using the STEMPRO EZPassage Disposable Stem Cell Passaging Tool (Invitrogen) in a 1.5 mL centrifuge tube. After centrifugation and a brief washing with PBS, the cell aggregates were treated with 0.5 mL 0.25% Trypsin-EDTA for 1 min. 1 mL 10% fetal bovine serum (FBS, Invitrogen) was used to stop trypsinization and was followed by an immediate centrifugation. The cell pellet was then dispersed in the StemPro serum free medium

(Invitrogen) supplied with 8 ng/mL bFGF and Y27632 (a ROCK inhibitor) at 10 μM and passed through a cell strainer with the 40 μm nylon mesh (BD Biosciences, Bedford, MA) to remove large cell aggregates. The obtained single hESCs were counted and then seeded on the PDMS micropost array at a desired density.

Appendix C

Traction force measurement

C1. Cell seeding

The cover glass holding the PDMS micropost array was attached to a 35 mm dish with a 20 mm hole at the center (Glass-bottom-dishes, MatTek, Ashland, MA). Cells were plated at low density (~ 5,000 cells/cm^2) for single cell traction force measurement.

Labelling PDMS micropost arrays with DiI will stain both the top and the side of the microposts, which may compromise the image analysis. To avoid this issue, fluorescent labelled ECM proteins, such as Alexa Fluor® 647 Conjugate fibrinogen can be mixed with desired ECM proteins to label exclusively the top of the microposts.

C.2 Live cell imaging

Live-cell images were obtained using a 40× objective (1.3 NA, oil immersion; EC Plan NEOFLUAR; Carl Zeiss MicroImaging, Thornwood, NY) on a Zeiss Observer.Z1 microscope equipped with a thermoelectrically-cooled monochrome CCD camera (AxioCam HRM, Carl Zeiss MicroImaging). The microscope was further equipped with an environmental chamber to maintain the experimental environment at 37°C. A microscope stage incubator (Carl Zeiss

MicroImaging) was also used to maintain 5% CO_2. A phase image and a fluorescent images were taken at the same position.

C3. Data analysis

The positions of single hESCs were recorded by the AxioVision software (Carl Zeiss MicroImaging). A custom-developed MATLAB program (details of the program was described in Ref. [54]; The MathWorks, Natick, MA) was used to calculate deflection of the PDMS micropost centroid from its unbent, unloaded position, which was then converted to the horizontal traction force by multiplying with the nominal spring constant *K* of the PDMS micropost.

Appendix D

Cell stretching assay

D1. Silicon mold fabrication

1. Photoresist Patterning

a) Spin coat 3 μm SPR220 photoresist and softbake at 110°C for 3min, manually or using ACS 200 cluster tool.

b) Expose the photoresist using GCA AS200 AutoStep Aligner.

c) Develop the exposed photoresist using AZ 300 Developer for 30s, manually or using ACS 200 cluster tool.

2. Plasma Etching

Etch silicon using deep reactive ion etching, DRIE (Deep Silicon Etcher, STS; Etch rate ~ 5μm/min).

3. Silicon Surface Silanization

a) O2 Plasma activate the Silicon mold surface for 2 min (Plasma Cleaner PDC-001, Harrick Plasma: O2, 80W, 250 mT, 5min), right before silanization.

b) Silanize the Silicon mold using 100μl of Silane (tridecafluoro- 1, 1, 2, 2,-tetrahydrooctyl)-1-trichlorosilane (United Chemical Technologies) for 4 hr under vacuum to facilitate subsequent release of the negative PDMS mold.

D2. Device assembly

1. **Fabricating PDMS membrane**
    a) PDMS were spin coated on the mold (500 rpm, 90s) to generate a thin PDMS film and were cured at 110 ^{o}C for 20 mins.
    b) The PDMS film was then peeled off and bonded to a coverglass through plasma bonding.
    c) A block PDMS, with a through hole punched, was bonded to the top of the membrane through plasma bonding. High bonding strength is desirable to avoid leaking.
2. **Calibration**
    a) A negative mold of PDMS micropost array was coated with Alexa Fluor 488 conjugated BSA and stamped on the device.
    b) Under the fluorescent microscope, post center to center distance was measured with or without pressure supply.

D3. Cell stretching

Distill water was then filled into the channels and chambers and a pressure regulator connected to a compress air outlet was used to apply pressure to deform the PDMS thin film. The device was then transferred into an incubator to culture for 24 hrs. Longer culture up to 48 hrs can also be achieved. To induce 100% increase in cell projection area, the pressure used was 30 Psi.

To release the streching after 24 hr stretching, the pressure was reduced gradually within an hour to avoid cell detachment after a sudden pressure release.

Appendix E

General cell biology assays

E.1 Immunocytochemistry

Cells were fixed with 4% paraformaldehyde (Electron Microscopy Sciences) for 15 min and then permeabilized with 0.1% Triton X-100 (Roche Applied Science) for 20 min at room temperature. Primary antibodies (listed in **Supplementary Table 2**) were used and detected by goat-anti mouse Alexa Fluor 488 and/or goat-anti rabbit Alexa Fluor 546 secondary antibodies, except for ChAT staining, which was detected using FITC conjugated bovine-anti goat secondary antibody (Santa-Cruz Biotechnology). Alexa Fluor 555 conjugated phalloidin (Invitrogen) was used for visualization of actin microfilaments. Percentage of marker-positive cells was quantified with a custom-developed MATLAB program (MathWorks) based on a watershed segregation algorithm.

E.2 RNA isolation and quantitative real-time PCR (qRT-PCR) analysis

Total RNA was isolated from cells using TRIzol (Invitrogen) or RNeasy kit (Qiagen). Real-time PCR (RT-PCR) was performed and monitored using an ABI 7300 system (Applied Biosystems). Quantitative real-time PCR (qRT-PCR) was also performed with either Taqman-probes (for gene expression analysis) or SYBR Green PCR mastermix (for siRNA knockdown). Human GAPDH or 18S primers were used as an endogenous control for relative quantifications. Samples in which no expression was detected were given an arbitrary Ct value of 40. All

analyses were performed with three replicates. Relative expression levels were determined by calculating $2^{-\Delta\Delta Ct}$ with the corresponding s.e.m.

E.3 Western blotting

Whole cell lysates were prepared from cells, separated on SDS-polyacrylamide gel, and transferred to PVDF membranes. NE-PER nuclear and cytoplasmic extraction kit (Thermo Scientific) was used to obtain cytoplasmic and nuclear protein fractions. PVDF membranes were incubated with blocking buffer (Li-Cor) for 1 hr and then incubated with primary antibodies overnight at 4^{o}C. Blots were then incubated with IRDye secondary antibodies (Li-Cor) for 1 hr before protein expression was detected with a Li-Cor Odyssey Sa Infrared Imaging System (Li-Cor).

E.4 siRNA knockdown

hESCs cultured on vitronectin coated 6-well plates were transfected using DharmaFECT 1 (Thermo Scientific). Briefly, cells were plated at 80% confluence and subjected to transfection the next day (or day 0) using 25 nM final concentration of siRNA. After 24 hrs, transfected cells were passaged onto the PMA for downstream assays. Two additional siRNA treatments were performed at day 2 and 4. siRNA including Lats1 and scramble control (SMARTpool) was purchased from Dharmacon.

E.5 Scanning electron microscopy (SEM)

Samples for scanning electron microscopy were washed 3 times with 50 mM Na-cacodylate buffer (pH 7.3; Sigma-Aldrich), fixed for 1 hr with 2% glutaraldehyde (Electron

Microscopy Science) in 50 mM Na-cacodylate buffer, and dehydrated in a graded series of ethanol concentrations through 100% over a period of 1.5 hr. Dehydration in 100% ethanol was performed 3 times. After washing with 100% ethanol, dehydrated samples were dried with liquid CO_2 using a super critical point dryer (Samdri-PVT-3D; Tousimis). Samples were then mounted on stubs, sputtered with gold palladium, observed, and photographed under a Hitachi SU8000 ultra-high resolution SEM machine (Hitachi High Technologies America).

E.6 Whole-cell patch clamp recording

Whole-cell current clamp was performed for functional MNs derived from hESCs using pipette electrodes (resistance 3 - 5 MΩ) filled with the following: 140 mM K-gluconate, 4 mM NaCl, 1 mM EGTA, 2 mM $MgCl_2$, 0.39 mM $CaCl_2$, 2 mM ATP, 0.3 mM GTP and 20 mM Hepes (pH 7.2; free $[Ca^{2+}]_i \sim 100$ nM). The standard extracellular (bath) solution (modified Tyrode's solution) contained: 153 mM NaCl, 5 mM KCl, 2 mM $CaCl_2$, 1 mM $MgCl_2$, 20 mM Hepes, and 10 mM glucose (pH 7.4). Signals were amplified using an Axopatch 2A patch clamp amplifier, digitized with Digidata 1440 at 10 kHz, filtered at 2 kHz, and recorded with Clampex 10.3 acquisition system (Axon instruments). All experiments were conducted at room temperature, and all recordings were analyzed with pClamp 10.3 and Origin 8.0 (OriginLab). As described previously[73], only cells with stable resting membrane potentials < -50 mV were considered to be healthy and used for further recording. Spontaneous action potentials (APs) were recorded without current stimulus. Amplitude of APs was determined by averaging at least 20 APs. The instantaneous frequency change or spike frequency adaptation (SFA) and post-inhibitory rebound (PIR) AP were examined by injecting a depolarizing or hyperpolarizing current pulse, respectively.

Reference

[1] Sun Y, Chen CS, Fu J. Forcing stem cells to behave: a biophysical perspective of the cellular microenvironment. Annual Review of Biophysics. 2012;41:519-42.
[2] Sun Y, Fu J. Mechanobiology: a new frontier for human pluripotent stem cells. Integrative Biology. 2013;5:450-7.
[3] Daley GQ, Scadden DT. Prospects for stem cell-based therapy. Cell. 2008;132:544-8.
[4] Lindvall O, Kokaia Z. Stem cells for the treatment of neurological disorders. Nature. 2006;441:1094-6.
[5] Laflamme MA, Murry CE. Heart regeneration. Nature. 2011;473:326-35.
[6] Moustakas A, Heldin C-H. Non-Smad TGF-β signals. Journal of Cell Science. 2005;118:3573-84.
[7] Jones DL, Wagers AJ. No place like home: anatomy and function of the stem cell niche. Nat Rev Mol Cell Biol. 2008;9:11-21.
[8] Johnston LA. Competitive interactions between cells: death, growth, and geography. Science. 2009;324:1679-82.
[9] Morrison SJ, Spradling AC. Stem cells and niches: mechanisms that promote stem cell maintenance throughout life. Cell. 2008;132:598-611.
[10] Jones DL, Wagers AJ. No place like home: anatomy and function of the stem cell niche. Nature Reviews Molecular Cell Biology. 2008;9:11-21.
[11] Scadden DT. The stem-cell niche as an entity of action. Nature. 2006;441:1075-9.
[12] Fuchs E, Tumbar T, Guasch G. Socializing with the neighbors: stem cells and their niche. Cell. 2004;116:769-78.
[13] Li D, Zhou J, Chowdhury F, Cheng J, Wang N, Wang F. Role of mechanical factors in fate decisions of stem cells. Regenerative Medicine. 2011;6:229-40.
[14] Guilak F, Cohen DM, Estes BT, Gimble JM, Liedtke W, Chen CS. Control of stem cell fate by physical interactions with the extracellular matrix. Cell Stem Cell. 2009;5:17-26.
[15] Discher DE, Mooney DJ, Zandstra PW. Growth factors, matrices, and forces combine and control stem cells. Science. 2009;324:1673-7.
[16] Wang JHC, Thampatty BP. Mechanobiology of adult and stem cells. International Review of Cell and Molecular Biology. 2008;271:301-46.
[17] Cohen DM, Chen CS. Mechanical control of stem cell differentiation. StemBook: The Stem Cell Research Community; 2008.
[18] Hoffman BD, Grashoff C, Schwartz MA. Dynamic molecular processes mediate cellular mechanotransduction. Nature. 2011;475:316-23.
[19] Wang N, Tytell JD, Ingber DE. Mechanotransduction at a distance: mechanically coupling the extracellular matrix with the nucleus. Nature Review Molecular Cell Biology. 2009;10:75-82.
[20] Geiger B, Spatz JP, Bershadsky AD. Environmental sensing through focal adhesions. Nature Reviews Molecular Cell Biology. 2009;10:21-33.
[21] Chen CS. Mechanotransduction - a field pulling together? Journal of Cell Science. 2008;121:3285-92.
[22] Peyton S, Ghajar C, Khatiwala C, Putnam A. The emergence of ECM mechanics and cytoskeletal tension as important regulators of cell function. Cell Biochemistry and Biophysics. 2007;47:300-20.
[23] Vogel V, Sheetz M. Local force and geometry sensing regulate cell functions. Nature Reviews Molecular Cell Biology. 2006;7:265-75.
[24] Orr AW, Helmke BP, Blackman BR, Schwartz MA. Mechanisms of mechanotransduction. Developmental Cell. 2006;10:11-20.
[25] Xu RH, Peck RM, Li DS, Feng X, Ludwig T, Thomson JA. Basic FGF and suppression of BMP signaling sustain undifferentiated proliferation of human ES cells. Nat Meth. 2005;2:185-90.

[26] Dravid G, Ye Z, Hammond H, Chen G, Pyle A, Donovan P, et al. Defining the role of Wnt/beta-catenin signaling in the survival, proliferation, and self-renewal of human embryonic stem cells. Stem Cells. 2005;23:1489-501.
[27] James D, Levine AJ, Besser D, Hemmati-Brivanlou A. TGFβ/activin/nodal signaling is necessary for the maintenance of pluripotency in human embryonic stem cells. Development. 2005;132:1273-82.
[28] Li J, Wang G, Wang C, Zhao Y, Zhang H, Tan Z, et al. MEK/ERK signaling contributes to the maintenance of human embryonic stem cell self-renewal. Differentiation. 2007;75:299-307.
[29] Peerani R, Rao BM, Bauwens C, Yin T, Wood GA, Nagy A, et al. Niche-mediated control of human embryonic stem cell self-renewal and differentiation. Embo J. 2007;26:4744-55.
[30] Holst J, Watson S, Lord MS, Eamegdool SS, Bax DV, Nivison-Smith LB, et al. Substrate elasticity provides mechanical signals for the expansion of hemopoietic stem and progenitor cells. Nature Biotechnology. 2010;28:1123-8.
[31] Fu JP, Wang YK, Yang MT, Desai RA, Yu XA, Liu ZJ, et al. Mechanical regulation of cell function with geometrically modulated elastomeric substrates. Nat Meth. 2010;7:733-6.
[32] Gilbert PM, Havenstrite KL, Magnusson KEG, Sacco A, Leonardi NA, Kraft P, et al. Substrate elasticity regulates skeletal muscle stem cell self-renewal in culture. Science. 2010;329:1078-81.
[33] Keung AJ, de Juan-Pardo EM, Schaffer DV, Kumar S. Rho GTPases Mediate the Mechanosensitive Lineage Commitment of Neural Stem Cells. Stem Cells. 2011;29:1886-97.
[34] Discher DE, Janmey P, Wang Y-l. Tissue cells feel and respond to the stiffness of their substrate. Science. 2005;310:1139-43.
[35] Sun Y, Villa-Diaz L, Lam HWR, Chen W, Krebsbach P, Fu J. Micromechanical elastomeric devices for investigations of mechanobiology in human embryonic stem cells. Proceedings of 16th International Conference on Miniaturized Systems for Chemistry and Life Sciences (μTAS 2012). Okinawa, Japan2012. p. In press.
[36] Sun Y, Villa-Diaz LG, Lam RH, Chen W, Krebsbach PH, Fu J. Mechanics regulates fate decisions of human embryonic stem cells. Plos One. 2012;7:e37178.
[37] Sun Y, Yong KM, Villa-Diaz LG, Zhang X, Chen W, Philson R, et al. Hippo/YAP-mediated rigidity-dependent motor neuron differentiation of human pluripotent stem cells. Nat Mater. 2014;13:599-604.
[38] Sun Y, Fu J. Harnessing mechanobiology of human pluripotent stem cells for regenerative medicine. ACS chemical neuroscience. 2014;5:621-3.
[39] Fan Z, Sun Y, Di C, Tay D, Chen W, Deng CX, et al. Acoustic tweezing cytometry for live-cell subcellular modulation of intracellular cytoskeleton contractility. Sci Rep. 2013;3:2176.
[40] Chen D, Sun Y, Deng Cheri X, Fu J. Improving Survival of Disassociated Human Embryonic Stem Cells by Mechanical Stimulation Using Acoustic Tweezing Cytometry. Biophys J. 2015;108:1315-7.
[41] Chen D, Sun Y, Gudur Madhu SR, Hsiao Y-S, Wu Z, Fu J, et al. Two-Bubble Acoustic Tweezing Cytometry for Biomechanical Probing and Stimulation of Cells. Biophys J. 2015;108:32-42.
[42] Saha S, Ji L, de Pablo JJ, Palecek SP. Inhibition of human embryonic stem cell differentiation by mechanical strain. Journal of Cellular Physiology. 2006;206:126-37.
[43] Saha S, Ji L, de Pablo JJ, Palecek SP. TGF β/Activin/Nodal pathway in inhibition of human embryonic stem cell differentiation by mechanical strain. Biophys J. 2008;94:4123-33.
[44] Chowdhury F, Na S, Li D, Poh YC, Tanaka TS, Wang F, et al. Material properties of the cell dictate stress-induced spreading and differentiation in embryonic stem cells. Nat Mater. 2010;9:82-8.
[45] Engler AJ, Sen S, Sweeney HL, Discher DE. Matrix elasticity directs stem cell lineage specification. Cell. 2006;126:677-89.
[46] Evans ND, Minelli C, Gentleman E, LaPointe V, Patankar SN, Kallivretaki M, et al. Substrate stiffness affects early differentiation events in embryonic stem cells. European Cells & Materials. 2009;18:1-13; discussion -4.
[47] Chowdhury F, Li Y, Poh Y-C, Yokohama-Tamaki T, Wang N, Tanaka TS. Soft substrates promote homogeneous self-renewal of embryonic stem cells via downregulating cell-matrix tractions. Plos One. 2010;5:e15655.

[48] Sun YB, Villa-Diaz LG, Lam RHW, Chen WQ, Krebsbach PH, Fu JP. Mechanics Regulates Fate Decisions of Human Embryonic Stem Cells. Plos One. 2012;7.
[49] Keung AJ, Asuri P, Kumar S, Schaffer DV. Soft microenvironments promote the early neurogenic differentiation but not self-renewal of human pluripotent stem cells. Integrative Biology. 2012;4:1049-58.
[50] Musah S, Morin SA, Wrighton PJ, Zwick DB, Jin S, Kiessling LL. Glycosaminoglycan-Binding Hydrogels Enable Mechanical Control of Human Pluripotent Stem Cell Self-Renewal. ACS Nano. 2012.
[51] Klim JR, Li LY, Wrighton PJ, Piekarczyk MS, Kiessling LL. A defined glycosaminoglycan-binding substratum for human pluripotent stem cells. Nat Meth. 2010;7:989-U72.
[52] Trappmann B, Gautrot JE, Connelly JT, Strange DG, Li Y, Oyen ML, et al. Extracellular-matrix tethering regulates stem-cell fate. Nat Mater. 2012;11:642-9.
[53] Mei Y, Saha K, Bogatyrev SR, Yang J, Hook AL, Kalcioglu ZI, et al. Combinatorial development of biomaterials for clonal growth of human pluripotent stem cells. Nat Mater. 2010;9:768-78.
[54] Yang MT, Fu J, Wang Y-K, Desai RA, Chen CS. Assaying stem cell mechanobiology on microfabricated elastomeric substrates with geometrically modulated rigidity. Nat Protoc. 2011;6:187-213.
[55] Villa-Diaz LG, Nandivada H, Ding J, Nogueira-De-Souza NC, Krebsbach PH, O'Shea KS, et al. Synthetic polymer coatings for long-term growth of human embryonic stem cells. Nature Biotechnology. 2010;28:581-3.
[56] Nandivada H, Villa-Diaz LG, O'Shea KS, Smith GD, Krebsbach PH, Lahann J. Fabrication of synthetic polymer coatings and their use in feeder-free culture of human embryonic stem cells. Nature Protocols. 2011;6:1037-43.
[57] Braam SR, Zeinstra L, Litjens S, Ward-van Oostwaard D, van den Brink S, van Laake L, et al. Recombinant vitronectin is a functionally defined substrate that supports human embryonic stem cell self-renewal via αVβ5 integrin. Stem Cells. 2008;26:2257-65.
[58] Wang L, Schulz TC, Sherrer ES, Dauphin DS, Shin S, Nelson AM, et al. Self-renewal of human embryonic stem cells requires insulin-like growth factor-1 receptor and ERBB2 receptor signaling. Blood. 2007;110:4111-9.
[59] Meili R, Alonso-Latorre B, del Alamo JC, Firtel RA, Lasheras JC. Myosin II is essential for the spatiotemporal organization of traction forces during cell motility. Mol Biol Cell. 2010;21:405-17.
[60] Walker A, Su H, Conti MA, Harb N, Adelstein RS, Sato N. Non-muscle myosin II regulates survival threshold of pluripotent stem cells. Nat Commun. 2010;1:71.
[61] Yim EK, Darling EM, Kulangara K, Guilak F, Leong KW. Nanotopography-induced changes in focal adhesions, cytoskeletal organization, and mechanical properties of human mesenchymal stem cells. Biomaterials. 2010;31:1299-306.
[62] Zhu AJ, Haase I, Watt FM. Signaling via β1 integrins and mitogen-activated protein kinase determines human epidermal stem cell fate in vitro. Proc Natl Acad Sci U S A. 1999;96:6728-33.
[63] Li L, Wang SA, Jezierski A, Moalim-Nour L, Mohib K, Parks RJ, et al. A Unique Interplay Between Rap1 and E-Cadherin in the Endocytic Pathway Regulates Self-Renewal of Human Embryonic Stem Cells. Stem Cells. 2010;28:247-57.
[64] Xu Y, Zhu X, Hahm HS, Wei W, Hao E, Hayek A, et al. Revealing a core signaling regulatory mechanism for pluripotent stem cell survival and self-renewal by small molecules. Proc Natl Acad Sci U S A. 2010;107:8129-34.
[65] Measuring the multi-scale integration of mechanical forces during morphogenesis. Current Opinion in Genetics & Development. 2011.
[66] Zoldan J, Karagiannis ED, Lee CY, Anderson DG, Langer R, Levenberg S. The influence of scaffold elasticity on germ layer specification of human embryonic stem cells. Biomaterials. 2011;32:9612-21.
[67] Chambers SM, Fasano CA, Papapetrou EP, Tomishima M, Sadelain M, Studer L. Highly efficient neural conversion of human ES and iPS cells by dual inhibition of SMAD signaling. Nature Biotechnology. 2009;27:275-80.
[68] Dupuis L, Loeffler JP. Neuromuscular junction destruction during amyotrophic lateral sclerosis: insights from transgenic models. Curr Opin Pharmacol. 2009;9:341-6.

[69] Lunn JS, Sakowski SA, Hur J, Feldman EL. Stem cell technology for neurodegenerative diseases. Ann Neurol. 2011;70:353-61.
[70] Li XJ, Du ZW, Zarnowska ED, Pankratz M, Hansen LO, Pearce RA, et al. Specification of motoneurons from human embryonic stem cells. Nature Biotechnology. 2005;23:215-21.
[71] Patani R, Hollins AJ, Wishart TM, Puddifoot CA, Alvarez S, de Lera AR, et al. Retinoid-independent motor neurogenesis from human embryonic stem cells reveals a medial columnar ground state. Nature Communications. 2011;2.
[72] Huebsch N, Arany PR, Mao AS, Shvartsman D, Ali OA, Bencherif SA, et al. Harnessing traction-mediated manipulation of the cell/matrix interface to control stem-cell fate. Nat Mater. 2010;9:518-26.
[73] Zhang XL, Cui NR, Wu ZY, Su JD, Tadepalli JS, Sekizar S, et al. Intrinsic membrane properties of locus coeruleus neurons in Mecp2-null mice. American Journal of Physiology-Cell Physiology. 2010;298:C635-C46.
[74] Chambers SM, Fasano CA, Papapetrou EP, Tomishima M, Sadelain M, Studer L. Highly efficient neural conversion of human ES and iPS cells by dual inhibition of Smad signaling. Nat Biotechnol. 2009;27:275-80.
[75] Callaerts P, Halder G, Gehring WJ. Pax-6 in development and evolution. Annu Rev Neurosci. 1997;20:483-532.
[76] Keung AJ, Asuri P, Kumar S, Schaffer DV. Soft microenvironments promote the early neurogenic differentiation but not self-renewal of human pluripotent stem cells. Integr Biol. 2012;4:1049-58.
[77] Hitoshi S, Seaberg RM, Koscik C, Alexson T, Kusunoki S, Kanazawa I, et al. Primitive neural stem cells from the mammalian epiblast differentiate to definitive neural stem cells under the control of Notch signaling. Genes Dev. 2004;18:1806-11.
[78] Li XJ, Du ZW, Zarnowska ED, Pankratz M, Hansen LO, Pearce RA, et al. Specification of motoneurons from human embryonic stem cells. Nat Biotechnol. 2005;23:215-21.
[79] Patani R, Hollins AJ, Wishart TM, Puddifoot CA, Alvarez S, de Lera AR, et al. Retinoid-independent motor neurogenesis from human embryonic stem cells reveals a medial columnar ground state. Nat Commun. 2011;2.
[80] Bean BP. The action potential in mammalian central neurons. Nat Rev Neurosci. 2007;8:451-65.
[81] Miles GB, Dai Y, Brownstone RM. Mechanisms underlying the early phase of spike frequency adaptation in mouse spinal motoneurones. J Physiol. 2005;566:519-32.
[82] Karumbayaram S, Kelly TK, Paucar AA, Roe AJT, Umbach JA, Charles A, et al. Human embryonic stem cell-derived motor neurons expressing SOD1 mutants exhibit typical signs of motor neuron degeneration linked to ALS. Dis Model Mech. 2009;2:189-95.
[83] Hester ME, Murtha MJ, Song S, Rao M, Miranda CJ, Meyer K, et al. Rapid and efficient generation of functional motor neurons from human pluripotent stem cells using gene delivered transcription factor codes. Mol Ther. 2011;19:1905-12.
[84] Derynck R, Zhang YE. Smad-dependent and Smad-independent pathways in TGF-β family signalling. Nature. 2003;425:577-84.
[85] Varelas X, Sakuma R, Samavarchi-Tehrani P, Peerani R, Rao BM, Dembowy J, et al. TAZ controls Smad nucleocytoplasmic shuttling and regulates human embryonic stem-cell self-renewal. Nat Cell Biol. 2008;10:837-48.
[86] Zhao B, Wei X, Li W, Udan RS, Yang Q, Kim J, et al. Inactivation of YAP oncoprotein by the Hippo pathway is involved in cell contact inhibition and tissue growth control. Genes Dev. 2007;21:2747-61.
[87] Dupont S, Morsut L, Aragona M, Enzo E, Giulitti S, Cordenonsi M, et al. Role of YAP/TAZ in mechanotransduction. Nature. 2011;474:179-83.
[88] Wada K, Itoga K, Okano T, Yonemura S, Sasaki H. Hippo pathway regulation by cell morphology and stress fibers. Development. 2011;138:3907-14.
[89] Yu FX, Zhao B, Panupinthu N, Jewell JL, Lian I, Wang LH, et al. Regulation of the Hippo-YAP pathway by G-protein-coupled receptor signaling. Cell. 2012;150:780-91.

[90] Calvo F, Ege N, Grande-Garcia A, Hooper S, Jenkins RP, Chaudhry SI, et al. Mechanotransduction and YAP-dependent matrix remodelling is required for the generation and maintenance of cancer-associated fibroblasts. Nat Cell Biol. 2013;15:637-46.
[91] Zhao B, Li L, Wang L, Wang CY, Yu J, Guan KL. Cell detachment activates the Hippo pathway via cytoskeleton reorganization to induce anoikis. Genes Dev. 2012;26:54-68.
[92] Chang T-C, Chen Y-C, Yang M-H, Chen C-H, Hsing E-W, Ko B-S, et al. Rho Kinases regulate the renewal and neural differentiation of embryonic stem cells in a cell plating density–dependent Manner. Plos One. 2010;5:e9187.
[93] Krawetz RJ, Taiani J, Greene A, Kelly GM, Rancourt DE. Inhibition of Rho kinase regulates specification of early differentiation events in P19 embryonal carcinoma stem cells. Plos One. 2011;6:e26484.
[94] Garcia-Gonzalo FR, Izpisua Belmonte JC. Albumin-associated lipids regulate human embryonic stem cell self-renewal. Plos One. 2008;3:e1384.
[95] Blauwkamp TA, Nigam S, Ardehali R, Weissman IL, Nusse R. Endogenous Wnt signalling in human embryonic stem cells generates an equilibrium of distinct lineage-specified progenitors. Nat Commun. 2012;3:1070.
[96] Visser-Grieve S, Zhou ZH, She YM, Huang H, Cyr TD, Xu T, et al. LATS1 tumor suppressor is a novel actin-binding protein and negative regulator of actin polymerization. Cell Research. 2011;21:1513-6.
[97] Copp AJ, Greene ND. Genetics and development of neural tube defects. The Journal of pathology. 2010;220:217-30.
[98] Keller R, Davidson LA, Shook DR. How we are shaped: The biomechanics of gastrulation. Differentiation. 2003;71:171-205.
[99] Ray K, David S, Paul S. The forces that shape embryos: physical aspects of convergent extension by cell intercalation. Physical Biology. 2008;5:015007.
[100] Patthey C, Gunhaga L, Edlund T. Early Development of the Central and Peripheral Nervous Systems Is Coordinated by Wnt and BMP Signals. PLoS ONE. 2008;3:e1625.
[101] Stuhlmiller TJ, Garcia-Castro MI. Current perspectives of the signaling pathways directing neural crest induction. Cell Mol Life Sci. 2012;69:3715-37.
[102] Garnett AT, Square TA, Medeiros DM. BMP, Wnt and FGF signals are integrated through evolutionarily conserved enhancers to achieve robust expression of Pax3 and Zic genes at the zebrafish neural plate border. Development. 2012;139:4220-31.
[103] Patthey C, Edlund T, Gunhaga L. Wnt-regulated temporal control of BMP exposure directs the choice between neural plate border and epidermal fate. Development. 2009;136:73-83.
[104] Eiraku M, Takata N, Ishibashi H, Kawada M, Sakakura E, Okuda S, et al. Self-organizing optic-cup morphogenesis in three-dimensional culture. Nature. 2011;472:51-6.
[105] Suga H, Kadoshima T, Minaguchi M, Ohgushi M, Soen M, Nakano T, et al. Self-formation of functional adenohypophysis in three-dimensional culture. Nature. 2011;480:57-62.
[106] Nakano T, Ando S, Takata N, Kawada M, Muguruma K, Sekiguchi K, et al. Self-formation of optic cups and storable stratified neural retina from human ESCs. Cell Stem Cell. 2012;10:771-85.
[107] Takebe T, Sekine K, Enomura M, Koike H, Kimura M, Ogaeri T, et al. Vascularized and functional human liver from an iPSC-derived organ bud transplant. Nature. 2013;499:481-4.
[108] Spence JR, Mayhew CN, Rankin SA, Kuhar MF, Vallance JE, Tolle K, et al. Directed differentiation of human pluripotent stem cells into intestinal tissue in vitro. Nature. 2011;470:105-9.
[109] Nelson CM, Jean RP, Tan JL, Liu WF, Sniadecki NJ, Spector AA, et al. Emergent patterns of growth controlled by multicellular form and mechanics. Proc Natl Acad Sci U S A. 2005;102:11594-9.
[110] Schlosser G. Do vertebrate neural crest and cranial placodes have a common evolutionary origin? BioEssays. 2008;30:659-72.
[111] McBeath R, Pirone DM, Nelson CM, Bhadriraju K, Chen CS. Cell shape, cytoskeletal tension, and RhoA regulate stem cell lineage commitment. Developmental Cell. 2004;6:483-95.

[112] Mann JM, Lam RH, Weng S, Sun Y, Fu J. A silicone-based stretchable micropost array membrane for monitoring live-cell subcellular cytoskeletal response. Lab Chip. 2012;12:731-40.
[113] Lam RHW, Sun YB, Chen WQ, Fu JP. Elastomeric microposts integrated into microfluidics for flow-mediated endothelial mechanotransduction analysis. Lab Chip. 2012;12:1865-73.
[114] Svoboda K, Schmidt CF, Schnapp BJ, Block SM. Direct Observation of Kinesin Stepping by Optical Trapping Interferometry. Nature. 1993;365:721-7.
[115] Smith SB, Finzi L, Bustamante C. Direct Mechanical Measurements of the Elasticity of Single DNA-Molecules by Using Magnetic Beads. Science. 1992;258:1122-6.
[116] Strick TR, Allemand JF, Bensimon D, Bensimon A, Croquette V. The elasticity of a single supercoiled DNA molecule. Science. 1996;271:1835-7.
[117] Sheetz MP. Laser tweezers in cell biology. Introduction. Methods in Cell Biology. 1997/11/14 ed1998. p. xi-xii.
[118] Huang H, Kamm RD, Lee RT. Cell mechanics and mechanotransduction: pathways, probes, and physiology. American Journal of Physiology-Cell Physiology. 2004;287:C1-11.
[119] Tanase M, Biais N, Sheetz M. Magnetic Tweezers in Cell Biology. In: Wang Y, Discher DE, editors. Methods in Cell Biology: Academic Press; 2007. p. 473-93.
[120] Chen JX, Fabry B, Schiffrin EL, Wang N. Twisting integrin receptors increases endothelin-1 gene expression in endothelial cells. American Journal of Physiology-Cell Physiology. 2001;280:C1475-C84.
[121] Kitzman DW, Goldman ME, Gillam LD, Cohen JL, Aurigemma GP, Gottdiener JS. Efficacy and safety of the novel ultrasound contrast agent perflutren (definity) in patients with suboptimal baseline left ventricular echocardiographic images. Am J Cardiol. 2000;86:669-74.
[122] Wei K, Mulvagh SL, Carson L, Davidoff R, Gabriel R, Grimm RA, et al. The safety of deFinity and Optison for ultrasound image enhancement: a retrospective analysis of 78,383 administered contrast doses. J Am Soc Echocardiogr. 2008;21:1202-6.
[123] Ellegala DB, Leong-Poi H, Carpenter JE, Klibanov AL, Kaul S, Shaffrey ME, et al. Imaging tumor angiogenesis with contrast ultrasound and microbubbles targeted to alpha(v)beta3. Circulation. 2003;108:336-41.
[124] Takalkar AM, Klibanov AL, Rychak JJ, Lindner JR, Ley K. Binding and detachment dynamics of microbubbles targeted to P-selectin under controlled shear flow. J Control Release. 2004;96:473-82.
[125] Klibanov AL. Preparation of targeted microbubbles: ultrasound contrast agents for molecular imaging. Med Biol Eng Comput. 2009;47:875-82.
[126] Kaufmann BA, Sanders JM, Davis C, Xie A, Aldred P, Sarembock IJ, et al. Molecular imaging of inflammation in atherosclerosis with targeted ultrasound detection of vascular cell adhesion molecule-1. Circulation. 2007;116:276-84.
[127] Winter PM, Morawski AM, Caruthers SD, Fuhrhop RW, Zhang H, Williams TA, et al. Molecular imaging of angiogenesis in early-stage atherosclerosis with alpha(v)beta3-integrin-targeted nanoparticles. Circulation. 2003;108:2270-4.
[128] Leong-Poi H. Molecular imaging using contrast-enhanced ultrasound: evaluation of angiogenesis and cell therapy. Cardiovascular Research. 2009;84:190-200.
[129] Anderson CR, Hu X, Zhang H, Tlaxca J, Decleves AE, Houghtaling R, et al. Ultrasound molecular imaging of tumor angiogenesis with an integrin targeted microbubble contrast agent. Invest Radiol. 2011;46:215-24.
[130] Fan Z, Liu H, Mayer M, Deng CX. Spatiotemporally controlled single cell sonoporation. Proc Natl Acad Sci U S A. 2012;109:16486-91.
[131] Kooiman K, Foppen-Harteveld M, van der Steen AFW, de Jong N. Sonoporation of endothelial cells by vibrating targeted microbubbles. J Control Release. 2011;154:35-41.
[132] van Wamel A, Kooiman K, Harteveld M, Emmer M, ten Cate FJ, Versluis M, et al. Vibrating microbubbles poking individual cells: drug transfer into cells via sonoporation. J Control Release. 2006;112:149-55.
[133] Marmottant P, Hilgenfeldt S. Controlled vesicle deformation and lysis by single oscillating bubbles. Nature. 2003;423:153.

[134] Prentice P, Cuschieri A, Dholakia K, Prausnitz M, Campbell P. Membrane disruption by optically controlled microbubble cavitation. Nature Physics. 2005;1:107.
[135] Postema M, van Wamel A, Lancee CT, de Jong N. Ultrasound-induced encapsulated microbubble phenomena. Ultrasound Med Biol. 2004;30:827-40.
[136] O'Brien WD, Jr. Ultrasound-biophysics mechanisms. Prog Biophys Mol Biol. 2007;93:212-55.
[137] Wu J, Nyborg WL. Ultrasound, cavitation bubbles and their interaction with cells. Adv Drug Deliver Rev. 2008;60:1103-16.
[138] Miller DL. Overview of experimental studies of biological effects of medical ultrasound caused by gas body activation and inertial cavitation. Progress in Biophysics & Molecular Biology. 2007;93:314-30.
[139] Dayton PA, Morgan KE, Klibanov ALS, Brandenburger G, Nightingale KR, Ferrara KW. A preliminary evaluation of the effects of primary and secondary radiation forces on acoustic contrast agents. Ieee Transactions on Ultrasonics Ferroelectrics and Frequency Control. 1997;44:1264-77.
[140] Dayton PA, Morgan KE, Klibanov AL, Brandenburger GH, Ferrara KW. Optical and acoustical observations of the effects of ultrasound on contrast agents. IEEE Trans Ultrason Ferroelectr Freq Control. 1999;46:220-32.
[141] Zhou Y, Yang K, Cui J, Ye JY, Deng CX. Controlled permeation of cell membrane by single bubble acoustic cavitation. J Control Release. 2012;157:103-11.
[142] Riento K, Ridley AJ. Rocks: multifunctional kinases in cell behaviour. Nat Rev Mol Cell Biol. 2003;4:446-56.
[143] Watanabe K, Ueno M, Kamiya D, Nishiyama A, Matsumura M, Wataya T, et al. A ROCK inhibitor permits survival of dissociated human embryonic stem cells. Nat Biotech. 2007;25:681-6.
[144] Ohgushi M, Matsumura M, Eiraku M, Murakami K, Aramaki T, Nishiyama A, et al. Molecular Pathway and Cell State Responsible for Dissociation-Induced Apoptosis in Human Pluripotent Stem Cells. Cell Stem Cell. 2010;7:225-39.
[145] Chen GK, Hou ZG, Gulbranson DR, Thomson JA. Actin-Myosin Contractility Is Responsible for the Reduced Viability of Dissociated Human Embryonic Stem Cells. Cell Stem Cell. 2010;7:240-8.
[146] Harb N, Archer TK, Sato N. The Rho-Rock-Myosin Signaling Axis Determines Cell-Cell Integrity of Self-Renewing Pluripotent Stem Cells. Plos One. 2008;3.
[147] Wozniak MA, Chen CS. Mechanotransduction in development: a growing role for contractility. Nat Rev Mol Cell Biol. 2009;10:34-43.
[148] Erpelding TN, Hollman KW, O'Donnell M. Bubble-based acoustic radiation force using chirp insonation to reduce standing wave effects. Ultrasound in medicine & biology. 2007;33:263-9.
[149] Dayton PA, Morgan KE, Klibanov AL, Brandenburger G, Nightingale KR, Ferrara KW. A preliminary evaluation of the effects of primary and secondary radiation forces on acoustic contrast agents. Ultrasonics, Ferroelectrics and Frequency Control, IEEE Transactions on. 1997;44:1264-77.
[150] Gormley G, Wu JR. Observation of acoustic streaming near Albunex (R) spheres. Journal of the Acoustical Society of America. 1998;104:3115-8.
[151] Marmottant P, Hilgenfeldt S. A bubble-driven microfluidic transport element for bioengineering. Proceedings of the National Academy of Sciences of the United States of America. 2004;101:9523-7.
[152] Fan Z, Kumon RE, Park J, Deng CX. Intracellular delivery and calcium transients generated in sonoporation facilitated by microbubbles. Journal of Controlled Release. 2010;142:31-9.
[153] Chowdhury F, Na S, Li D, Poh YC, Tanaka TS, Wang F, et al. Material properties of the cell dictate stress-induced spreading and differentiation in embryonic stem cells. Nat Mater. 2010;9:82-8.
[154] Ingber DE. Cellular mechanotransduction: putting all the pieces together again. Faseb J. 2006;20:811-27.
[155] Rooney JA. Shear as a Mechanism for Sonically Induced Biological Effects. Journal of the Acoustical Society of America. 1972;52:1718-24.
[156] Wu J. Shear stress in cells generated by ultrasound. Prog Biophys Mol Biol. 2007;93:363-73.
[157] Marmottant P, Hilgenfeldt S. Controlled vesicle deformation and lysis by single oscillating bubbles. Nature. 2003;423:153-6.

[158] Ji JY, Jing H, Diamond SL. Shear stress causes nuclear localization of endothelial glucocorticoid receptor and expression from the GRE promoter. Circ Res. 2003;92:279-85.
[159] Bardsley WG, Aplin JD. Kinetic analysis of cell spreading. I. Theory and modelling of curves. J Cell Sci. 1983;61:365-73.
[160] Barbaric I, Biga V, Gokhale Paul J, Jones M, Stavish D, Glen A, et al. Time-Lapse Analysis of Human Embryonic Stem Cells Reveals Multiple Bottlenecks Restricting Colony Formation and Their Relief upon Culture Adaptation. Stem Cell Reports.
[161] Li L, Wang BH, Wang S, Moalim-Nour L, Mohib K, Lohnes D, et al. Individual cell movement, asymmetric colony expansion, rho-associated kinase, and E-cadherin impact the clonogenicity of human embryonic stem cells. Biophys J. 2010;98:2442-51.
[162] Gramiak R, Shah PM. Echocardiography of the Aortic Root. Investigative Radiology. 1968;3:356-66.
[163] Goldberg BB, Liu J-B, Forsberg F. Ultrasound contrast agents: A review. Ultrasound in Medicine & Biology. 1994;20:319-33.
[164] Kaul S. Myocardial contrast echocardiography: a 25-year retrospective. Circulation. 2008;118:291-308.
[165] Lentacker I, De Smedt SC, Demeester J, Sanders NN. Microbubbles which bind and protect DNA against nucleases. J Control Release. 2006;116:e73-5.
[166] Lum AF, Borden MA, Dayton PA, Kruse DE, Simon SI, Ferrara KW. Ultrasound radiation force enables targeted deposition of model drug carriers loaded on microbubbles. J Control Release. 2006;111:128-34.
[167] Frampton JP, Fan Z, Simon A, Chen D, Deng CX, Takayama S. Aqueous Two-Phase System Patterning of Microbubbles: Localized Induction of Apoptosis in Sonoporated Cells. Advanced Functional Materials. 2013:n/a-n/a.
[168] Kiessling F, Fokong S, Koczera P, Lederle W, Lammers T. Ultrasound microbubbles for molecular diagnosis, therapy, and theranostics. J Nucl Med. 2012;53:345-8.
[169] Visser-Grieve S, Zhou Z, She Y-M, Huang H, Cyr TD, Xu T, et al. Lats1 tumor suppressor is a novel actin-binding protein and negative regulator of actin polymerization. Cell Res. 2011;21:1513-6.
[170] Du J, Chen XF, Liang XD, Zhang GY, Xu J, He LR, et al. Integrin activation and internalization on soft ECM as a mechanism of induction of stem cell differentiation by ECM elasticity. Proc Natl Acad Sci USA. 2011;108:9466-71.
[171] Engler AJ, Sen S, Sweeney HL, Discher DE. Matrix elasticity directs stem cell lineage specification. Cell. 2006;126:677-89.
[172] Connelly JT, Gautrot JE, Trappmann B, Tan DWM, Donati G, Huck WTS, et al. Actin and serum response factor transduce physical cues from the microenvironment to regulate epidermal stem cell fate decisions. Nat Cell Biol. 2010;12:711-8.
[173] Holst J, Watson S, Lord MS, Eamegdool SS, Bax DV, Nivison-Smith LB, et al. Substrate elasticity provides mechanical signals for the expansion of hemopoietic stem and progenitor cells. Nat Biotechnol. 2010;28:1123-8.
[174] Huebsch N, Arany PR, Mao AS, Shvartsman D, Ali OA, Bencherif SA, et al. Harnessing traction-mediated manipulation of the cell/matrix interface to control stem-cell fate. Nature Mater. 2010;9:518-26.
[175] Varelas X, Sakuma R, Samavarchi-Tehrani P, Peerani R, Rao BM, Dembowy J, et al. TAZ controls Smad nucleocytoplasmic shuttling and regulates human embryonic stem-cell self-renewal. Nature Cell Biology. 2008;10:837-48.
[176] Kraehenbuehl TP, Langer R, Ferreira LS. Three-dimensional biomaterials for the study of human pluripotent stem cells. Nat Methods. 2011;8:731-6.
[177] Kshitiz, Kim DH, Beebe DJ, Levchenko A. Micro- and nanoengineering for stem cell biology: the promise with a caution. Trends Biotechnol. 2011;29:399-408.
[178] Lele TP, Sero JE, Matthews BD, Kumar S, Xia S, MontoyaZavala M, et al. Tools to Study Cell Mechanics and Mechanotransduction. In: YuLi W, Dennis ED, editors. Methods in Cell Biology: Academic Press; 2007. p. 441, 3-72.

[179] Kim DH, Wong PK, Park J, Levchenko A, Sun Y. Microengineered platforms for cell mechanobiology. Annu Rev Biomed Eng. 2009;11:203-33.
[180] Sun Y, Yong KM, Villa-Diaz LG, Zhang X, Chen W, Philson R, et al. Hippo/YAP-mediated rigidity-dependent motor neuron differentiation of human pluripotent stem cells. Nat Mater. 2014.
[181] Downing TL, Soto J, Morez C, Houssin T, Fritz A, Yuan F, et al. Biophysical regulation of epigenetic state and cell reprogramming. Nat Mater. 2013;12:1154-62.
[182] Carson AR, McTiernan CF, Lavery L, Grata M, Leng X, Wang J, et al. Ultrasound-targeted microbubble destruction to deliver siRNA cancer therapy. Cancer Res. 2012;72:6191-9.
[183] Chen H, Hwang JH. Ultrasound-targeted microbubble destruction for chemotherapeutic drug delivery to solid tumors. J Ther Ultrasound. 2013;1:10.
[184] Klibanov AL. Ultrasound molecular imaging with targeted microbubble contrast agents. J Nucl Cardiol. 2007;14:876-84.
[185] Chaudhuri O, Gu L, Darnell M, Klumpers D, Bencherif SA, Weaver JC, et al. Substrate stress relaxation regulates cell spreading. Nat Commun. 2015;6:6365.
[186] Ali MY, Chuang CY, Saif MTA. Reprogramming cellular phenotype by soft collagen gels. Soft Matter. 2014;10:8829-37.
[187] Cui Y, Hameed FM, Yang B, Lee K, Pan CQ, Park S, et al. Cyclic stretching of soft substrates induces spreading and growth. Nat Commun. 2015;6.
[188] Zhao X, Kim J, Cezar CA, Huebsch N, Lee K, Bouhadir K, et al. Active scaffolds for on-demand drug and cell delivery. Proc Natl Acad Sci U S A. 2011;108:67-72.
[189] Yang C, Tibbitt MW, Basta L, Anseth KS. Mechanical memory and dosing influence stem cell fate. Nat Mater. 2014;13:645-52.